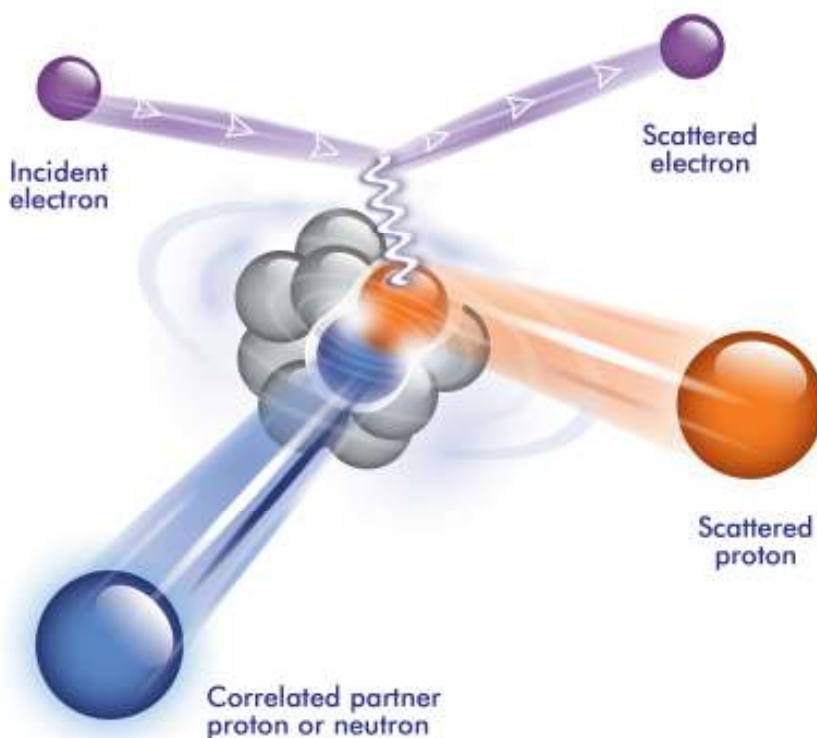


**Investigation of Proton-Proton Short-Range Correlations via the
 $^{12}\text{C}(e,e'pp)$ Reaction**

Thesis submitted towards the degree of
Doctor of Philosophy

By
Ran Shneor



SUBMITTED TO THE SENATE OF TEL-AVIV UNIVERSITY
December 2007

This work was carried out under the supervision of
Professor Eli Piassetzky

Abstract

In this work we present a simultaneous measurement of the $^{12}\text{C}(e,e'p)$ and $^{12}\text{C}(e,e'pp)$ reactions. This measurement was done as part of the E01-015 experiment at Hall A of Jefferson Lab, at $Q^2 = 2 \text{ (GeV/c)}^2$, $x_B = 1.2$, for an $(e,e'p)$ missing-momentum range from 300 to 600 MeV/c. At these kinematics conditions, with a missing-momentum greater than the Fermi momentum of nucleons in a nucleus and far from the D excitation, nucleon-nucleon Short-Range Correlations (SRCs) are predicted to dominate the reaction. For $9.5 \pm 2\%$ of the $^{12}\text{C}(e,e'p)$ events, a recoiling partner proton was observed in the opposite direction to the $^{12}\text{C}(e,e'p)$ missing momentum vector with roughly equal momentum. This observation is an experimental signature for proton-proton short-range correlations (pp-SRC) in nuclei.

Even though the probability of pp-SRCs in nuclei is small, they are important since they can teach us about the strong interaction at short distances. Moreover, as a manifestation of asymmetric dense cold nuclear matter that can be studied in the laboratory, pp-SRCs are relevant to the understanding of neutron stars.

Notations and Conventions

JLab	Thomas Jefferson Laboratory
2N -SRC	Two Nucleon Short-Range Correlations
3N -SRC	Three Nucleon Short-Range Correlations
ADC	Analog to Digital Converter
BCM	Beam Current Monitor
BigBite	The Large Acceptance BigBite Spectrometer
BNL	Brookhaven National Laboratory
BPM	Beam Position Monitor
CAMAC	Computer Automated Measurement And Control
CEBAF	Continuous Electron Beam Accelerator Facility
CODA	JLab DAQ software
DAQ	Data Acquisition
DWIA	Distorted Wave Impulse Approximation
EB	Event Builder
ER	Event Recorder
FSI	Final State Interactions
HRS	High Resolution Spectrometer
IA	Impulse Approximation
IC	Isobar Currents
IPM	Independent Particle Model
ISI	Initial State Interactions
MAMI	Mainzer Mikrotron
MEC	Meson Exchange Currents
MLU	Memory Look Up
NIKHEF	National Institute for Nuclear Physics and High Energy Physics in Amsterdam.
PAW	Physics Analysis Workstation
PID	Particle Identification
PMT	Photo Multiplier Tube
PWIA	Plain Wave Impulse Approximation
ROC	Read Out Control Unit
ROOT	An object oriented framework for large scale data analysis
SLAC	Stanford Linear Accelerator Center
SRC	Short-Range Correlations
TDC	Time to Digital Converter
TOF	Time of Flight
VDC	Vertical Drift Chamber
VME	Virtual Machine Environment

Contents

1. Scientific Background.....	13
1.1 Introduction.....	13
1.2 Previous experiments related to Short Rang Correlations.....	14
1.2.1 Inclusive experiments.....	14
1.2.2 Semi-exclusive experiments.....	15
1.2.3 Triple coincidence experiments.....	17
1.3 This experiment.....	19
1.3.1 Introduction.....	19
1.3.2 Impulse approximation description of the $^{12}\text{C}(e,e'pp)$ reaction.....	19
1.3.3 Suppression of competing effects.....	21
1.3.4 The selected kinematics for the experiment.....	24
2 Apparatus and Experimental Setup.....	25
2.1 CEBAF Accelerator.....	25
2.2 Hall A and its standard equipment.....	25
2.2.1 The Beam Line.....	27
2.2.2 The scattering chamber and the target.....	28
2.2.3 The High Resolution Spectrometers.....	30
2.3 The large acceptance BigBite spectrometer.....	32
2.3.1 Design and building of BigBite for the SRC experiment.....	32
2.3.2 BigBite characteristics and performance.....	32
2.4 Electronics and Data Acquisition.....	37
2.4.1 Trigger setup.....	37
2.4.2 Data Acquisition System.....	39
2.4.3 Offline Analysis.....	39
3. Data Analysis.....	41
3.1 Particle Identification and momentum/angle measurement with BigBite.....	41
3.1.1 ADC and TDC Calibrations.....	41
3.1.2 Use of ep Elastic data for calibration and tuning.....	42
3.1.3 Momentum reconstruction.....	42
3.1.4 Reconstruction of scattering angles.....	48
3.1.5 Particle Identification.....	49
3.1.6 Definition of Track and Selection of the Golden Track.....	50
3.1.7 Efficiencies.....	52
3.2 Cuts and selection of events.....	54
3.2.1 The $^{12}\text{C}(e,e'p)$ reaction.....	54
3.2.2 The $^{12}\text{C}(e,e'pp)$ reaction.....	55
4 Results and Conclusions.....	58
4.1 The semi inclusive $X_B > 1$ $^{12}\text{C}(e,e'p)$ reaction.....	58
4.2 The triple coincidence $^{12}\text{C}(e,e'pp)$ reaction.....	63
4.3 The motion of the correlated pair.....	67
4.4 The $(e,e'pp)/(e,e'p)$ ratio.....	71
4.4.1 The measured ratio.....	71
4.4.2 The extrapolated ratio.....	71
4.4.3 Sensitivity check for the $(e,e'pp)/(e,e'p)$ ratio.....	73
4.5 The missing energy spectra of the $^{12}\text{C}(e,e'pp)$ reaction.....	75
4.6 Summary and Conclusions.....	77

Appendix

Appendix A - Path reconstruction for charged particles in BigBite.....	78
Appendix B - Monte-Carlo Simulation.....	82
Appendix C - Estimation of Final-State Interactions contribution.....	84

List of Figures

1-1	The cross section scaling $r = 3 \times \sigma[A(e, e')]/A \times \sigma[^3\text{He}(e, e')]$ as a function of x_B [4].	15
1-2	The spectroscopic strength vs. the target mass for the (e,e'p) reaction [2]. The data are compared to IPM calculations.	16
1-3	The correlation between P_n and its direction γ relative to the direction of the struck proton in the quasi-elastic (p,2p) reaction. Data labeled by 94 and 98 are from Refs. [28,30], respectively. The momenta are the beam momenta. The dotted vertical line corresponds to $P_n = 275 \text{ MeV}/c$.	18
1-4	The c.m. width of the correlated n - p pairs in ^{12}C . The data represents the distribution of the longitude component of the c.m. width p_z^{cm} from $^{12}\text{C}(p,2pn)$ measurement at BNL.	18
1-5	The Impulse Approximation Description of the $^{12}\text{C}(e, e'pp)$ reaction.	20
1-6	Feynman diagram of different possible reaction channels.	23
1-7	A vector diagram of the kinematics of the $^{12}\text{C}(e, e'pp)$ measurement.	24
2-1	Schematic layout of JLAB accelerator.	26
2-2	Schematic layout of Hall A.	26
2-3	Schematic layout of Hall A, indicating the location of the raster, the EP energy measurement system, the beam current monitors (BCM) and the beam position monitors (BPM) upstream of the target. Also indicated are the locations of the components of one of the high-resolution spectrometers (Q1, Q2, dipole, Q3 and shield house) and of the beam dump. The beam polarimeters shown in this figure were not used in this experiment.	27

2-4	Exploded view of the scattering chamber.....	28
2-5	Schematic view of the Hall A target ladder for E01-015 and the targets used for the experiment (Left). Schematic view of the tilted carbon target (Right).....	29
2-6	layout of Hall A High Resolution Spectrometer (HRS).....	30
2-7	A schematic layout of the detector packages for the electron (left) and hadron (right) high resolution spectrometers. Note that not all of these detectors were utilized during this experiment.....	32
2-8	A photo of BigBite with the magnet (left) auxiliary (middle) and trigger (right) scintillator detector planes, as set in Hall A for the E01-015 experiment	34
2-9	The auxiliary plane during assembly.....	34
2-10	A schematic plot of a single auxiliary plane counter, with the light guide, the PMT and the magnetic shield.....	35
2-11	A Schematic layout of the Trigger Plane.....	36
2-12	A side view of the Trigger plane.....	36
2-13	Circuit diagrams of the trigger system.....	38
2-14	A block diagram of the Hall A data acquisition system (DAQ).....	40
3-1	Pulse height in the ΔE plane vs. Pulse height in the E plane in ADC channels. The dotted line represents the "punch-through" point B, while the blue line represent protons with increasing momentum from top (C) to buttom (A). This plot which includes all the counters in the E and ΔE planes, was produced after first matching the gain of the different paddles inside the E and ΔE planes.....	44

3-2	Reconstructed momentum using TOF vs proton momentum from the electron HRS (Left). The difference of the two reconstructed momentums (Right). Momentum reconstruction using TOF between the target and the E plane (Top). Using TOF between the Auxiliary plane and the E-plane (Bottom).....	46
3-3	Reconstructed momentum using analytical calculation of the radius of curvature inside the magnetic field vs proton momentum from the electron HRS (Top). Fit based reconstructed momentum using hit-position, vs proton momentum from the electron HRS (Bottom).....	46
3-4	Reconstructed momentum using energy deposit vs proton momentum from the electron HRS (Left). The difference of the two reconstructed momentums (Right). Reconstructed momentum using energy deposit in the E plane (Top). Momentum reconstruction using energy deposit in the DE plane (Middle). Momentum reconstruction using energy deposit in the auxiliary plane (Bottom).....	47
3-5	The in-plane angle reconstructed in BigBite [deg] vs. the in-plane angle of the proton as determined from the electron [deg] (Left). The difference between the in-of-plane angle as measured in BigBite and the expected angle from the electron as measured by the HRS (Right).	48
3-6	The out of plane angle reconstructed in BigBite [deg] vs. the out-of-plane angle of the proton as determined from the electron [deg] (Left). The difference between the out-of-plane angle as measured in BigBite and the expected angle from the electron as measured by the HRS with a typical resolution of $\sigma=1.5^\circ$ (Right).....	49

3-7	The pulse height in the ΔE plane vs. the pulse height in the E plane in ADC channels. The yellow areas represent a low energy deposit areas cut, which are typical to photons and pions. Further PID cuts included a "sleeve" cut which follows the proton blue line. Deuterium and heavier particles are located in a higher E and ΔE energy deposit (to the right of the blue line).....	50
3-8	Distribution of the number of reconstructed tracks from different data sets. Left: elastic data set (highest luminosity). Center: number of tracks distribution for 30mA beam current data Right number of tracks for 5 mA beam current (lowest luminosity). The number of tracks in the different distributions increases with the luminosity. Notice that the tracks are only these reconstructed for protons identified by the E ΔE energy deposit.....	51
3-9	The average proton momentum vs. the proton momentum reconstructed from the electron HRS (Left). The difference of the two reconstructed momentums, with a $\sigma = 25$ MeV/c (Right).....	51
3-10	The score function calculated for the elastic data events viewed using a log scale. The narrow peak at the left side of the left figure represents simulated results using no accidentals (Left). Zoom in of the function calculated for the elastics data events. Applying a cut < 2 to the simulated distribution, will result with about 1 percent event loss. A similar cut on the data will remove about 30 % of the total events (Right).....	52
3-11	A Scatter plot of the out-of-plane angle [mrad] vs the proton momentum [MeV/c] for proton singles. The angular acceptance of BigBite is limited at momenta lower than < 350 MeV/c.....	53
3-12	The coincidence time between the two HRS, with a width of 0.4 ns. The beam structure can be seen with a width of 2ns.....	54

3-13	The out-of-plane angle vs. the in-plane angle of \vec{p}_{miss} for kinematics k1 (top), k2 (middle) and k3 (bottom).....	56
3-14	Number of counts vs. the time difference between the two HRSs, and vs. the time difference between BigBite E-plane and HRS-L.....	57
3-15	The distribution of the hit bar number in BigBite Trigger plane (E+DE) vs. the Auxiliary plane bar number. The area between the two diagonal lines was selected in order to remove natural and negatively charged particles tracks.....	57
4-1	The PWIA Feynman diagram of the $^{12}\text{C}(e,e'p)$ reaction. k_F is the Fermi sea level, which for ^{12}C is 220 MeV/c.....	58
4-2	The energy transfer distribution [top]. The momentum transfer distribution [middle], and the Bjorken scaling x_B variable distribution [bottom]. The dashed line represents the entire measured distribution, while the solid line is the distribution after a cut to remove Δ -production events that was applied on the angle of \vec{p}_{miss}	59
4-3	The missing momentum spectrum of the A-1 system for the K1 (solid), K2 (dash) and K3 (points) kinematics.....	60
4-4	The measured $^{12}\text{C}(e,e'p)$ missing-energy spectra for kinematics K1, K2 and K3 (top to bottom). The peak at 16 MeV in K1 is due to removal of p-shell protons, leaving the ^{11}B in its ground state. The grey region contains events from s and p shell removal with residual excited bound or continuum states. The dash line contains events in which a Δ was excited. The Δ -production removal cut was applied either by using an angular cut on \vec{p}_{miss} (Left), or by applying a $x_B > 1$ (Right).	61

4-5	Differential Cross-Section in the $^{12}\text{C}(e,e'p)^{11}\text{B}$ transition as a function of the missing momentum. The red curve represents many-body calculation by Ciof [56], which take in to account short-range correlations. The green curve is a result of harmonic oscillator model calculation.....	62
4-6	The PWIA Feynman diagram of the $^{12}\text{C}(e,e'pp)$ reaction. k_F is the Fermi sea level, which for ^{12}C is 220 MeV/c.....	63
4-7	The corrected TOF between the target and BigBite E plane for K1, K2 and K3 kinematics from top to bottom respectively. The vertical solid (dashed) lines represent the edges of the signal and background cut windows.....	64
4-8	The net number of e'pp events vs. the width of the signal TOF cut in TDC channels (1 ch = 35 picosec), for K1, K2 and K3 kinematics top to bottom respectively. The lines mark the width of the cut used to calculate the number of (e,e'pp). see also figures 4-7.....	65
4-9	The energy transfer distribution [top]. The momentum transfer distribution [middle], and the Bjorken scaling x_B variable distribution [bottom] . The dashed line represents the measured background subtracted $^{12}\text{C}(e,e'pp)$ distribution. The solid line is the $^{12}\text{C}(e,e'p)$ distributions normalized to the same total number of events. Both curves are after a cut to remove Δ -production events was applied on the angle of \vec{p}_{miss}	66
4-10	The distribution of the cosine of the opening angle γ , between \vec{p}_i and \vec{p}_{rec} for the K2 (top) and K3 (bottom) kinematics. The histogram shows the distribution of random events. The curve is a simulation of the scattering off a moving pair with a width of 0.136 GeV/c for the pair c.m. momentum.....	68

4-11	'Measured' vs. 'real' width of the c.m. motion in the vertical direction for K1, K2 and K3 (top to bottom). The curve is a result of the simulation described in appendix B. The middle horizontal line in each plot represents the width of the data. The top and bottom lines define one standard deviation	69
4-12	'Measured' vs. 'real' width of the c.m. motion in the scattering plane in the direction of BigBite for K1, K2 and K3 (top to bottom). The curve is a result of the simulation described in appendix B. The middle horizontal line in each plot represents the width of the data. The top and bottom lines define one standard deviation from the central value.....	70
4-13	The two components of the measured c.m. width for each of the K1, K2 and K3 kinematics (2 x 3 points in total).....	71
4-14	The measured and extrapolated ratios of yields for the $^{12}\text{C}(e,e'pp)$ and the $^{12}\text{C}(e,e'p)$ reactions. Top - the raw yield ratios. Middle- Differential cross section ratio of the $^{12}\text{C}(e,e'pp)$ reaction to the $^{12}\text{C}(e,e'p)$ reaction. Bottom- A simulation was used to account for the finite acceptance of BigBite and make the extrapolation to the total number of recoiling proton pairs shown in the lower figure. The gray area represents a band of $\pm 2\sigma$ uncertainty in the width of the c.m. momentum of the pair.....	72
4-15	The vertical (Left-A) and horizontal (Right-B) angular acceptance cuts defined for the $(e,e'p)/(e,e'pp)$ ratio sensitivity check.....	74
4-16	The number of events as a function of the two nucleon missing energy E_{2m} for kinematics K2 and K3 combined.....	76
4-17	The number of events as a function of the two nucleon missing energy E_{2m} This experiment kinematics K2 and K3 combined (Top) . Measurement by Kester et al.[17] (Middle). Measurement by Penn et.al.[59] (Bottom).....	76

List of Tables

4-1	Summary of the total charge and number of (e,e'p) and (e,e'pp) events for each of the 3 kinematical setups K1, K2 and K3.....	62
4-2	The values of the ratio at the central cut values, and calculated ratio when changing the cuts position at +4° and -4° relative to the central cut values.....	73
4-3	The values of the measured ratios with the nominal cut values, and calculated ratios when replacing the \bar{p}_{miss} angular cut with a $x_B > 1$ cut.....	73
4-4	The values of the extrapolated ratio with the nominal cut values, and calculated ratio when applying half angular acceptance cuts to the vertical and horizontal angles.....	74
C-1	Data for 1.5 GeV/c proton are from O'Neill <i>et al.</i> PL 351(1995)87. The Data is an average of the measurement at $Q^2=1$ and 3GeV/c ²	84
C-2	Data for 600 MeV/c protons from Garino <i>et al.</i> [66].....	84

Chapter 1

Scientific Background

1.1 Introduction

Nuclei are composed of bound protons and neutrons, referred to collectively as nucleons (the standard notation is p , n , and N , respectively). The standard model of the nucleus since the 1950s has been the nuclear shell model, where neutrons and protons move independently in well-defined quantum orbits in the average nuclear field created by their mutual attractive interactions. The 1963 Nobel Prize in Physics was awarded (in part) to M. Goeppert-Mayer and J. H. D. Jensen for their discoveries concerning nuclear shell structure [1].

In the 1980s and 1990s, proton removal experiments using electron beams with energies of several hundred MeV showed that only 60-70% of the protons participate in this type of independent-particle motion predicted by the shell model [2]. At the time, it was assumed that this low occupancy is due to correlated pairs of nucleons within the nucleus. Indeed, the existence of nucleon pairs that are correlated at distances of several femtometers, long-range correlations, has been established, but these accounted for less than half of the predicted correlated nucleon pairs. Recent measurements [3,4] have shown that a substantial fraction of the nucleons in nuclear ground states form pairs in which the distance between the correlated nucleons is one femtometer or smaller. These pairs, which have a large relative momentum and small center-of-mass (CM) momentum, are referred to as short-range correlated (SRC) pairs. The study of these SRC pairs allows unique access to cold dense nuclear matter such as would be found on a large scale in a neutron star.

Experimentally, a high-momentum probe can knock a proton out of a nucleus, leaving the rest of the system nearly unaffected. If, on the other hand, the proton being struck is very close to another nucleon, the nucleon-nucleon force would cause both nucleons to be ejected, as shown in the figure on the cover page. The signature of such a pair is the observation of two nucleons with large, nearly equal and opposite momenta in the laboratory frame of reference.

This thesis presents the results of measurements of the $^{12}\text{C}(e,e'p)$ and $^{12}\text{C}(e,e'pp)$ reactions at high energy and large momentum transfers. The experiment (E01-015) was performed in Hall A of the Thomas Jefferson Lab (JLab). As shown in this thesis we identified pp-SRC pairs in ^{12}C and measured the probabilities of a proton in ^{12}C to be a member of such a pair. In the same experiment (E01-015) we also measured the $^{12}\text{C}(e,e'pn)$ reaction. The results of the later measurement will be reported in another thesis [5].

1.2 Previous experiments related to Short Range Correlations.

Short Range Correlations (SRC) in nuclei have been actively investigated for over three decades. However, experimental studies of the microscopic structure of SRCs were largely restricted due to moderate momentum-transfer kinematics in which it is very difficult to resolve SRCs due to competing processes such as final-state interactions (FSI), meson exchange currents (MEC) and isobar configurations (IC).

Recently, several high-energy, large-momentum-transfer measurements, along with companion theoretical studies, have made progress in identifying SRC pairs in nuclei and understanding their dynamics. The following is a short review of the recent studies of SRC using high energy and large momentum transfer reactions.

1.2.1 Inclusive experiments.

JLab/ Hall C experiment E89-008 [6] was an inclusive $A(e,e')$ measurement at $x_B > 1$, where $x_B = Q^2/2m\omega$ is the Bjorken scaling variable. The data were analyzed as a function of the y -scaling variable that is related in Plane Wave Impulse Approximation (PWIA) to the momentum of the struck proton in the nucleus. Relatively large high-momentum tails were observed. Some theoretical models tried to explain this by invoking short-range correlations [7]. Other theoretical models [8] explained the results in terms of Final State Interactions (FSI).

There are (e,e') measurements in the "dip" region, between the quasi-elastic peak and the delta region, at $x_B < 1$, which show an anomalously large transverse cross section. This has been cited as evidence for N-N correlations, although not necessarily short-range. ([9], [10] and [11]).

JLab/ Hall B experiments [3,4] observed Bjorken x_B scaling for ratios of inclusive (e,e') cross sections of nuclei A to the ${}^3\text{He}$ nucleus at $x_B > 1.4$. (see figure 1-1). This confirmed the earlier observation of scaling for nucleus-to-deuteron cross section ratios that were measured at SLAC [12]. The scaling suggests that the electrons probe high-momentum bound nucleons coming from local sources in nuclei (i.e. SRC) with properties generally independent of the non-correlated residual nucleus [7]. In the PWIA, $x_B > 1.4$ corresponds to hitting a proton with momentum above 275 MeV/c. The probability for a proton to be a member of a 2N-SRC was estimated from the inclusive (e,e') data to be $20 \pm 5\%$ for carbon [3,4]. By 2N we mean proton-proton (pp), proton-neutron (pn) and neutron-neutron (nn) pairs. The inclusive (e,e') measurement does not supply any information about the isospin structure of the 2N-SRC pairs. The second plateau in figure 1-1 at $x_B > 2$ corresponds in this model to 3N-SRC and was estimated by ref [4] to be an order of magnitude smaller than 2N-SRC.

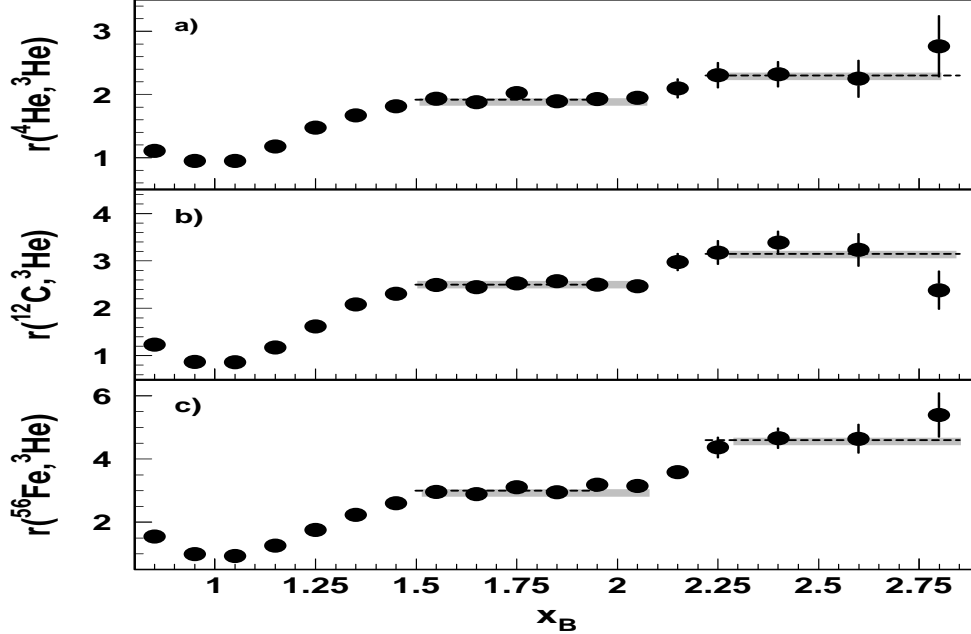


Figure 1-1: The cross section scaling $r = 3 \times \sigma[A(e, e')]/A \times \sigma[{}^3\text{He}(e, e')]$ as a function of x_B [4].

1.2.2 Semi-exclusive experiments.

The high-energy, large-momentum transfer (e,e'p) reaction is an experimental way to study the properties of bound nucleons in the nucleus. In the (e,e'p) reaction, the missing momentum and missing energy are determined. (See section 4.1 for definitions of missing momentum and missing energy). In PWIA, assuming only nucleonic contributions, these become the momentum and the binding energy of the bound nucleon before it was struck by the virtual photon. The initial and final state interactions (ISI/FSI) and non-nucleonic contributions can be minimized and/or calculated by choosing suitable kinematical conditions.

The large (e,e'p) data base reveals two universal features common to all nuclei:

- (i) The measured cross section to remove a proton from a well defined single particle shell is 60-70% of the Independent Particle Shell Model (IPM) prediction. The IPM is based upon the assumption that each nucleon moves independently in an average potential (mean field) induced by the surrounding nucleus. In this calculation FSI were taken into account [2] (see figure 1-2).
- (ii) For a missing momentum above ~ 300 MeV/c and missing energy above ~ 50 MeV, the measured strength is higher (up to an order of magnitude) than the predictions from the IPM calculations[14].

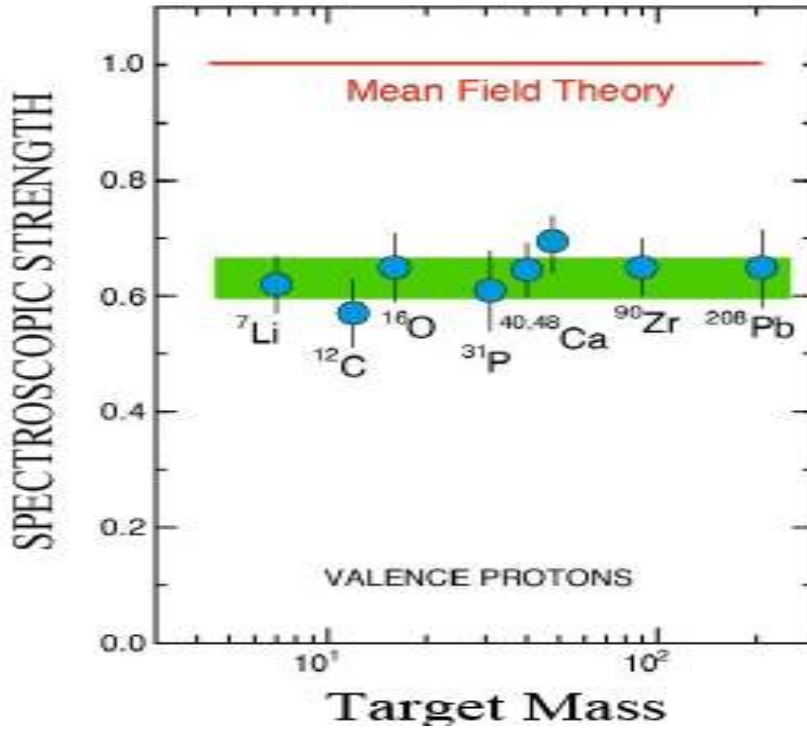


Figure 1-2. : The spectroscopic strength (which relates to the occupation of single-particle orbits by protons) vs. the target mass for the $(e,e'p)$ reaction [2]. The data are compared to IPM calculations.

Experiment E97-006 was performed at JLab/Hall C in order to study short-range correlations (SRC) in nuclei [13]. SRC lead to access strength of the spectral function (see definition in Eq. 1.2) at high momentum and energy and the depletion of single-particle states. In a $(e,e'p)$ experiment one can obtain the spectral function assuming PWIA and using an off-shell e-p cross section. However, since PWIA is broken, the signature of SRC at high initial momentum k and high removal energy E is often overwhelmed by contribution from re-scattering and the Δ -resonance. The SRC and the other process contribute differently in the parallel and perpendicular geometries, corresponding to the direction of the struck proton relative to the virtual photon. In this experiment $(e,e'p)$ data were taken for C, Al, Fe, Au in both parallel and perpendicular kinematics at $1 < x_B < 2$.

Experiment E97-006 measured the strength of the nuclear spectral function $S(k,E)$ at high nucleon momenta k and large removal energies E . This strength is related to the presence of short-range and tensor correlations, and was known hitherto only indirectly and with considerable uncertainty from the lack of strength of the independent-particle predictions in this kinematical regime.

The results from this experiment were compared to calculations by Benhar *et al.* [15]. In parallel kinematics it was found that at $k < 400$ MeV/c the data yield is smaller than predicted by the theory, while for $k > 400$ MeV/c the opposite is true. Overall, the strength agrees well with the theoretical predictions.

1.2.3 Triple coincidence experiments.

New generations of "kinematically complete" experiments which measure the scattered nucleon in coincidence with a correlated nucleon have been performed. This category includes (e, e'pp) measurements from MAMI and NIKHEF [16-23], and (γ ,N-N) from TAGX and LEGS [24, 25]. These new virtual photon measurements had the required energy resolution to identify the shells from which the proton pair was knocked out and to study the strength due to short-range nucleon-nucleon correlations. Recent model calculations [26, 27] attribute the correlation to central (Jastrow type) and tensor components. Note that all the NIKHEF and Mainz triple coincidence measurements were performed at low Q^2 and $x_B < 1$. For the experiment discussed in this thesis, the high Q^2 and $x_B > 1$ are essential elements. The advantages of the high Q^2 and $x_B > 1$ are discussed in section 1.3.3.

The first high Q^2 triple coincidence measurement was experiment E850 at BNL which studied the reaction $^{12}\text{C}(p,2pn)$ using a few GeV/c proton beam [28-30]. The two outgoing high p_T protons (corresponding to 90° c.m. scattering) were detected in coincidence with a neutron with a momentum larger than 320 MeV/c. About half of the hard scattering $^{12}\text{C}(p,2p)$ events were found to be in coincidence with one neutron emitted into the back hemisphere. For the quasi elastic (p, 2p) events, a correlation between the direction of the missing momentum and the emitted neutron momentum was observed [28] (see figure 1-3). The experimental observation of these directional correlations indicated the dominance of short-range correlations in this regime.

Recent analysis of these data concluded that if a nucleon with momentum between 275-550 MeV/c is removed from the nucleus using a high momentum and energy transfer probe, at least 74% of the time it originates from np-SRCs. This experiment observed direct np-SRC but also set a 13% upper limit on the contribution of pp-SRC to the high momenta tails of protons in ^{12}C [31].

Experiment (E850) also measured the longitudinal components of the c.m. momentum of the correlated pn pair [32]. Figure 1-4 shows the $p_{c.m.}^z$ distribution with the centroid at -0.013 ± 0.027 GeV/c. The spread of the distribution is $\sigma = 0.143 \pm 0.017$ GeV/c.

This result is in good agreement with calculations by Ciofi degli Atti *et al.* [33], which estimates the contribution of c.m. motion of correlated pairs in ^{12}C to the spectral function at large momentum and removal energies. Ciofi *et al.* assumed Gaussian distribution of the c.m. of the correlated pair and deduced a width of 139 MeV/c.

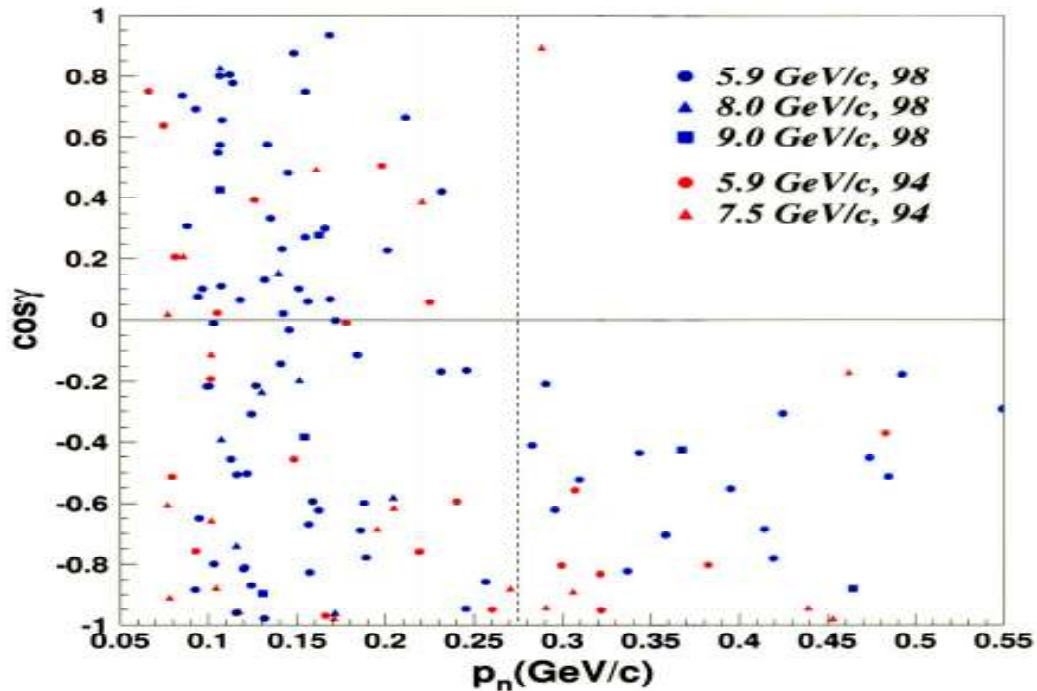


Figure 1-3: The correlation between p_n and its direction γ relative to the direction of the struck proton in the quasi-elastic (p,2p) reaction. Data labeled by 94 and 98 are from Refs. [28,30], respectively. The momenta are the beam momenta. The dotted vertical line corresponds to $p_n = 275$ MeV/c.

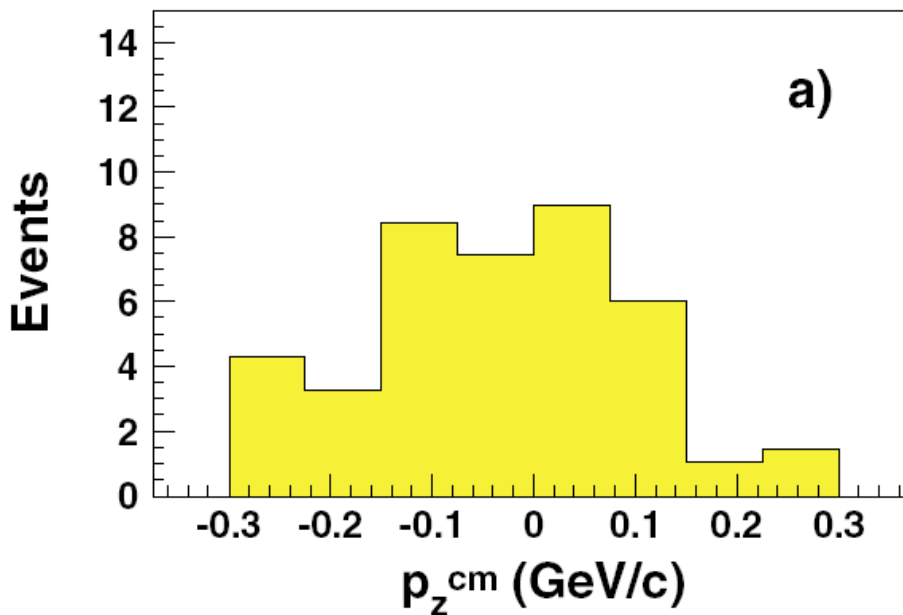


Figure 1-4: The c.m. width of the correlated n - p pairs in ^{12}C . The data represents the distribution of the longitudinal component of the c.m. width p_z^{cm} from $^{12}\text{C}(p,2pn)$ measurement at BNL.

1.3 This experiment.

1.3.1 Introduction.

The electron-nucleus interaction is better understood than the nucleon-nucleus interaction. Also, the electromagnetic interaction is weak compared to the hadronic one, and hence electrons probe the entire volume of the nucleus while hadrons tend to interact on the nuclear surface.

This thesis reports an experiment to study SRC in a similar manner as the hadron-nucleus scattering experiment at BNL. This experiment is significantly more precise and has a much better statistics than the experiment at BNL. Hall A has an excellent setup for measuring (e,e'p) scattering. We added a third arm consisting of a large acceptance magnetic spectrometer to measure the protons, combined with a solid-angle matched array of counters to measure neutrons in coincidence with the outgoing high momentum electron and proton. Just as for the (p,2pn) reaction, we measured the full kinematics of the (e,e'pp) reaction, but with much higher accuracy as enabled by the JLab facilities. As in (e,e'p), we can deduce the momentum of the struck proton. We also measured the momentum and direction of the additional neutron or proton in coincidence with the outgoing e and p. This allowed us to measure the fraction of (e,e'p) events in which correlated nucleons are observed, as a function of the momentum of the proton in the nucleus. It also allowed us to make a comparison between pn and pp correlated pairs in nuclei.

1.3.2 Impulse approximation description of the $^{12}\text{C}(e,e'pp)$ reaction.

We refer to N-N SRC as a pre-existing pair of nucleons which have high back-to-back momenta balancing each other. In this case: $\vec{p}_1 \approx -\vec{p}_2$, $p_1, p_2 > k_F$, and $p_{c.m.} \approx 0$, where in the laboratory system p_1 and p_2 are the momenta of the two nucleons and $p_{c.m.}$ is their c.m. momenta, k_F is the Fermi momentum surface [34] (See figure 1-5).

In the impulse approximation, a virtual photon with a large four-momentum transfer Q^2 is absorbed by one of the protons in a pp-SRC pair. This supplies the energy required to break the pair and remove both protons from the nucleus (see figure 1-5).

The pre-existing pair is identified by a recoil proton detected in coincidence with the (e,e'p) reaction which has a high momentum (\vec{p}_{rec}) in the direction of the (e,e'p) missing momentum (\vec{p}_{miss}). In the PWIA, the measured momenta \vec{p}_{rec} and $-\vec{p}_{miss}$, are equal to the momenta \vec{p}_2 and \vec{p}_1 of the proton pair in their initial state.

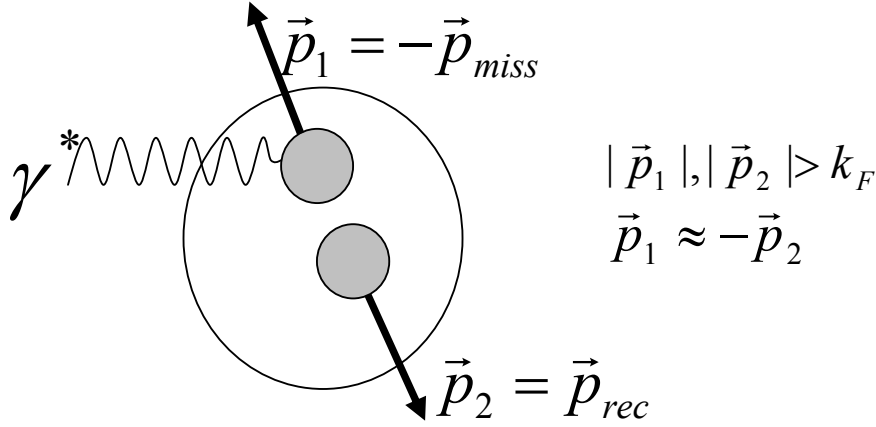


Figure 1-5: The Impulse Approximation Description of the $^{12}\text{C}(e,e'pp)$ reaction.

The cross section for the reaction when a proton is knocked out of the nucleus and a spectator nucleon in the final state is detected in coincidence with the scattered electron and proton can be represented within the PWIA as follows:

$$\frac{d\sigma}{dE_e' d\Omega_e d^3(p_f / E_f) d^3(p_{rec} / E_{rec})} = K_d \sigma_{ep}(Q^2, \varepsilon, E_{miss}, \vec{p}_{miss}) \cdot D(E_{miss}, \vec{p}_{miss}, \vec{p}_{rec}) \quad (\text{Eq. 1.1})$$

Where K_d is a kinematical factor $\varepsilon = [1 + 2 \times (q^2 / Q^2) \tan^2(\theta_e / 2)]^{-1}$ and σ_{ep} describes the electron scattering on an off-shell proton. E_f and p_f are the energy and momentum of the proton in the (e,e'p) reaction.

The spectral function is the probability to find inside the nucleus a nucleon with missing momentum \vec{p}_{miss} and missing energy E_{miss} . The decay function D represents the joint probability to find a nucleon with \vec{p}_{miss} and E_{miss} and where the residual $A-1$ nuclear state contains the spectator nucleon with momentum \vec{p}_{rec} . The decay function is related to the spectral function of (e,e'p) reaction in the following way:

$$\int D(E_{miss}, \vec{p}_{miss}, \vec{p}_{rec}) d^3 p_{rec} = S(E_{miss}, \vec{p}_{miss}). \quad (\text{Eq. 1.2})$$

The decay function defines the quantities which can be studied experimentally by a triple coincidence measurement within the PWIA assumption. The decay function can also be expressed as a function of $\vec{p}_{rec}(p_{rec}^{\pm}, p_{rec}^t)$ and $\vec{p}_{miss}(p_{miss}^{\pm}, p_{miss}^t)$. These are the light cone variables in which any four-momentum k can be represented as $k \equiv k(k^+, k^-, k^t)$ where k^0 is the energy $k^{\pm} = k^0 \pm k^z$, and the z and t components are defined along the direction and perpendicular to the direction of the transferred momentum \vec{q} (the virtual photon momentum).

1.3.3 Suppression of competing effects.

The interpretation of the data in terms of SRC is plagued by contributions from competing processes such as final-state interactions (FSI), meson exchange currents (MEC) and isobar configurations (IC) [35, 36, and 37]. Figure 1-6 shows diagrams of the desired SRC process and the competing processes. The kinematics for this experiment were chosen to minimize these effects. The MEC diagram diminishes as $1/Q^2$ compared to SRC diagram [38, 39] and is suppressed for the (e,e'pp) reaction. A large Q^2 is also required to probe high missing momentum in the (e,e'p) reaction with $x_B > 1$, which also drastically reduces the isobar production contribution [42].

The large Q^2 chosen, produced a high energy proton approximately in the direction of the virtual photon, in coincidence with the correlated partner proton that emerges roughly opposite to the initial momentum of the struck proton. The FSI consist of two components: the interaction of the struck proton with its correlated partner nucleon in the pair, and the interaction with other nucleons in the A-2 residual nucleus.

An important feature of the kinematics we are considering (large Q^2 , $p_f \sim 1$ GeV/c) is the applicability of the Eikonal approximation for the description of the rescattering. In this approximation, small angle rescattering of 1 GeV/c nucleons causes mainly transfer of momentum in the plane transverse to the direction of their high momentum (see ref [39-41]). This allows us to control, to some extent, the amount of FSI by selecting the angle between the struck proton momentum and the incident virtual photon \vec{q} . The best geometry for the suppression of FSI would be the parallel kinematics, where the large \vec{p}_i and large $|\vec{q}|$ combines to a very large p_f which cannot be mimicked by FSI. Unfortunately, in this geometry, the large \vec{p}_i and large \vec{q} create a low x_B which entails contamination from resonance production.

In view of the above, we chose kinematics which we call "almost anti-parallel" in which we look at high momentum target protons (300-500 MeV/c) that are almost anti-parallel to the \vec{q} direction ($x_B > 1$). If they are fully correlated with another spectator nucleon and the pair is at rest, and if we choose the direction of \vec{q} properly, the spectator will be ejected at about 90° to the beam. This specific kinematical setup is a good compromise between the singles rates and the suppression of FSI. For light nuclei, $A < 16$, calculations of FSI diagrams within the generalized Eikonal approximation [42] shows that in addition to $x_B > 1$, the condition:

$$\left| p_{miss}^z + \frac{q_0}{q} E_{miss} \right| \geq k_F$$

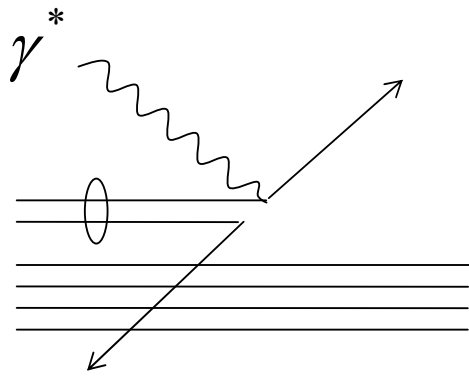
will confine the rescattering with another nucleon to within short-range. As a result the FSI will take place mainly with the nearby partner nucleon in the correlation. Thus, it will not affect the determined isospin and the c.m. motion of the SRC pair. An important part of this measurement is to determine the isospin strength of the SRC pairs. Note that the interactions between nucleons in a pair conserve the isospin structure of the pair. This means that a pp pairs remains a pp pair, even with FSI.

The FSI of the recoil proton with the rest of the nucleus is strongly suppressed due to Pauli blocking [43]. The absorptive (imaginary) part of the FSI can reduce the $^{12}\text{C}(e,e'pp)/^{12}\text{C}(e,e'p)$ ratio, while single charge exchange can turn $^{12}\text{C}(e,e'pn)$ events into $^{12}\text{C}(e,e'pp)$ events, thereby increasing the measured ratio. Our estimates of these FSI effects, based on a Glauber approximation using the method of [39,44] which is described in Appendix C, indicate that the absorption and single charge exchange are each about 20% corrections and compensate each other so that the net effect is small compared to the uncertainties in the measurement. This conclusion is backed by the c.m. motion result, which gives widths for all the components that are narrow and internally consistent (see discussion in chapter 4).

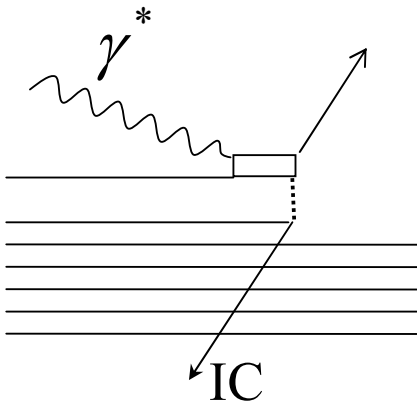
The elastic (real) part of the FSI with the A-2 nucleons can alter the momenta, such as to make $-\vec{p}_{miss} \neq \vec{p}_1$, $\vec{p}_{rec} \neq \vec{p}_2$, and hence $\vec{p}_{c.m.}$ different from $\vec{p}_1 + \vec{p}_2$. The elastic FSIs between members of the SRC pair do not change the c.m. momentum of the pair as reconstructed from the momentum of the detected particles. The FSI with the A-2 is small, and the FSI within the pair do not change the c.m. motion. Therefore the reconstructed \vec{p}_{cm} reflects the genuine pair c.m. motion. The data presented in this thesis supports this conclusion, as will be discussed in chapter 4.

All this leads to an exclusive measurement of three particles in coincidence in a region of high energy transfer, high Q^2 and $x_B > 1$. We choose to pay the price of the small cross section at $x_B > 1$ in order to decrease contributions from resonance effects.

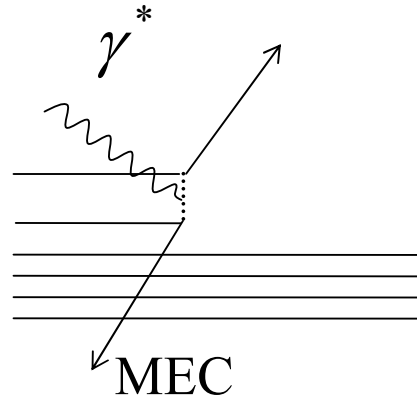
In a triple coincidence measurement, in general, the assignment of the initial momenta of the two detected nucleons is not unique, depending on whether the virtual photon is being absorbed by one or the other nucleons. There are two amplitudes which add coherently. The ambiguity is a problem in low Q^2 measurements. In the specific case of this proposed large Q^2 measurement, the high momentum transferred identifies clearly the struck nucleon that absorbed the photon from the correlated "backward" emitted partner. In principle one has to coherently add two amplitudes, but in this case one of the amplitude is too small to be considered. This is another important advantage to doing the measurement at high Q^2 .



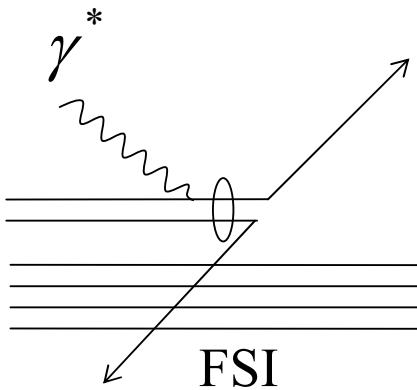
SRC



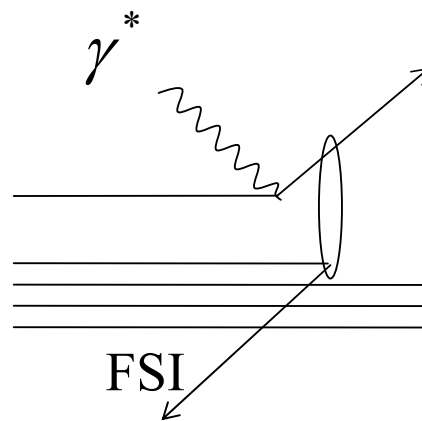
IC



MEC



FSI



FSI

Figure 1-6 : Feynman diagram of different possible reaction channels.

1.3.4 The selected kinematics for the experiment.

This experiment was performed in Hall A of the Thomas Jefferson National Accelerator Facility (JLab) using an incident electron beam of 4.627 GeV with a current between 5 and 50 μA . The target was a 0.25 mm thick graphite sheet rotated 70° from perpendicular to the beam line to minimize the material through which the recoiling protons passed. The two Hall A high-resolution spectrometers (HRS) [45] were used to measure the $^{12}\text{C}(e,e'p)$ reaction. Scattered electrons were detected in the left HRS (HRS-L) at a central scattering angle (momentum) of 19.5° ($3.724 \text{ GeV}/c$). This corresponds to the quasi-free knockout of a single proton with transferred three-momentum $|\vec{q}| = 1.65 \text{ GeV}/c$, transferred energy $\omega = 0.865 \text{ GeV}$, $Q^2 = 2 (\text{GeV}/c)^2$, and $x_B = Q^2/2m\omega = 1.2$ where m is the mass of a proton. Knocked-out protons were detected using the right HRS (HRS-R) which was set at 3 different combinations of central angle and momentum: 40.1° & $1.45 \text{ GeV}/c$, 35° & $1.42 \text{ GeV}/c$, and 32.0° & $1.36 \text{ GeV}/c$. These 3 kinematics settings correspond to central missing-momentum values in the range of 300-600 MeV/c.

A third, large-acceptance spectrometer, BigBite, was used to detect recoiling protons in the $^{12}\text{C}(e,e'pp)$ events. BigBite was located at an angle of 99° and 1.1 m from the target with a resulting angular acceptance of about 96 msr and a nominal momentum acceptance from 0.25 to 0.9 GeV/c. The kinematics for the 3 setups are shown in figure 1-7.

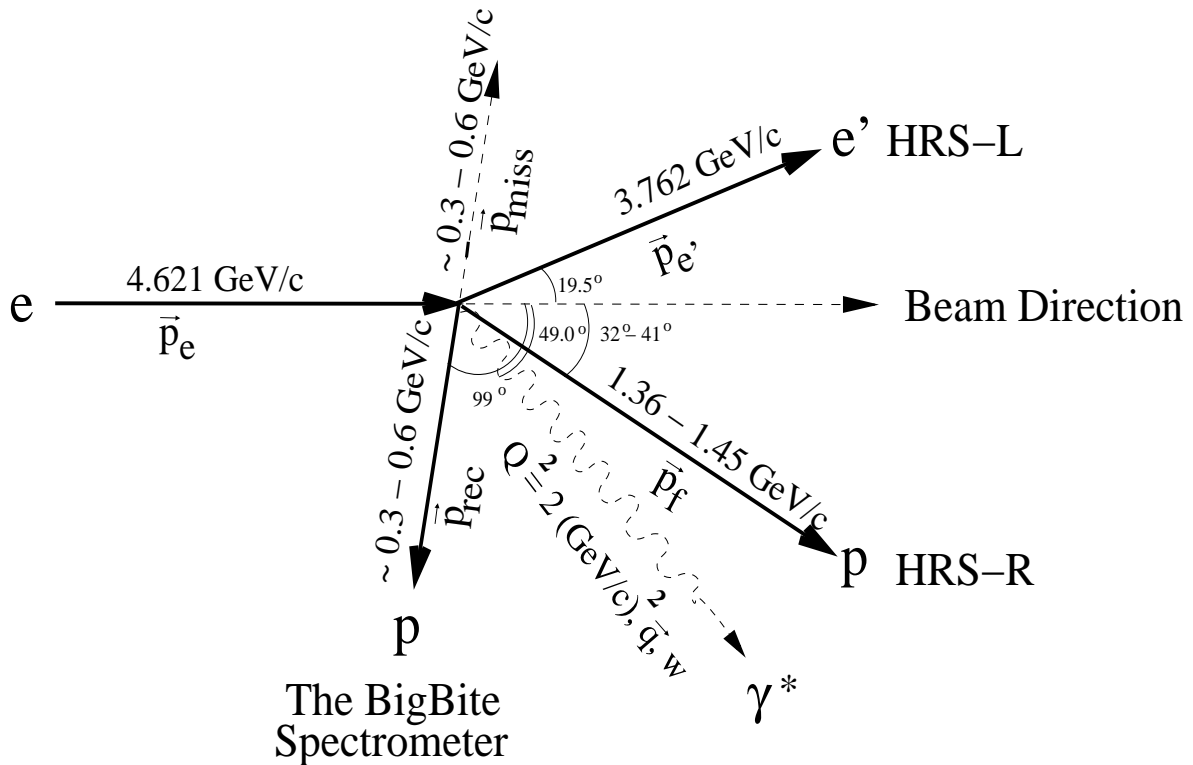


Figure 1-7: A vector diagram of the kinematics of the $^{12}\text{C}(e,e'pp)$ measurement.

Chapter 2

Apparatus and Experimental Setup

This work represents the first physics experiment utilizing BigBite as a large acceptance spectrometer in Hall A of the Thomas Jefferson National Accelerator Facility [45]. The experiment was performed during the winter of 2005. The setup included BigBite, the Hall A High Resolution Spectrometer (HRS) pair and a dedicated neutron detector. The first part of this chapter describes the electron accelerator (CEBAF) at the Jefferson Lab and the Hall A standard experimental setup. The latter part presents the design and building of the BigBite spectrometer for the SRC experiment. A neutron detector was used to measure the $^{12}\text{C}(e,e'pn)$ reaction simultaneously with the $^{12}\text{C}(e,e'pp)$ reaction. The detector and the $^{12}\text{C}(e,e'pn)$ results are not reported in this work.

2.1 CEBAF Accelerator

The Continuous Electron Beam Accelerator Facility (CEBAF) is a super-conducting high-current, high-duty factor electron accelerator with maximum beam energy of about 6 GeV (see figure 2-1). The polarized source provides up to 78 % polarized electrons with a maximum current of 200 μA . The electrons are pre-accelerated to 45 MeV by the injector. The beam is then further accelerated by the two main linacs, which are connected by 180° recirculation arcs. Up to four re-circulations (5-pass) are possible. Each linac consists of three cryo modules, each containing eight cryo units consisting of five cell elliptical cavities. The cryo-units are made of Niobium and are cooled to 2°K . They are driven by an RF frequency of 1.497 GHz. The electron beam can be divided in the beam switch-yard to the three experimental halls, A, B and C [46]. In this experiment we used an electron beam of 1.204 GeV (1-pass) and 2.345 GeV (2-pass) for calibration and a 4.627 GeV (5-pass) beam for production.

2.2 Hall A and its standard equipment.

A schematic layout of Experimental Hall A [45] is shown in figure 2-2. The hall is circular in shape with a diameter of 53 m. Beam enters the hall from the lower left hand corner of the figure. The beam line is instrumented with beam position and beam current monitors (see section 2.2.1). The scattering chamber is located in the center of the hall. The cryogenic target systems are mounted inside the scattering chamber along with sub-systems for cooling, gas handling, temperature and pressure monitoring, target control and motion.

Hall A has two High Resolution Spectrometers (HRSs) (See figure 2-2 and section 2.3.3). Both of these devices provide a momentum resolution of better than $\Delta p/p = 2 \cdot 10^{-4}$ and a horizontal angular resolution of better than 2 mrad at a central momentum of 4 GeV/c. The present base instrumentation in Hall A has been used with great success for experiments which require high luminosity and high resolution in momentum and/or angles. The detection of an electron and a proton within a small time window set by the experiment is a signature of a coincidence (e,e'p) event.

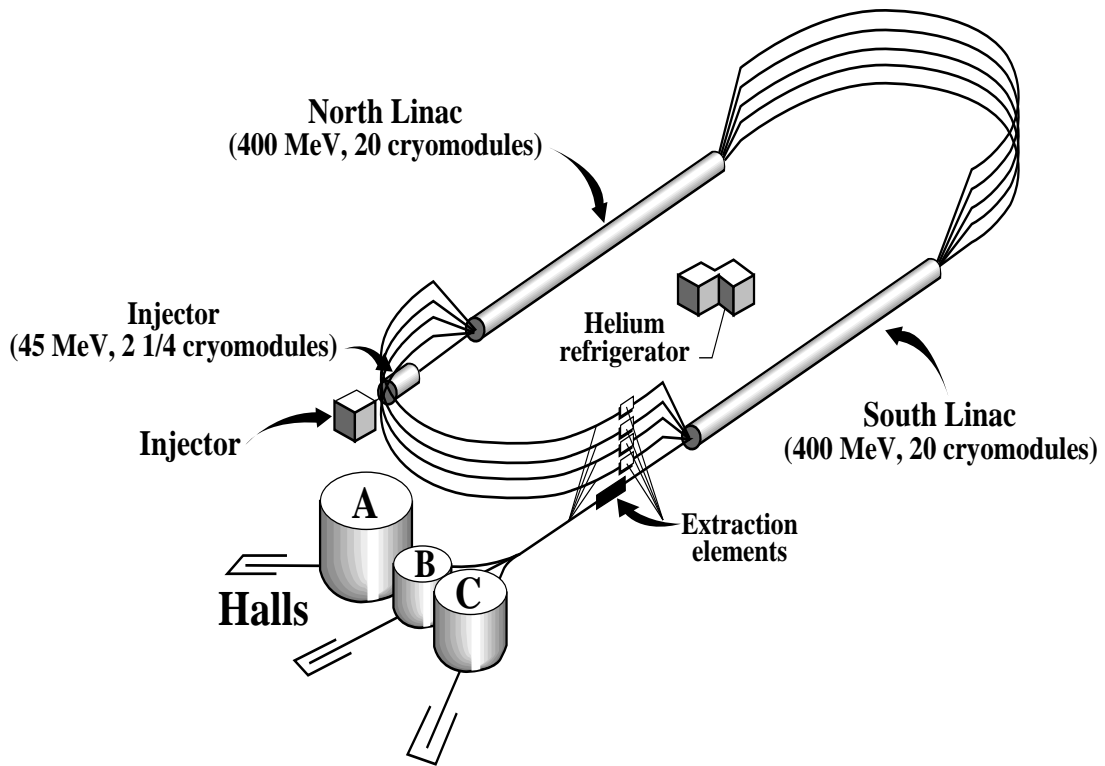


Figure 2-1: Schematic layout of Jlab accelerator.

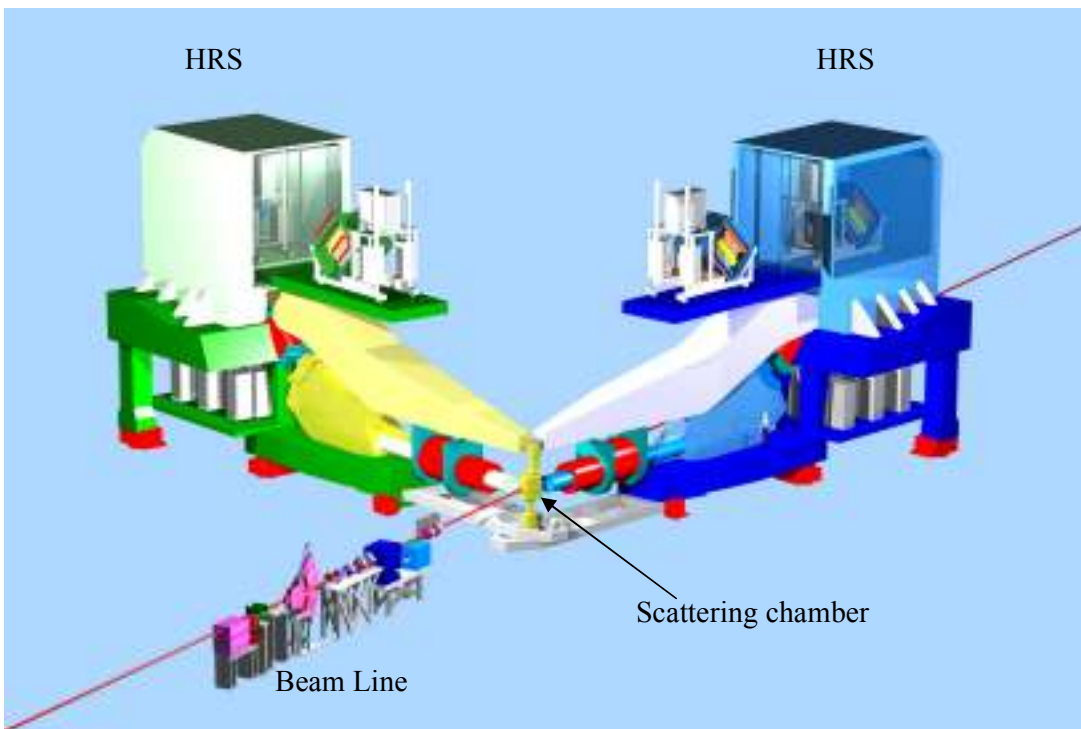


Figure 2-2: Schematic layout of Hall A

2.2.1 The Beam Line

The instrumentation along the beam line (shown in figure 2-3) consists of various elements necessary to transport the electron beam onto the target and into the dump, and to measure simultaneously the relevant properties of the beam. The beam instruments allow to control and determine the energy, current, polarization, position, direction, size, and stability of the beam at the Hall A target location.

The beam current delivered to the hall is measured by two RF Beam Cavity Monitors (BCMs) placed 24.5 m upstream of the target. When the cavities are tuned to the frequency of the beam (1497 MHz), their output voltage levels are proportional to the beam current.

The Beam position monitor (BPM) is a device for non-invasive continuous measurement of the position of the beam. Each of the employed BPMs has a cavity with four antennas; each oriented parallel to the nominal beam direction and located symmetrically around the nominal beam position. The electron beam passing through the cavity induced signals in the antennae with amplitudes inversely proportional to the distance from the beam to each antenna. Analog-to-Digital Converter (ADC) readouts from pairs of antennae are combined with calibration coefficients to yield the beam position in each of the two directions. The intrinsic beam spot size is very small (100 micrometer) and can cause local damage to the liquid cryo and other temperature sensitive target cells at high current. For the liquid cryo targets, the beam is rastered on target with amplitude of a few mm to prevent the target overheating.

The absolute beam energy is measured by two independent methods: the arc energy method and the ep method. The arc energy method measures the energy as a function of the bend angle of the arc and the field integral of eight-dipole magnets located in the 40 meter arc between the accelerator and the Hall A end station.

The ep method, determines the energy based on the angles of particles in an electron proton elastic reaction. This method requires the beam to be directed to a stand-alone device in the beam line 17 m upstream of the target.

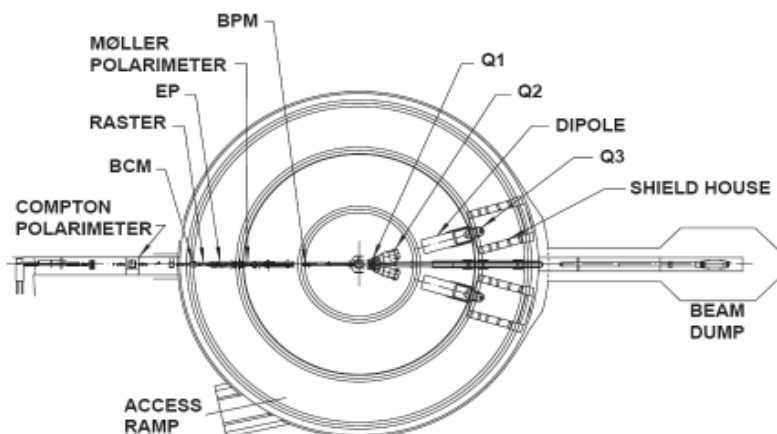


Figure 2-3. Schematic layout of Hall A, indicating the location of the raster, the ep energy measurement system, the beam current monitors (BCM) and the beam position monitors (BPM) upstream of the target. Also indicated are the locations of the components of one of the high-resolution spectrometers (Q1, Q2, dipole, Q3 and shield house) and of the beam dump. The beam polarimeters shown in this figure were not used in this experiment.

2.2.2 The scattering chamber and the target.

The cryogenic target system is mounted inside the scattering chamber along with sub-systems for cooling, gas handling, temperature and pressure monitoring, target control and motion. The basic Hall A cryogenic target has three independent target loops: a liquid hydrogen LH2 loop, a liquid deuterium LD2 loop and a gaseous helium loop. Each of the two liquid loops has two aluminum cylindrical target cells mounted on the target ladder. The cells are 63.5 mm in diameter and can be either 4 or 15 cm long. The side walls of the cells are 178 nm thick, with entrance and exit windows approximately 71 and 102 nm thick, respectively. The upstream window of the scattering chamber consists of a thick ring holder with an inner diameter of 19 mm, large enough for the beam to pass through.

Scattering chamber

A new scattering chamber was designed and constructed for use in Hall A for experiment E01-015. The new chamber was required in order to fully utilize the large vertical acceptance of BigBite. The chamber was constructed so that it can be used with the conventional Hall A pivot post for experiments requiring a large vertical acceptance. The chamber outer diameter was 1.143 m and its height was 0.991 m. The vertical opening of the windows was 37.1 cm. See figure 2-4 for a schematic view of the scattering chamber.

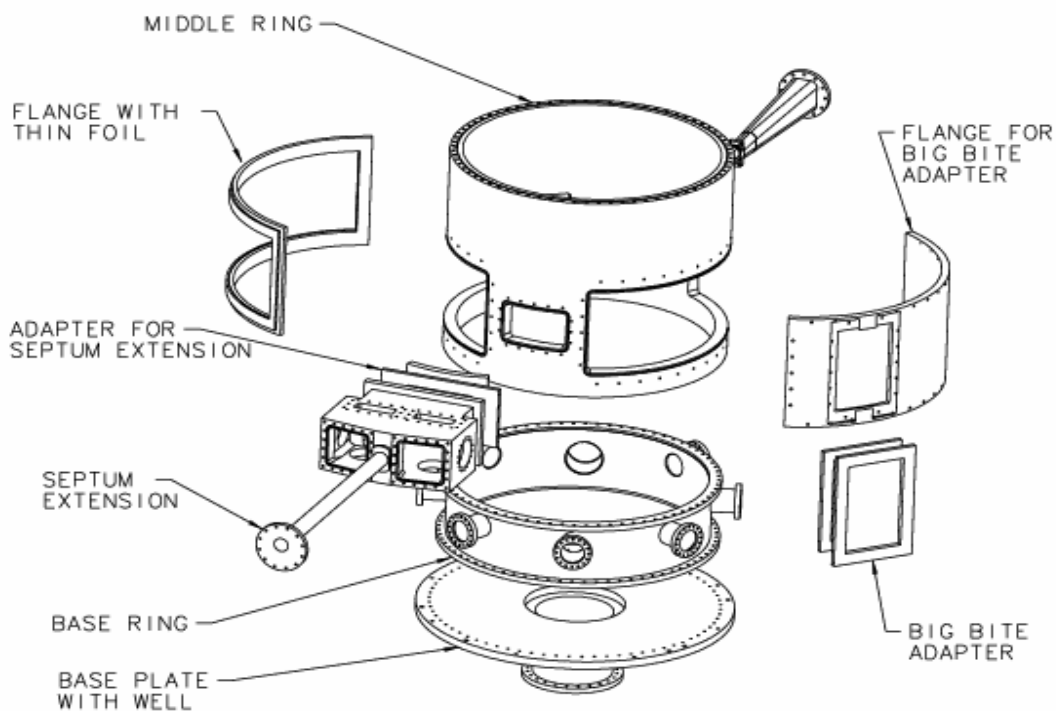


Figure 2-4: Exploded view of the scattering chamber. The septum extension was not used in this experiment.

Target

The target used during the production data taking was a thin (0.25 mm) carbon foil tilted 20° to the nominal beam direction (see figure 2-5). The 20° angle was chosen as such in order to minimize the energy loss of the two emerging protons. The energy loss is dominated by the slower proton, which is detected by BigBite at a momentum range of 250-700 MeV/c.

Other targets employed in the experiment were: a 1 mm carbon foil target, set perpendicular to the beam (used for the HRSs calibration), a 4 cm and 15 cm long Liquid Deuterium targets (used for the Neutron array calibration), a 4 cm and 15 cm long Liquid Hydrogen targets (used for ep Elastic calibration), a dummy empty aluminum target and a BeO target. The targets were arranged on a vertical stack which can be moved from one position to another with a remote control. All target positions were surveyed before and after the experiment. The motion during vacuum pump-down and cool-down is monitored and corrected for. The targets were centered to about 1mm with a typical position precision of 0.5 mm.

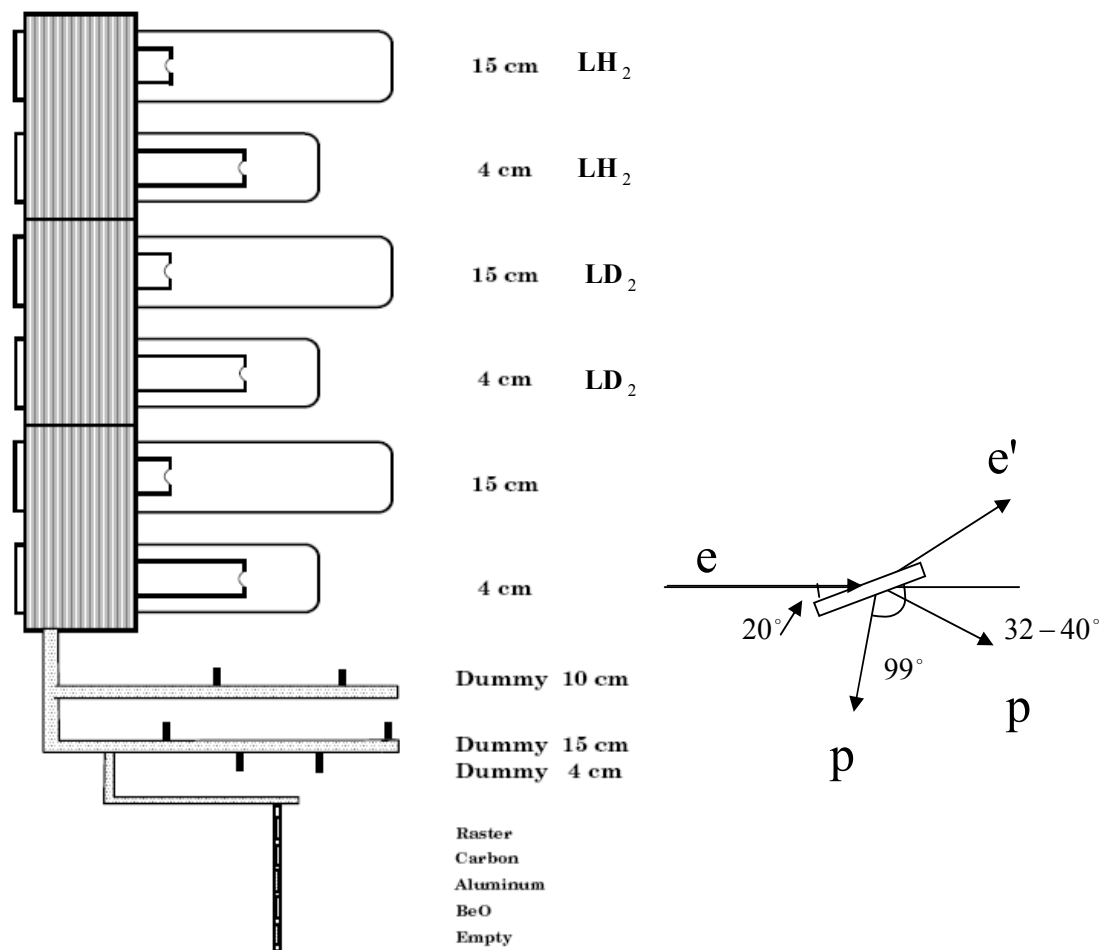


Figure 2-5: Schematic view of the Hall A target ladder for E01-015 and the targets used for the experiment (Left). Schematic view of the tilted carbon target (Right).

2.2.3 The High Resolution Spectrometers.

The Hall A spectrometers were designed to measure the particle momentum and angle with high resolution. Each of the two spectrometers consists of three quadrupoles (Q1, Q2 and Q3) and one dipole (D). These superconducting magnets are arranged in the QQDQ configuration (see figure 2-6). The bending angle of the pole is 45° in the vertical plane. The momentum range is from 0.3 to 4 GeV/c. The relative momentum acceptance is about $\Delta p / p = \pm 4.5\%$ with a resolution of $\Delta p / p = 2 \times 10^{-4}$. The scattering angle of the detected particles is varied through rotation of the spectrometers around the hall center, with a central scattering angle range of $12.5^\circ - 150^\circ$. In this experiment the left HRS was set at 19.5° and the right HRS was set at 3 different angles - 32° , 35.8° and 40.1° . Nominal acceptance of the spectrometers is ± 28 mrad in the horizontal direction and ± 60 mrad in the vertical direction.

The detector package of each spectrometer has the following components: two scintillators for trigger and time-of-flight measurements, and a pair of Vertical Drift Chambers (VDC) for charged particle tracking information. During this experiment, the electron HRS included an additional gas Cerenkov detector for particle identification, while the hadron HRS had pre-shower and shower detectors. The information from the pre-shower and shower detectors was not used for analysis. See figure 2-7 for a schematic layout of the detector packages installed on the two HRSs.

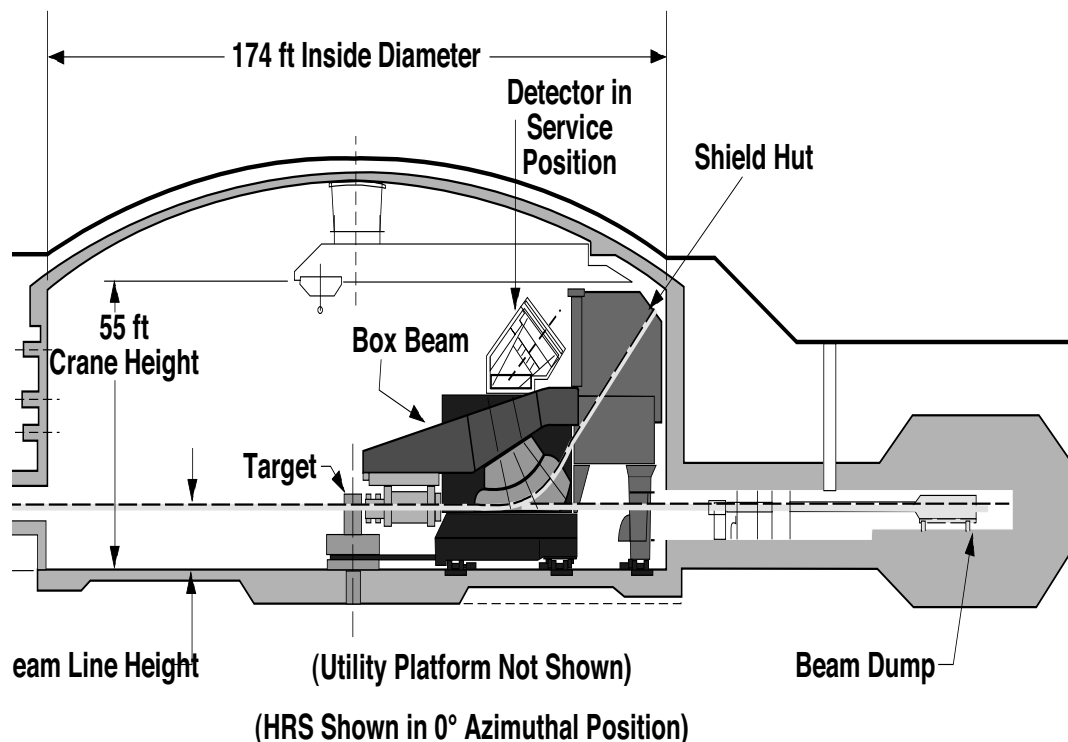


Figure 2-6: Schematic layout of Hall A High Resolution Spectrometer (HRS)

Vertical Drift Chambers

The vertical Drift Chambers [45] provides a precise measurement of the position and angle of incidence of charged particles at the spectrometer focal planes. The tracking information from the VDC measurement is combined with the spectrometer optics to reconstruct the position, angle and momentum of the particle in the target.

Each spectrometer has a pair of identical VDCs. The VDCs are composed of two wire planes in a standard UV configuration – the wires of each plane are oriented at 90° to one another, and each plane is oriented at 45° with respect to the nominal particle trajectories. There are a total of 386 sense wires in each plane. A charged particle crossing the VDC ionizes atoms in the gas mixture, creating a trace of released electrons. The electrons are accelerated by the electric field created by the high voltage and drift along the field lines towards the wires. In the vicinity of the sense wires the drifting electrons initiate electron avalanches. The electron avalanches hit the wires and induce wire signals, which are amplified, discriminated and sent to multihit TDCs.

Scintillators

There are two planes of trigger scintillators S1 and S2 in each spectrometer. S1 is located 1.5 m away from the center of the first VDC plane. The S2 is 2 m away from S1. S1 and S2 each consist of six paddles. The active area of each S1 paddle is about 29.5 cm by 35.5 cm. The active area of each S2 paddle is about 37.0 cm by 54 cm. These paddles are made of 5mm thick plastic scintillator. A 2-inch photo multiplier at each side is used to collect the photons and generate signals for both the Analog-Digital-Converter (ADC) and Time-Digital Converter (TDC).

The scintillators are mainly used to generate triggers for the data acquisition system. The time resolution of each plane is about 0.3 nsec (σ). Beside the use for trigger purpose, the scintillators can also be used for particle identification. Time-of-flight (TOF) between the S1 and S2 planes can be used to measure the particles speed β in terms of the light speed c in the vacuum. Another use of the scintillator detectors was in the calculation of the reaction time at the target. By subtracting the electron TOF from the left HRS S1, the reaction time was calculated with a resolution of 0.3 ns.

Gas Cerenkov counters.

Two similar threshold Gas Cerenkov counters are installed as a part of the particle identification equipment in the focal plane detectors of the High Resolution Spectrometers (HRS). Each counters' housing is made in steel with thin entry and exit windows made of Tedlar. Light weight spherical mirrors have also been built resulting in a very thin total thickness traversed by particles. The counters are operated at atmospheric pressure with CO_2 . These two counters have identical sections but different thicknesses, 1000 mm for the hadron arm and 1500 mm for the electron arm. These are gas Cerenkov detectors which are used as threshold counters. The refraction index of the gas is chosen in order to give maximum light output for electrons and to be inefficient to other particles like pions. With CO_2 at normal pressure, the refraction index is $n = 1.00041$ which gives a threshold of $p_{min} = 17 \text{ MeV}/c$ for electrons and $p_{min} = 4.8 \text{ GeV}/c$ for pions.

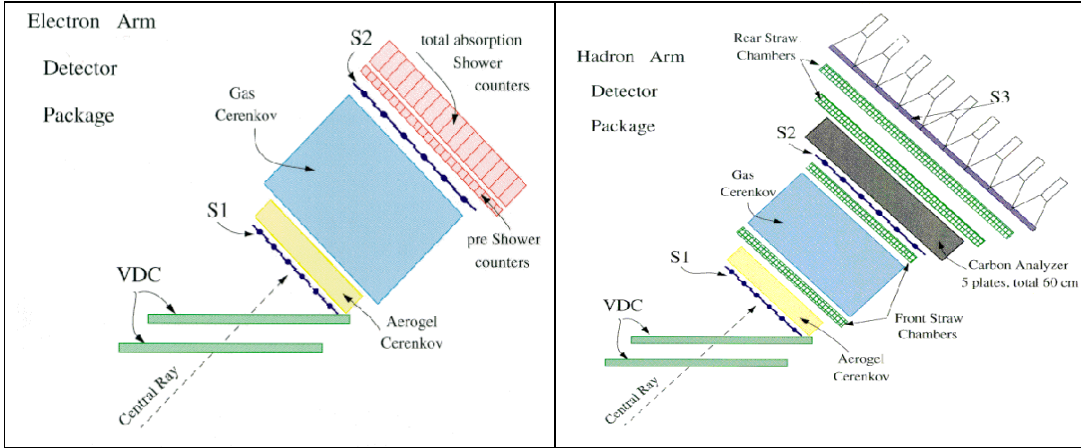


Figure 2-7: A schematic layout of the typical detector packages for the electron (left) and hadron (right) high resolution spectrometers. Note that not all of these detectors were utilized during this experiment.

2.3 The large acceptance BigBite spectrometer.

The new BigBite spectrometer in Jefferson lab's Hall A consisted of a large acceptance, non-focusing dipole magnet and various detector planes. For this experiment we used 3 scintillator planes –Auxiliary, ΔE and E. The ΔE and E planes together are referred to as the trigger plane. The large angular and momentum acceptance of BigBite complements the two High Resolution Spectrometers (HRSSs) already present in Hall A for use in three-arm measurements which require large momentum and large angular acceptances. The experiment reported here was the commissioning experiment of BigBite at Jefferson Lab.

2.3.1 Design and building of BigBite for the SRC experiment.

BigBite was designed to identify charged particles and measure their momentum and their angle. Timing, hit position and energy deposited in the scintillators are all used to measure the in-coming particles direction and momentum.

A non-focusing magnetic dipole ($B = 0.93$ T), was used to bend the charged particles path before they hit the detector planes. The momentum of a particle in a magnetic field p is proportional to the path radius of curvature R , and is given by:

$$p = eBR \quad (\text{Eq. 2-1}).$$

Utilizing segmented scintillator planes allowed hit bar number and the timing differences between left and right PMTs to be used to calculate the hit position in three axes [47].

The size and direction of the particle momentum was reconstructed using the hit pattern information of each scintillator plane which was used to reconstruct the particle path inside the magnetic field (see Appendix A). The momentum of the particle was also calculated by measuring TOF along a known distance (i.e. between different scintillator planes or from the target to one of the scintillator planes). The best momentum resolution was achieved by measuring the TOF between the target and the scintillator plane which was furthest from the target, while other methods were mostly used to filter background noise.

Particle Identification was done in two ways - by comparing the TOF and momentum as determined by the trajectories in the magnetic field and by measuring the energy deposited in the E and ΔE planes. The ΔE and E counters were 30 mm and 3mm thick, and as their names suggests, the ΔE and E planes were designed such that the ΔE scintillators absorbed only a fraction (ΔE) of the particle initial energy, while the E scintillators were designed to absorb most or all of the particle energy. More details about the design, building and testing of BigBite can be found in [47].

The Auxiliary plane

The Auxiliary plane (shown in figures 2-8, 2-9 and 2-10) [48], consisted of 56 scintillator bars. Each scintillator bar had dimensions $350 \times 25 \times 2.5 \text{ mm}^3$ and was coupled using a light-guide to a PMT on one end. The scintillators were arranged in a staggered configuration (see figure 2-9). The PMTs were shielded using soft iron cylinders. The PMTs were Hamamatsu-R1450, which are 19 mm diameter, 10 stage linear focused tubes. The gain was 5×10^6 , the quantum efficiency $QE \approx 28\%$ at 420 nm, the rise time was 1.8 ns, and the transit-time spread was 0.76 ns. The PMT base voltage divider chain was configured for high rate. The first 3 stages were zener-diode stabilized. These PMTs have been tested at 5 MHz.

The dominant consideration which determined the size/number of scintillators in the auxiliary plane was the singles rates and resolution. Our estimation was about 5-10 MHz for the full acceptance. With 56 counters, we expected an average rate of about 100-150 KHz per counter (scintillators along the planes, at positions which correspond to lower momentum, had a higher rate). The active area covered was $1400 \times 350 \text{ mm}^2$, which determined the number of bars. The number of segmented counters also determined the resolution of the hit position and of the momentum as obtained from the trajectories in the magnetic field. We allowed 1 mm gap between counters. The material used was EJ-204, which was cut and diamond milled by ELJEN Technology.

The light guides were $85 \times (24 \text{ to } 18) \times 6 \text{ mm}^3$ trapezian shaped light guides made from BC-800 material produced by BICRON. The scintillator (2 mm thick) was glued to a groove in the center of the light guide face. The light guides were glued to the PMT.

The expected magnetic field at the Auxiliary plane position was estimated to be roughly 0.02 T in the direction of the PMT axis. The design of the magnetic shield was based on soft iron cylinders of an external diameter 42 mm and an internal diameter of 23 mm. The shield extended more than two external radii beyond the photo cathode plane. We also used an inner μ -metal shield 0.8 mm thick, 95 mm long, with external diameter of 24.7 mm. 2-3 mm of the lower part of the iron cylinders were shaved off so to enable attaching them to a common plate. The plates were then mounted on the same platform, as shown in figure 2-9.

Magnet Auxiliary plane Trigger plane

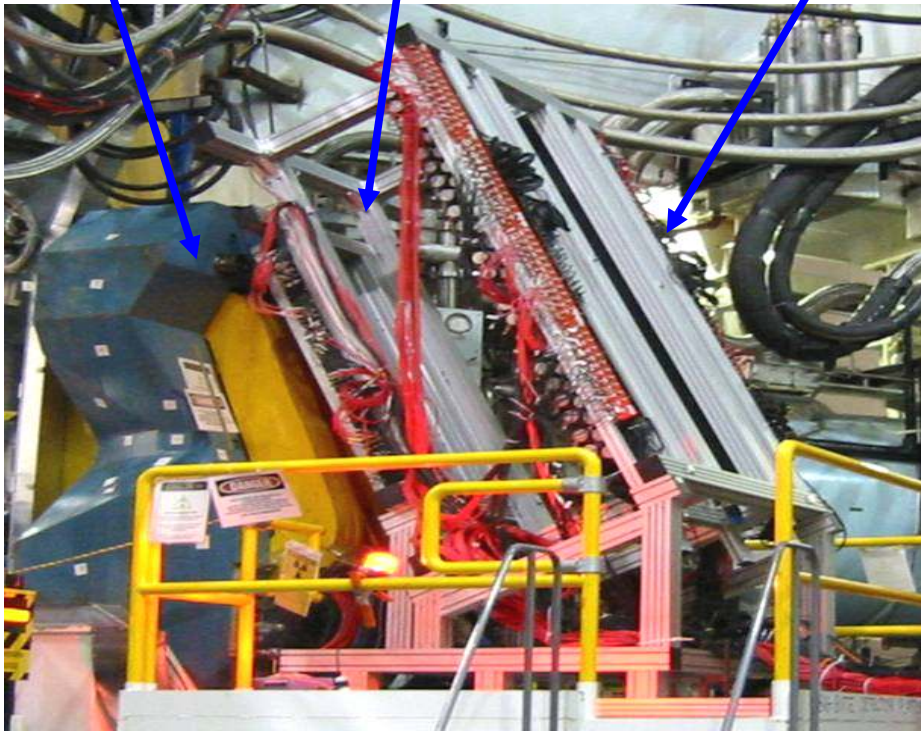


Figure 2-8: A photo of BigBite with the magnet (left) auxiliary (middle) and trigger (right) scintillator detector planes, as set in Hall A for the E01-015 experiment.

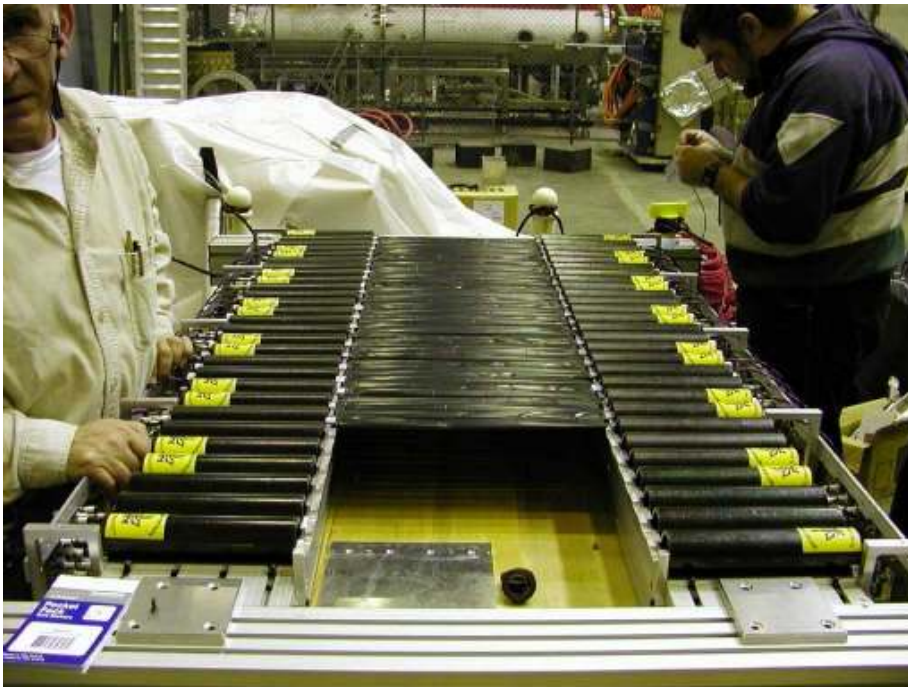


Figure 2-9: The auxiliary plane during assembly.

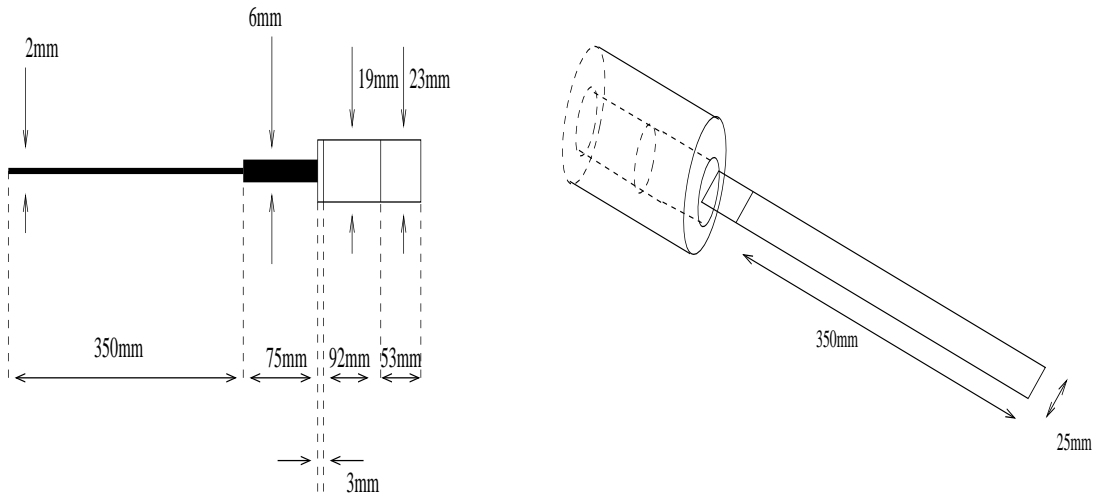


Figure 2-10: A schematic diagram of a single auxiliary plane counter, with the light guide, the PMT and the magnetic shield.

The Trigger Plane

The Trigger plane (see figures 2-11 and 2-12) consisted of two layers of segmented plastic scintillators. The first layer, called ΔE , consisted of 24, 3 mm thick scintillator bars. The second layer called E, consisted of 24, 30 mm thick bars. Each bar covered an area of $500 \times 86 \text{ mm}^2$ and was coupled to a PMT at each end.

The dominant considerations which determined the size/number of scintillators in the trigger plane were again the singles rates and the resolution. The expected singles rate was about 5-10 MHz for the full acceptance, which with a design of 24 counters, gave an average rate of about 200-400 KHz per counter. The active area we wished to cover was $2100 \times 500 \text{ mm}^2$, which determined the number of scintillators. Staggering the elements of each scintillator layer gave an expected position resolution in the dispersive direction of 43 mm (one half of a single counter width). The scintillators were made of EJ-204 material, which was cut and diamond milled by ELJEN Technology. Two $85 \times (24 \text{ to } 18) \times 6 \text{ mm}^3$ trapezian light guides were glued to each scintillator bar. The material which was used for making these light guides is BC-800 produced by BICRON. The scintillators (30 mm thick for the E bars and 3 mm thick for the ΔE bars) were glued to a groove in the center of the light guide face using Aljen optical cement. The light guides were glued to the PMT using a silicon elastomer.

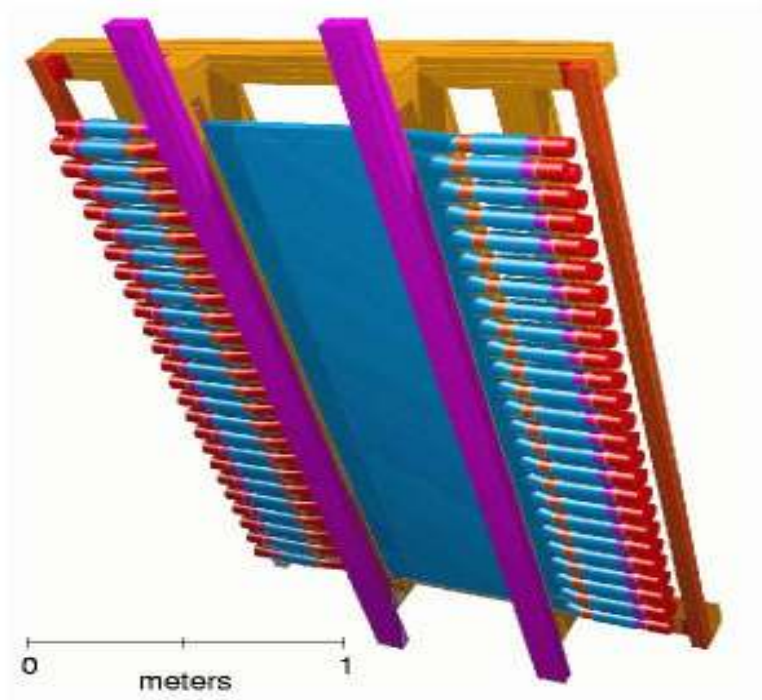


Figure 2-11: Schematic layout of the Trigger plane.

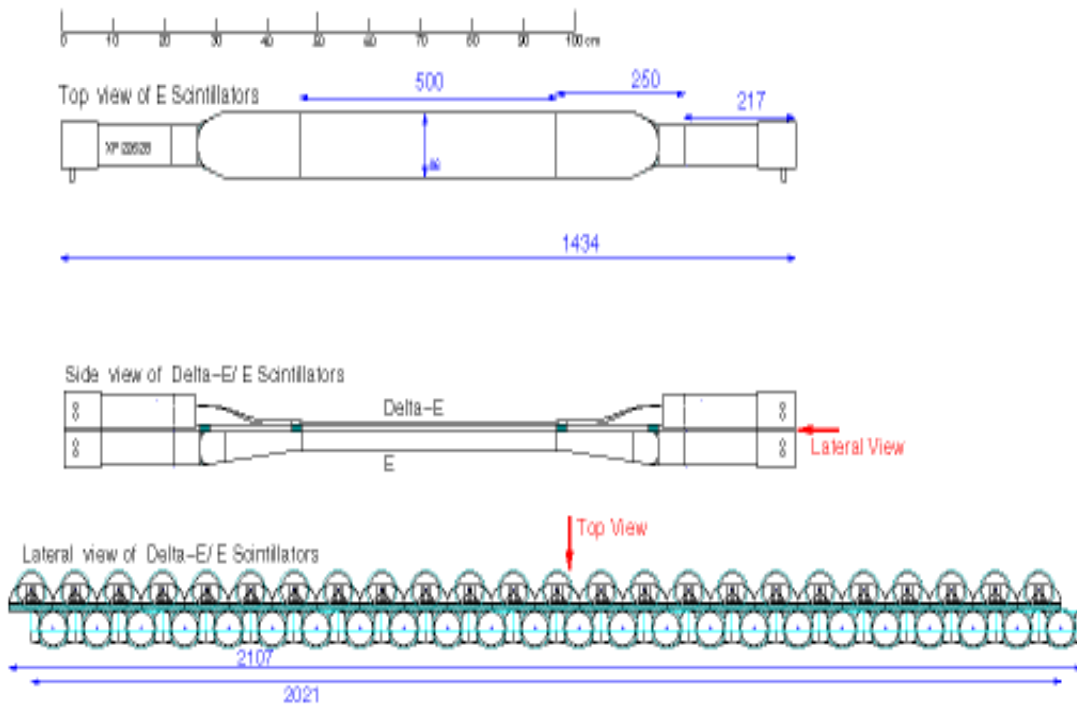


Figure 2-12: A side view of the Trigger plane.

2.3.2 BigBite characteristics and performance.

A complete set of tests and calibrations was performed both before and during experiment E01-015 in order to verify and tune every aspect of the spectrometer operation (more details are given in section 3.1).

Acceptance

Since BigBite uses a non-focusing magnetic dipole, there is no true upper limit on its momentum acceptance. The acceptance limit during the experiment was a result of both the geometry and the threshold of the discriminator used for the different scintillator detector signals processing. The overall momentum range in which BigBite operated during this experiment was 250-700 MeV/c (see section 3.1 for more details).

The vertical and horizontal acceptances of BigBite (although weakly depended on the momentum), were roughly ± 300 mrad (Vertical) and ± 80 mrad (Horizontal). This acceptance is the result of the geometry, the position of the magnet and the active surface covered by the trigger and the auxiliary scintillator planes (See figure 3-11).

Resolution

The two aspects that determine Big Bite's resolution are the timing resolution of the scintillator detectors and the number of scintillator elements in each of the scintillator planes. Performance tests showed that an angular resolution of 1.5° both in the vertical and horizontal axes was achieved. The timing resolution of the trigger plane scintillators were measured to be $\sigma = 0.5$ nsec. This timing resolution is translated to a momentum resolution of $\Delta p/p = 2.5\%$ (see chapter 3 for more details).

2.4 Electronics and Data Acquisition.

2.4.1 Trigger setup.

Triggers are electronic signals that prompt the data acquisition system to start readout of the detector information (see figure 2-13). In the E01-015 experiment setup only events in the HRSs formed the trigger, while BigBite was not part of the trigger. The main physics trigger types were: an electron spectrometer singles trigger (denoted "T3"), a hadron spectrometer singles trigger ("T1") and a coincidence between the HRS left and HRS right trigger ("T5"). For every T5 trigger, the HRSs, BigBite and the neutron array were read out.

The trigger system was built from commercial CAMC and NIM discriminators, delay units, logic units and memory units (MLU). First the signals from both PMTs in each paddle were required to form a coincidence for that paddle. The logical OR of the signals from these 6 paddles was then formed for that plane. The main trigger called S-Ray trigger, was formed from the logical AND of two scintillator plans with the requirement that the fired paddle combination in the two planes were in an allowed set. A memory lookup (MLU) was used to decide whether the combination was valid. The allowed combinations for S-Ray tracks were tracks at an approximately 45° angle with respect to the hall floor, with difference of fired paddle number in the two planes equal to 0 or 1. The timing of this trigger was determined by a strobe on the MLU which in most events comes from the right-side PMT of the second scintillator plane (S2).

The coincidence trigger T5 was formed in an overlap AND circuit with a 110 nsec window between the singles trigger T1 (from the hadron HRS) and T3 (from electron HRS). A looser trigger, T2, was formed if the S-Ray requirement could not be satisfied or only two of the 3 detectors fired: two scintillators and Cerenkov for the electron arm. For the hadron arm, the looser trigger T4 was formed if the S-Ray requirement could not be satisfied or if only one of the two scintillators was fired. The T2 and T4 triggers were mainly used for the measurements of the trigger inefficiencies. All these trigger types were sent to a scaler unit for counting and to a Trigger Supervisor (TS) unit which has both the pre-scaled function and MLU function. The prescale factor is an integer greater than 0. If the prescale for a specific trigger type was N, then only 1 out of N trigger of that type was recorded in the data stream. During the production data taking, all the other triggers except T5 were pre-scaled to reduce the dead-time of the DAQ computer system.

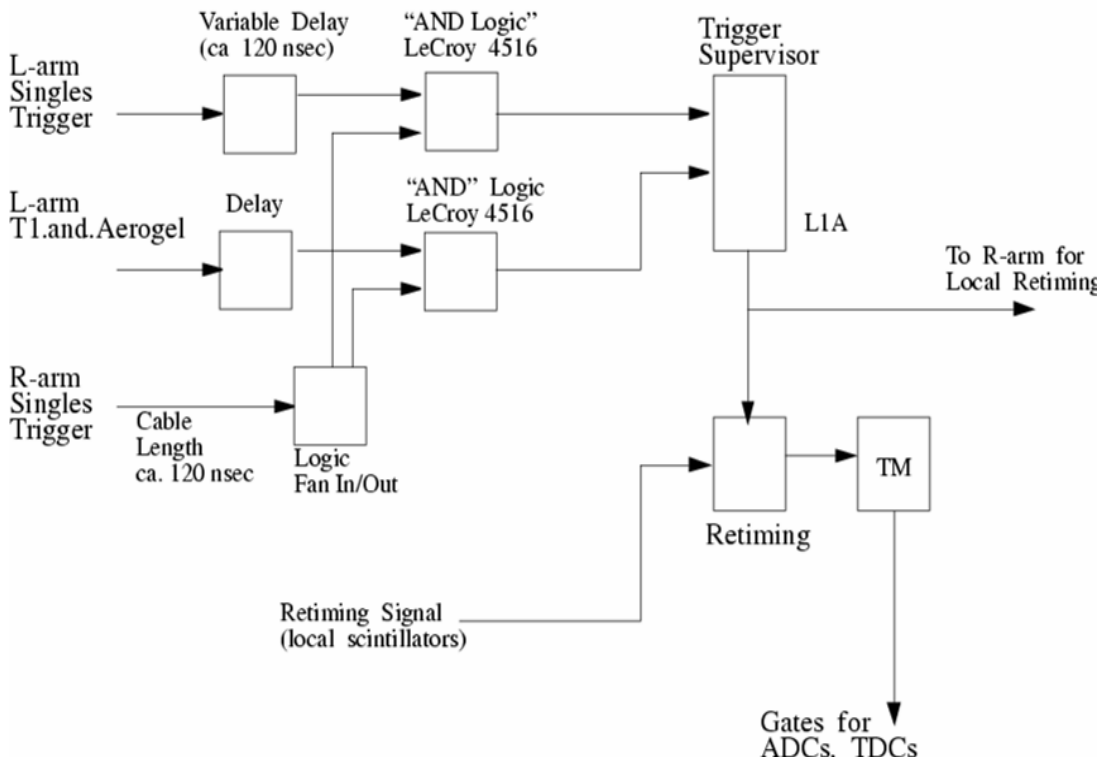


Figure 2-13: Circuit Diagrams of the trigger system.

2.4.2 Data Acquisition System.

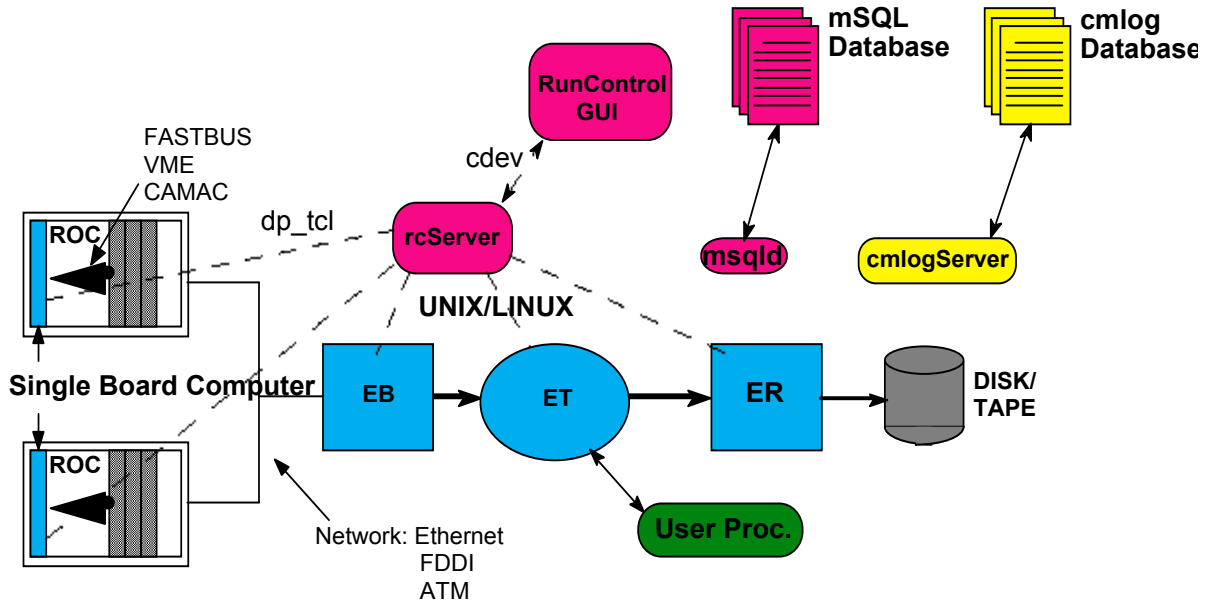
Figure 2-14 shows a block diagram of the Hall A data acquisition system (DAQ). The DAQ software was based on the "CEBAF online data acquisition" (CODA) package [49]. The hardware components were either custom made, such as the trigger supervisor module, or commercially acquired, such as the Analog to Digital Converter (ADC), Time-to-Digital Converter (TDC) and scaler modules. The E01-015 experiment used standard Hall A DAQ in two-spectrometer configuration [45] without readout of the focal plane polarimeter data. Additional DAQ system was assigned for the readout of the BigBite detector and the neutron array. The ADC, TDC and scaler modules were either Fastbus [50] or VME-type [51], and were housed in either a Fastbus or VME crates.

After registering hits from the detectors, the crates were read out by the Read Out Controllers (ROCs), which were CODA routines running under the VxWorks operating system [52]. The ROCs' function was to receive a trigger from the trigger supervisor, execute a corresponding readout list, structure the information and pass it over to the next CODA component, which is the Event Builder (EB). The Event Builder was a routine that waited for connection requests from the ROCs, collected their event fragments, ordered and merged the pieces in to a single data structure in CODA format. The events were then passed to the Event Recorder (ER), which was a CODA routine that wrote the events on disk. Written data files were eventually transferred to a central file-server.

2.4.3 Offline Analysis.

In both online and offline data analysis, the raw data acquired by the DAQ were analyzed by the ROOT/C++ analyzer for Hall A [53], which decodes and analyzes the data and writes out data summary and ROOT [54] files containing ntuples and histograms. The ROOT files were further analyzed using various ROOT scripts for the diagnosis of the detector status and extraction of physics results.

The ROOT/C++ analyzer for Hall A is general purpose analysis software written in C++. It was designed to analyze the data from the two Hall A High Resolution Spectrometers (HRS R and HRS L) with the standard detector packages. Experiment E01-015 was one of the first experiments to use the new C++ analyzer; therefore some custom code development was needed. Dedicated analysis modules were written into the analyzer program, in order to incorporate the new detectors used for the experiment (BigBite and neutron array).



- EB - Event Builder.
- ET - Event Transfer.
- ER - Event Reader.
- ROC - Read Out Controller.
- GUI - Graphical User Interface.

Figure 2-14 A block diagram of the Hall A data acquisition system (DAQ).

Chapter 3

Data Analysis

Offline data analysis was performed with the software package ROOT developed at CERN. ROOT is a C++ data handling program similar to PAW. Each event stored on tape by CODA [49], was unpacked into a ROOT tree format using the Hall A C++ analyzer. These data structures were related to basic elements of the detector such as the scintillator counters, drift chambers, etc. After the detector basic elements were read, more ROOT structures were created, such as particle tracks, reconstructed event information and various physical quantities. These results were visualized with ROOT to create various histograms and plots.

The data analysis of the $^{12}\text{C}(e,e'pp)$ reaction was divided into three major tasks:

1. Identify valid (e,e'p) events.
2. Identify a correlated proton in BigBite and determine its momentum.
3. Determine quantities of the correlated pair and global event analysis.

This subdivision was made with the purpose of a better understanding of the analysis techniques. Later in this chapter, the results of these processes are combined to extract the physical parameters of each event.

3.1 Particle Identification and momentum/angle measurements with BigBite.

3.1.1 ADC and TDC Calibrations.

The detectors were calibrated in the first phase of analysis. The procedure of calibration of ADC gains and pedestals is similar for the different scintillator detectors in the experiment, and is described below, using as an example the calibration of the Trigger plane E and DE counters in BigBite.

ADC Calibration

The ADC calibration of the trigger plane E and ΔE counters was performed by measuring the energy deposited by protons with exactly sufficient kinetic energy to "punch-through" the E counters (which is ~ 70 MeV kinetic energy or ~ 360 MeV/c momentums). The calibration was then done for each overlapping E and ΔE counters pairs sequentially. The gain and pedestal offset parameters were adjusted to match the "punch-through" point of every E and ΔE counter to be at the same channel (channel 2500 for the E counters and channel 1500 for the ΔE counters). Figure 3-1 shows the pulse height in the ΔE plane vs. the pulse height in the E plane in ADC channels.

TDC Calibration

The timing offset of each TDC channel of the trigger counters was set. This was done by two methods:

- A. Setting a known TOF/meter for all the counters at a predetermined value (this procedure requires the information about the location of each detector).
- B. Calibrating the counters sequentially, using particles (cosmic rays/protons) that hit both an E and a ΔE counter simultaneously, each step calibrating two overlapping E and ΔE counters. In this method the calibration was done by progressing through pairs of E to ΔE starting at the top of the plane and moving down.

3.1.2 Use of ep Elastic data for calibration and tuning.

Elastic H(e,e'p) calibration data was used to calibrate various aspects of the BigBite spectrometer optics. The over-determined 2 body kinematics allowed us to obtain the kinematics of proton scattered into BigBite using the coincident scattered electron in the HRS. The elastically scattered protons have momentum magnitude and direction equal to \vec{q} , the momentum transferred by the scattered electron. Energy losses of the proton inside the target and during the flight path were estimated and corrected for.

3.1.3 Momentum reconstruction.

We developed several ways to determine the momentum of the in-coming particle in BigBite. The different methods can be divided in to 3 groups –

1. Time Of Flight (TOF) based methods (TDC info).
(Auxiliary plane to the E plane, target to the E plane)
2. Energy-Deposit based methods (ADC info).
(E and ΔE , ΔE alone, Auxiliary alone)
3. Curvature in the magnetic field methods.
(fit based, analytical calculation based)

Each of these techniques (7 options in all) has a different resolution and efficiency which will be discussed below. Each has advantages and disadvantages in different parts of the entire momentum acceptance of BigBite.

Time Of Flight (TOF) based methods (TDC).

These methods involve measuring the time of flight of the particle for a known distance. The two intervals used for these methods are: from the target to the E plane and from the Auxiliary plane to the E-plane. In order to calculate the momentum of a particle with a known mass, 3 quantities are required – The time in the origin, the time in the destination and the path length.

Target to the E plane.

This method yielded the best resolution for momentum determination using BigBite. ($\sigma \cong 10$ MeV/c for protons of 250 - 400 MeV/c).

Time-in-origin - This is the time when the particle left the target (the interaction time). Since this time is not measured directly, it was obtained using the time of the electron arm (HRS) corrected for the different path lengths of different electrons. This time had a resolution of the order of $\sigma \cong 0.4$ nsec.

Time in the E plane- This time was obtained by averaging the left and the right PMTs times in the E plane. The times of the different paddles were aligned relative to each other, to create a combined peak with a width of 0.3 nsec. This alignment was performed by looking at events which had coincidence hits in an overlapping E and ΔE counters. This procedure was repeated for all the ΔE -E pairs, along the entire trigger plane. Then the common zero time was calibrated relative to the time-in-origin, discussed above.

Path length- The total path length from the target to the E plane was calculated per event. The path can be divided in to 3 parts (from the target to BigBite, inside BigBite magnetic field (depended on the momentum) and from BigBite magnetic field exit to the E plane). The path calculation has a resolution of the order of few a cm (see appendix A).

Auxiliary plane to the E plane.

This method has a resolution of $\sigma \cong 40$ MeV/c for protons of 250-400 MeV/c. The main reasons for this relatively poor resolution are the smaller flight distance and the use of a single PMT per Auxiliary plane bar.

Time-in-origin - This is the time when the particle had hit the Auxiliary plane. A correction was applied to this time in order to account for the propagation time of the light from the hit point to the PMT (~ 1 nanosec). This correction was done by calculating the hit position along the Auxiliary paddle, and computing the distance traveled to the PM. The hit position on the Auxiliary paddle was determined by extrapolating from the hit position on the E plane. The light propagation speed was previously measured and the different Auxiliary paddles were aligned relative to each other.

Time in the E plane- As in the previous method, this time was obtained by averaging the left and the right paddles times in the E plane, which were first calibrated relative to each other.

Path length- The total path length from the auxiliary hit point to the E plane was calculated per-event. The hit point on the auxiliary plane was calculated using the hit position on the E plane assuming a point target. This path calculation has a resolution of the order of 2 cm.

Both methods described above, based on TOF measurements, have resolution which decreases as the momentum of the proton increases (See Figure 3-2).

Energy deposit based methods (ADC).

These methods are based on the correlation between the momentum of a particle and the energy deposited over a fixed length inside a scintillator material. Each scintillator bar in each of the three planes (E, ΔE and Auxiliary) were first calibrated to have the same gain, by adjusting the "punch-through" point for protons to be in the same channels (see section 3.1.1).

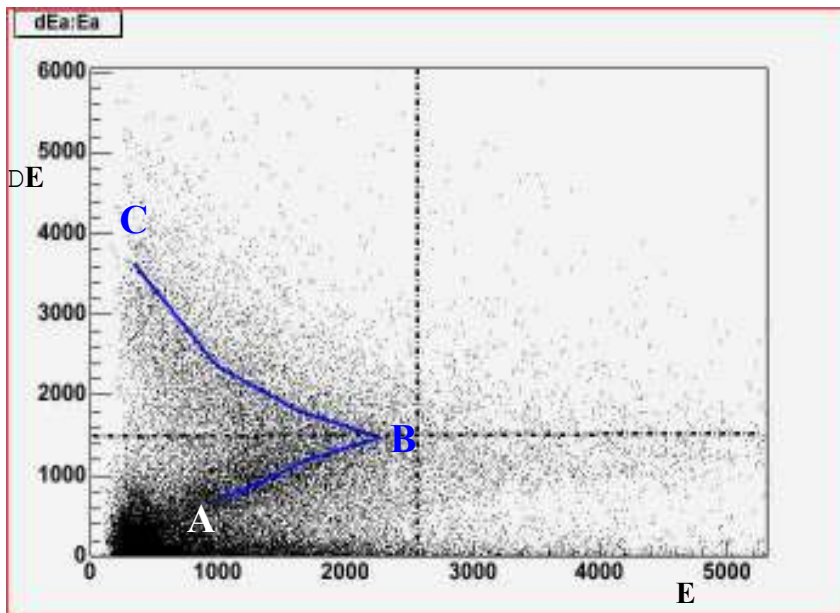


Figure 3-1: Pulse height in the ΔE plane vs. pulse height in the E plane in ADC channels. The dotted line represents the "punch-through" point (B), while the solid line represent protons with increasing momentum from top (C) to bottom (A). This plot which includes all the counters in the E and ΔE planes was produced after first matching the gain of the different paddles inside the E and ΔE planes.

E and ΔE energy deposit– This method has a resolution of about $\sigma = 20$ MeV/c (for protons of 250-400 MeV/c). The energy deposit in the ΔE plane counters was used to determine if the particle has a kinetic energy above or below the "punch through" point (AB or BC in figure 3-1). The momentum itself was determined using the geometrical sum of the left and the right PMT energy deposited in the E plane scintillator (see figure 3-1). The momentum was then determined using an exponential fit to the known momentum of protons detected in coincidence with electron in the H(e,e'p) scattering process.

ΔE energy deposit– This method has a resolution of about $\sigma = 45$ MeV/c (for protons of 250-400 MeV/c). In this method the energy deposit in the ΔE scintillator was used to calculate the momentum. The momentum was determined using a fit to the known momentum of protons detected in coincidence with electron in the H(e,e'p) scattering process.

Auxiliary plane energy deposit- This method has a resolution of about $\sigma = 60$ MeV/c (for protons of 250-400 MeV/c). In this method the energy deposit in the Auxiliary plane scintillator was used to calculate the momentum. The momentum was determined using a fit to the known momentum of protons detected in coincidence with electron in the H(e,e'p) scattering process. A correction was applied for attenuation from different path length, traveled inside the detectors. This path was calculated based on the hit position in the E plane.

Momentum calculated from the curvature inside the magnetic field.

A non-focusing magnetic dipole ($B \sim 0.93$ T) was used to curve the charged particle paths before they hit the detector planes. The radius of curvature of the particle path in the magnetic field is proportional to its momentum (see Eq. 2-1). Both hit position based methods which are described below (same as for the TOF based methods) become less accurate in determination of the momentum as the momentum of the proton increases and the curvature decreases to an almost straight line.

Analytical calculation based reconstruction- This method has a resolution of about $\sigma = 30$ MeV/c (for protons of 250-400 MeV/c). To calculate the three-dimensional position of a detected particle, we use the known positions of the bars that were hit and the time differences between the signals in the left and right PMTs of those bars. The hit pattern information of each scintillator plane, assuming a point-like target, can be used to reconstruct the particle path inside the magnetic field and the corresponding magnitude and direction of the particle's momentum (see Appendix A).

Fit Based reconstruction- This method has a resolution of about $\sigma = 25$ MeV/c (for protons of 250-400 MeV/c). The Fit to the momentum was done using the outgoing proton incline (i.e. the vertical hit position on E – vertical hit position on Auxiliary). Due to the fact that this fit does not depend on any geometric or physical parameter, it gives a slightly better resolution than the actual analytical calculation (see above)

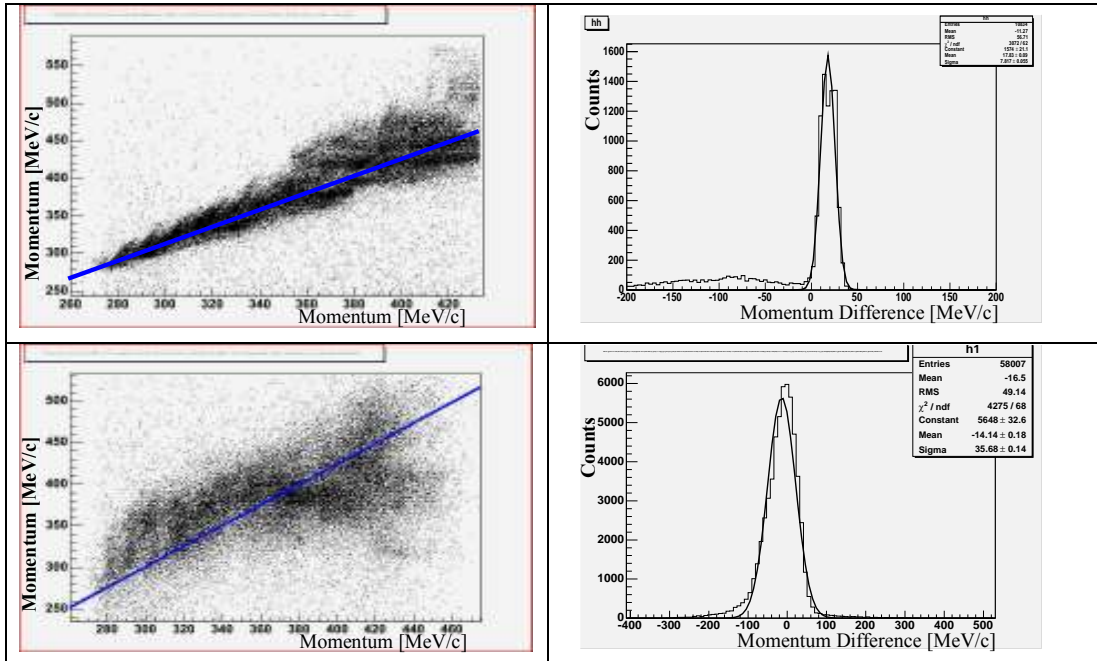


Figure 3-2: Reconstructed momentum using TOF vs proton momentum deduced from the H(e,e'p) reaction using the electron in the HRS (Left). The difference of the two reconstructed momenta (Right). Momentum reconstruction using TOF between the target and the E plane (Top). Using TOF between the Auxiliary plane and the E-plane (Bottom).

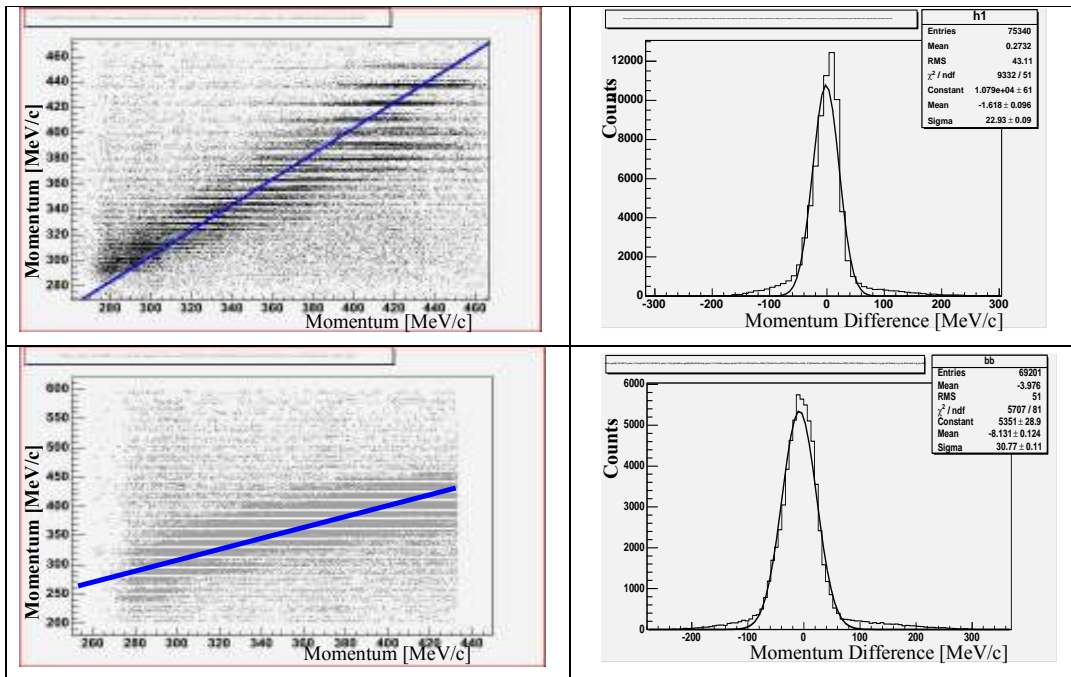


Figure 3-3: Reconstructed momentum using analytical calculation of the radius of curvature inside the magnetic field vs proton momentum deduced from the over-determined H(e,e'p) reaction (Top). Fit based reconstructed momentum using hit-position, vs proton momentum deduced from the over-determined H(e,e'p) reaction (Bottom).

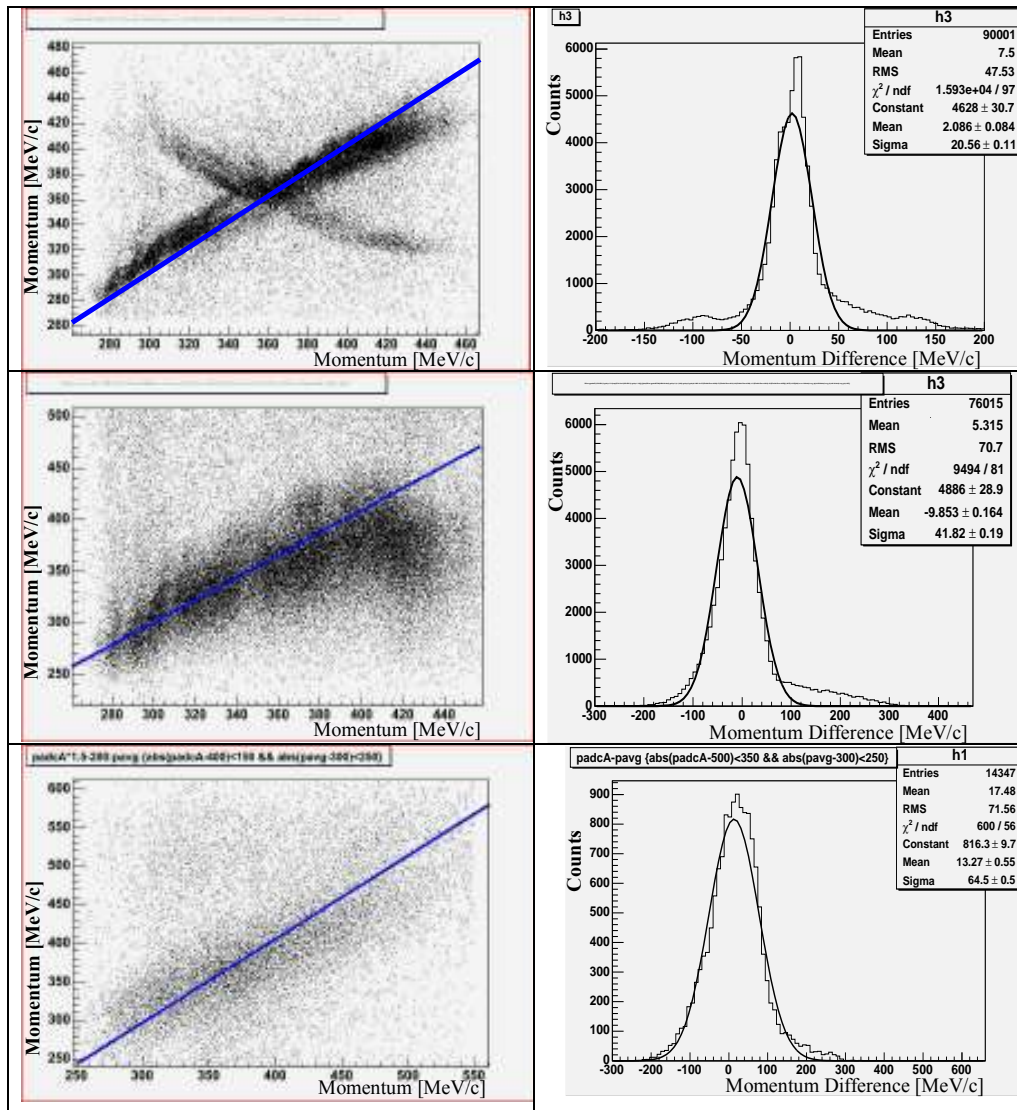


Figure 3-4: Reconstructed momentum using energy deposit vs. proton deduced from the over-determined H(e,e'p) reaction (Left). The difference of the two reconstructed momenta (Right). From top to bottom- Reconstructed momentum using energy deposit in the E plane (Top), using energy deposit in the DE plane (Middle), and using energy deposit in the auxiliary plane (Bottom).

3.1.4 Reconstruction of scattering angles.

Reconstruction calibration of the direction of the incoming particle in to BigBite (in-plane and out-of-plane angles, which correspond to vertical and horizontal) was performed using elastic $H(e,e'p)$ scattering data.

Out-Of-Plane angle of the particle

Here we refer to the reconstruction of the out-of-plane (vertical) angle. This is the same direction in which the magnetic field bends the protons. The reconstruction in this method has a resolution of about 1.5° (see figure 3-6). The reconstruction of this angle is folded together with the momentum calculation from the curvature. The hit pattern information of each scintillator plane can be used to reconstruct the particle path inside the magnetic field and the corresponding direction of the particle's momentum (see appendix A).

In-Plane angle of the particle

Here we refer to the reconstruction of the in-plane (horizontal) angle. The reconstruction in this method has a resolution of about 1.5° (see figure 3-7). This reconstruction is based on measuring the time difference between the left and the right PMT's of the hit paddle of the E plane. The detectors were first calibrated and centered, so that the corrected distribution for a uniform hits along the detectors, gives a "step-function" between ± 25 cm, which is the physical dimension of the detectors. After calculating the hit-point along the detector x, the first-order calculation of the in-plane angle, is given simply by:

$$\theta = \arctan(x/z),$$

where z is the distance between the counter that was hit and the target.

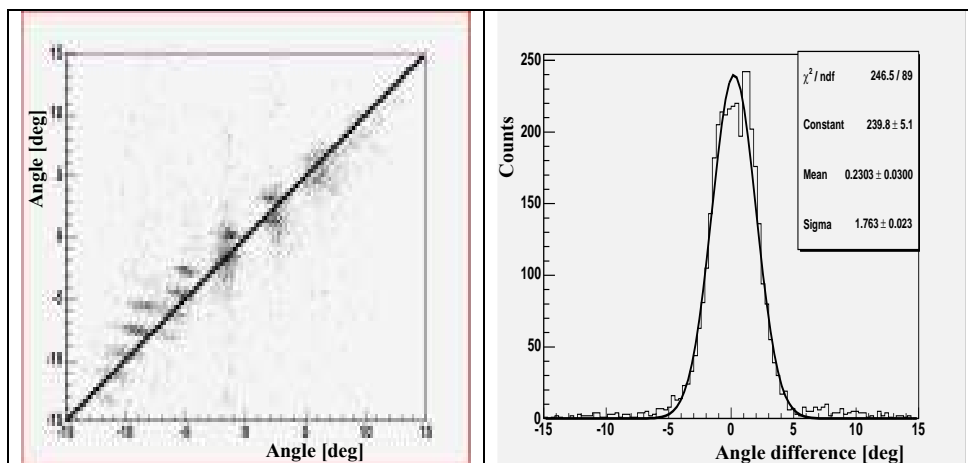


Figure 3-6: The out of plane angle reconstructed in BigBite [deg] vs. the out-of-plane angle of the proton as determined from the electron [deg] (Left). The difference between the out-of-plane angle as measured in BigBite and the expected angle from the electron as measured by the HRS with a typical resolution of $\sigma=1.5^\circ$ (Right).

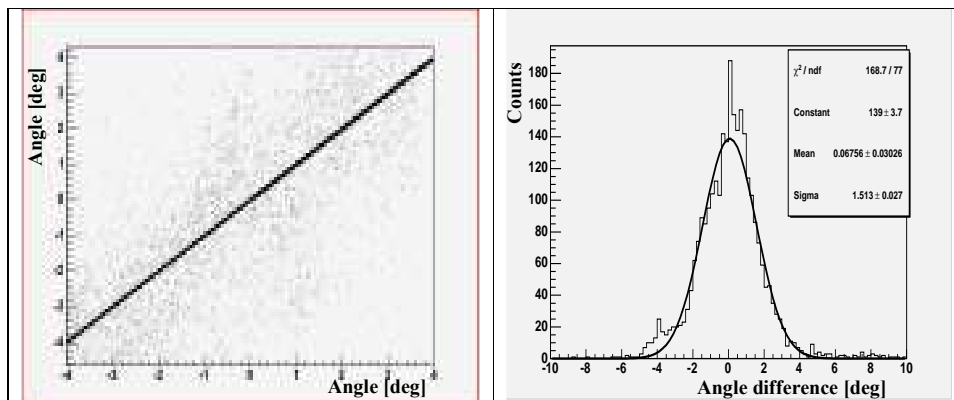


Figure 3-5: The in-plane angle reconstructed in BigBite [deg] vs. the in-plane angle of the proton [deg] as determined from the electron in H(e,e'p) (Left). The difference between the in-plane angle as measured in BigBite and the expected angle from the electron as measured by the HRS (Right).

3.1.5. Particle Identification.

The most important method for particle identification in BigBite is based on the energy deposited in the E and ΔE counters. Having different thickness (3 cm for the E and 3 mm for the ΔE counters) the E- ΔE detectors are used to differentiate between different possible particles which are expected in these kinematics conditions; Protons, Pions, Kaons, Photons, Deuterons etc... Each of these particles has a typical energy deposit pattern, which was identified and tagged (See figure 3-7).

Another technique which is applicable is by establishing different matching criteria between the different results from the momentum reconstruction (see above). Negatively charged particles will have a "negative" curvature inside the magnetic field, which will result in a reconstructed momentum with negative values. Pions Electron and Photons, which are all relativistic in this kinematics, have a short and unique TOF which can be cut-out to filter only protons and heavier (non-relativistic) particles. Deuterons & heavier particles can be cut out by comparing momentum measured by radius in magnetic field, and TOF of particle.

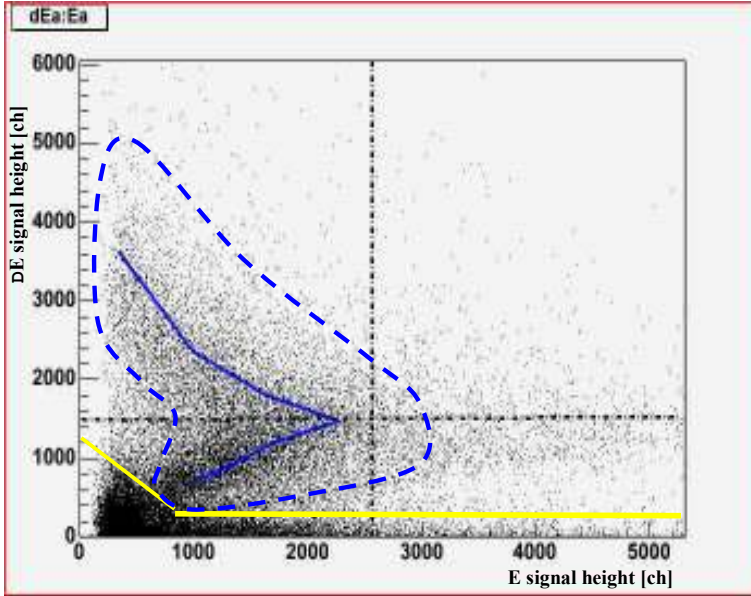


Figure 3-7: The pulse height in the ΔE plane vs. the pulse height in the E plane in ADC channels. The lower solid lines represent a low energy deposit areas cut, which are typical to photons and pions. Further PID cuts included a "sleeve" cut, which follows the proton's curve. Deuterium and heavier particles are located in a higher E and ΔE energy deposit.

3.1.6 Definition of Track and Selection of the Golden Track.

A track was defined for every possible combination of overlapping E, ΔE and Auxiliary bars which were hit. The relatively high singles rates created a few tracks per event (see figure 3-8). In order to reduce the number of tracks, a set of preliminary cuts was applied. These cuts consisted of energy deposit cut, to eliminate minimum ionizing particles, and a hit pattern cut, which removed neutral and negatively-charged particles (see section 3.2.2). Since multiple tracks were still reconstructed for part of the events in BigBite, it was necessary to create a stricter selection mechanism.

A hit in these detectors was defined in cases where the pulse was enough to trigger the discriminator in both the left and the right PMTs for the E and the ΔE planes, and a single PMT in the Auxiliary plane. After all the different possible tracks were assigned for each event, we calculated the momentum for all possible tracks, using all the various methods. For each track the relative mismatch ("score") was defined in the following way –

$$\text{Score} = \sqrt{\frac{\sum_i (P_i - P_{avg})^2 / \sigma^2(p_i)}{n - 1}} / P_{avg} \quad \text{Eq. 3-1}$$

Where P_i are the different momenta calculated for this track, P_{avg} is the average momenta, $\sigma(p_i)$ is the relative resolution of technique i , and n is the total number of techniques (=6). The track which had the lowest overall difference between the different momentum calculated, is the one which was identified as the golden track.

Note: The only method which does not enter the score calculation is the target to E TOF momentum calculation method. This is in order to prevent biasing of this quantity, as it is the main momentum calculation method, and has the best resolution.

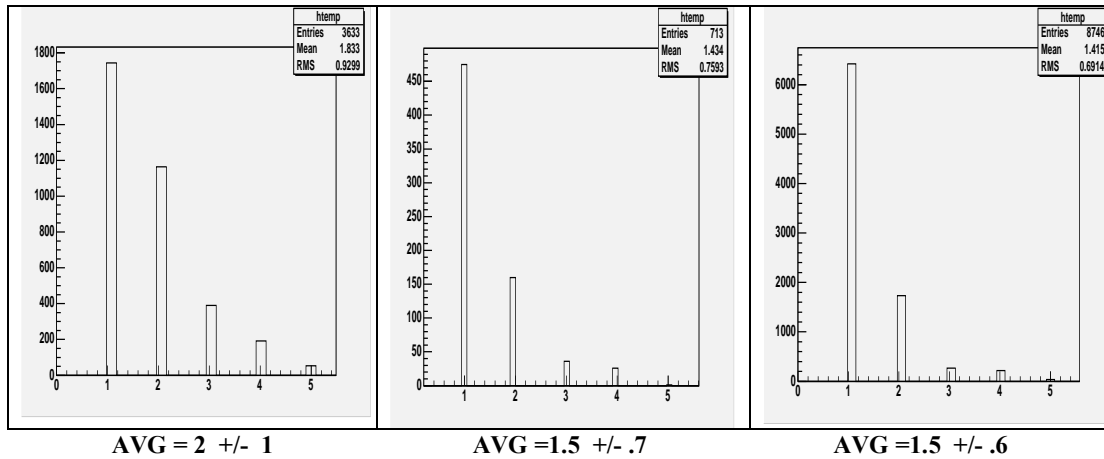


Figure 3-8- Distribution of the number of reconstructed tracks from different data sets. Elastic data set (highest luminosity) [Left]. Number of tracks distribution for 30 μ A beam current data [Center]. Number of tracks for 5 μ A beam current (lowest luminosity) [right]. The number of tracks in the different distributions increases with the luminosity. Notice that the tracks are only those reconstructed for valid protons tracks as identified by the $E \Delta E$ energy deposit, and bar hit positions.

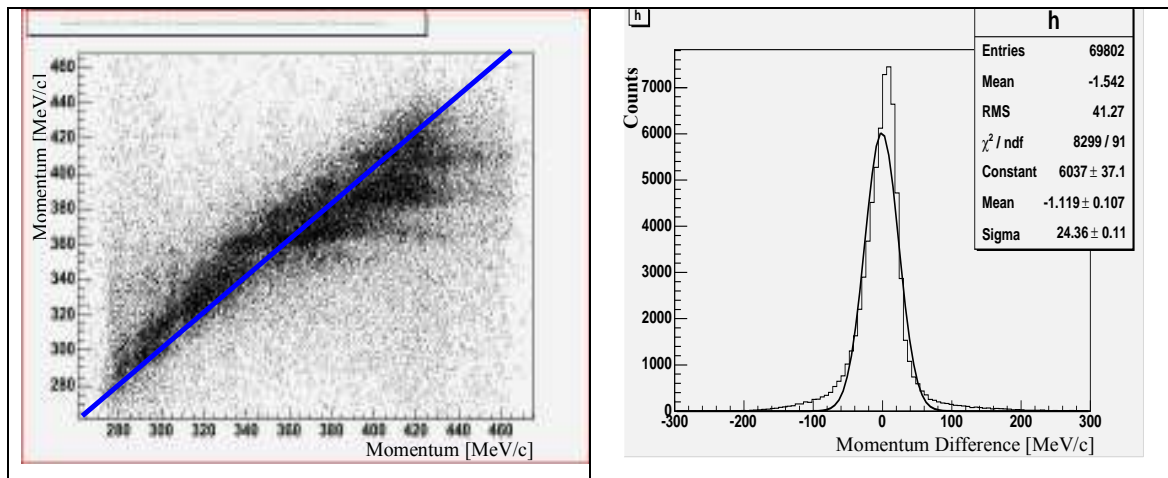


Figure 3-9: The average proton momentum vs. the proton momentum reconstructed from the electron HRS (Left). The difference of the two reconstructed momenta, with a $\sigma = 25$ MeV/c (Right).

The average reconstructed momentum from all the methods vs. the proton momentum from the H(e,e'p) calibration can be seen in figure 3-9. Further noise-reduction mechanism was applied by limiting the golden-track relative mismatch (see Eq. 3-1 for the calculation of this quantity). We estimated the number of legitimate events which might be removed together with the noise when applying such a cut, using a Monte Carlo simulation.

In the simulation a "real" momentum in the same kinematical conditions as the elastic data was randomly generated (Gaussian distribution with mean=400 MeV/c and $\sigma=120$ MeV/c). Next, the "reconstructed" momenta were generated for each technique, each with its own σ around the original momentum. The relative mismatch quantity was calculated for each of the events. The over all distribution can be seen in figure 3-10 right. Cutting out all events with score>2 resulted a loss of less then 1% of legitimate events (these maybe real events which are cut out).

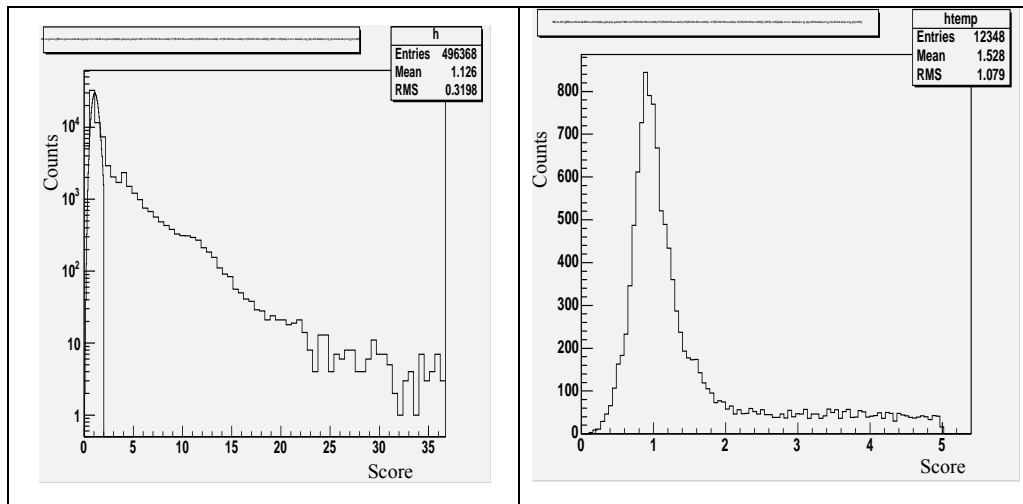


Figure 3-10: Left: The score calculated for the Elastic data events viewed on a log scale. The narrow peak represents simulated results with no accidentals. Right: a zoom in of the score distribution calculated for the elastics data events. Applying a score< 2 cut to the simulated distribution, resulted with about 1 percent event loss. A similar cut on the data removes about 30 % of the total events.

3.1.7 Efficiencies.

Big Bite's overall efficiency was determined in two ways:

- Comparing the number of elastically scattered protons detected in BigBite, with the totals number of elastically scattered H(e,e'p) events (as determined by the number of detected electrons in the HRS).
- Determining the individual detection efficiencies of each detector plane (the auxiliary plane, the ΔE plane and the E plane), and then calculating the overall BigBite spectrometer efficiency.

The efficiency determined by the two methods agreed to be 84%. The overall detection efficiency is set mainly by the efficiency of the plane which has lowest individual detection efficiency. In BigBite case, the auxiliary plane has a detection efficiency of 85 % while the ΔE and the E has a detection efficiency of about 99%). The detection efficiency is a function of the energy deposited by the protons in BigBite, the gain, and the threshold level that was set in the discriminators.

As a result of BigBite geometry, and the fact that the curvature of the protons in BigBite depends on their momentum, the efficiency of BigBite is a function of the angle and the momentum of the incoming proton. Figure 3-11 shows a scatter plot of proton's angle vs. momenta, where the lower efficiency can be seen at lower momenta.

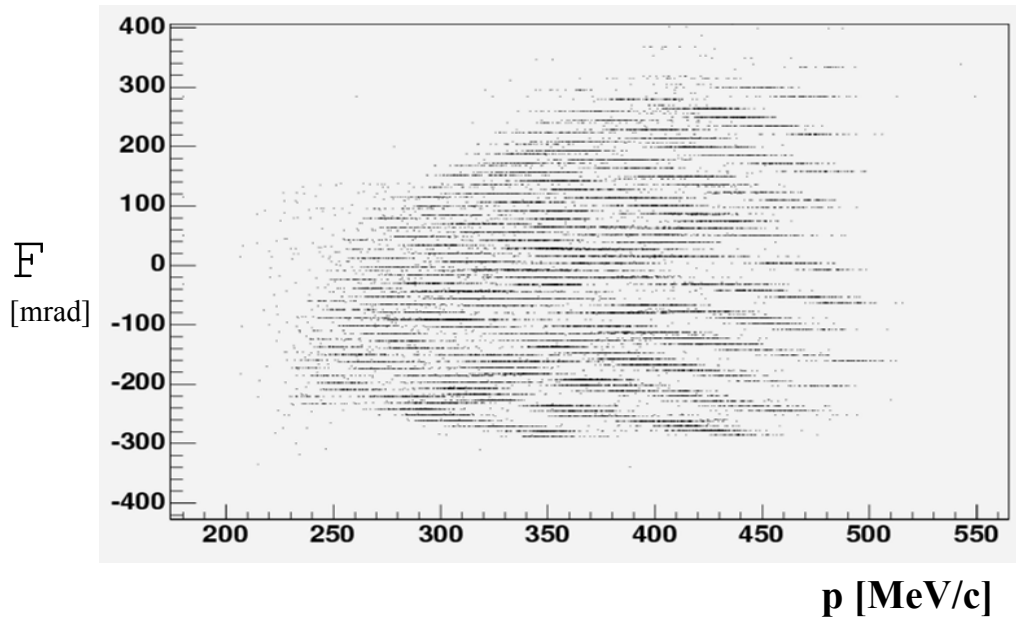


Figure 3-11: A Scatter plot of the out-of-plane vertical angle [mrad] vs the proton momentum [MeV/c] for proton singles. The angular acceptance of BigBite is limited at momenta lower then < 350 MeV/c.

3.2 Cuts and selection of events.

3.2.1 The $^{12}\text{C}(e,e'p)$ reaction.

We combined the beam, electron and proton analysis to select a final set of events corresponding to the $^{12}\text{C}(e,e'p)$ reaction. The event selection-cuts were carefully designed to suppress accidental and background level. These cuts inevitably excluded some events which are from the reaction of interest.

HRS nominal acceptance cuts and reconstructed track multiplicity cuts.

Acceptance cuts were used to match the HRS known acceptance by selecting only events which had reconstructed quantities that fall within the spectrometer acceptances. Cuts were applied on the reconstructed in-plane angle (± 28 mrad), out-of-plane angle (± 60 mrad) and momentum (± 4.5 %) of the particle detected in the HRS. An additional cut was applied to reject events with high multiplicity, as track reconstruction is unreliable for high multiplicity events.

Coincidence-time cut.

The coincidence time (see figure 3-12) is defined as the relative time between the triggers coming from the left and the right HRSs. The coincidence signal width was about $\sigma \cong 0.4$ ns. The time window applied was 2 ns wide.

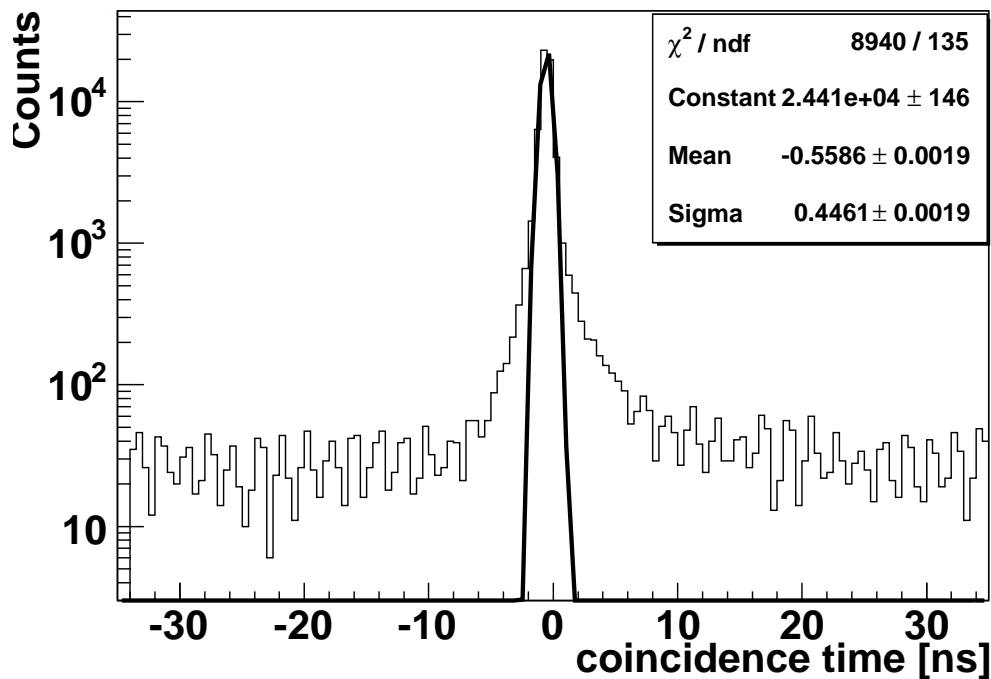


Figure 3-12: The coincidence time between the two HRSs, with a width $\sigma=0.4$ ns. The beam structure can be seen with a pulse interval of 2 ns.

Missing-energy cut.

The missing energy in the (e,e'p) reaction is defined as the difference between the total energy of the outgoing particles and the total energy of the incoming beam:

$$E_{miss} = E_{in} - E_{out} = E_{beam} - E_{e'} - T_p - T_{A-1} \quad \text{Eq. 3-2}$$

where T_p is the kinetic energy of the knocked out proton and T_{A-1} is the kinetic energy of the residual nucleus. E_{miss} is the energy which was available for breaking up of the nucleus. The kinematical region in which we are interested is where there is at least enough energy to remove two protons from the carbon nucleus. The minimal energy needed for such a break-up is when two protons are removed from the carbon p-shell. The energy needed in this case is $2 \times 16 \text{ MeV} = 32 \text{ MeV}$ which defined our lower boundary of the missing energy cut. At high missing energy, process such as pion and delta productions start to play a more dominant role. The study of these reactions is outside the scope of this work, hence a $E_{miss} < 240 \text{ MeV}$ cut was applied.

Δ production cuts.

Additional cuts were applied in order to further remove pion and delta production events (see figure 3-13). This was done by either cutting on the in-plane angle of the \vec{p}_{miss} Vector to be above 77° , 84° and 88° for kinematics settings of $p_{miss} = 300, 400$ and $500 \text{ MeV}/c$ respectively, or by applying a $x_B > 1$ cut (see discussing in chapter 4).

3.2.2 The $^{12}\text{C}(e,e'pp)$ reaction.

The cuts applied to select $^{12}\text{C}(e,e'pp)$ are all the cuts used to select $^{12}\text{C}(e,e'p)$ and additional cuts involving BigBite variables, as listed below.

Initial cuts

In order to reduce the number of tracks a set of preliminary cuts was applied. These cuts included an energy deposit cut to eliminate minimum ionizing particles (see figure 3-7) and a hit pattern cut, which removed neutral and negatively charged particles (see figure 3-15).

Time-of-Flight

The (e,e'pp) events were selected by applying a cut to the corrected TOF of the protons from the target to the E-plane (see section 4.2). The measured TOF was corrected by subtracting the TOF using momentum determined by other methods (see section 3.1) over a path length calculated using the counter numbers which were hit (see Appendix A). The corrected TOF spectra can be seen in the figure 4-6. The nominal cut applied was 14 ns wide.

Particle Identification (PID)

A cut for selecting protons was applied on the energy deposit of the particle in the E and ΔE counters (see section 3.1.5 and figure 3-7). PID was also applied by cutting on the "score" which represents the relative agreement between different methods used for determining the proton momentum (see section 3.1.6). The 'score' values decreases as the agreement between different techniques improves. In the case where the detected particle is not a proton, the different methods yield different values, and the score is high.

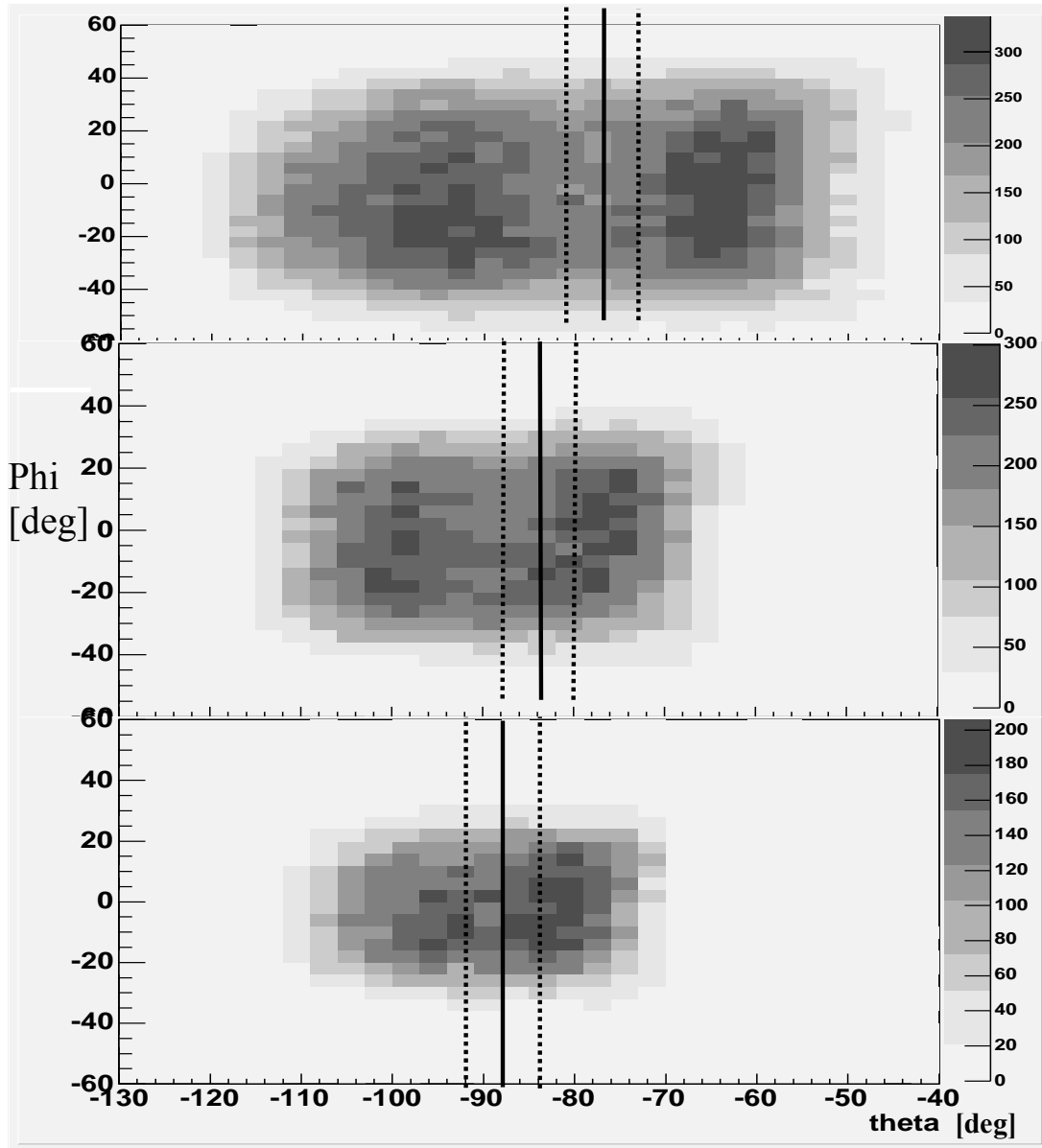


Figure 3-13: The out-of-plane angle vs. the in-plane angle of \vec{p}_{miss} for kinematics K1 (top), K2 (middle) and K3 (bottom). The solid line in each plot represents the nominal cut which was applied to remove pion and delta production events. The dotted lines represent $\pm 4^\circ$ cuts which were used for sensitivity checks.

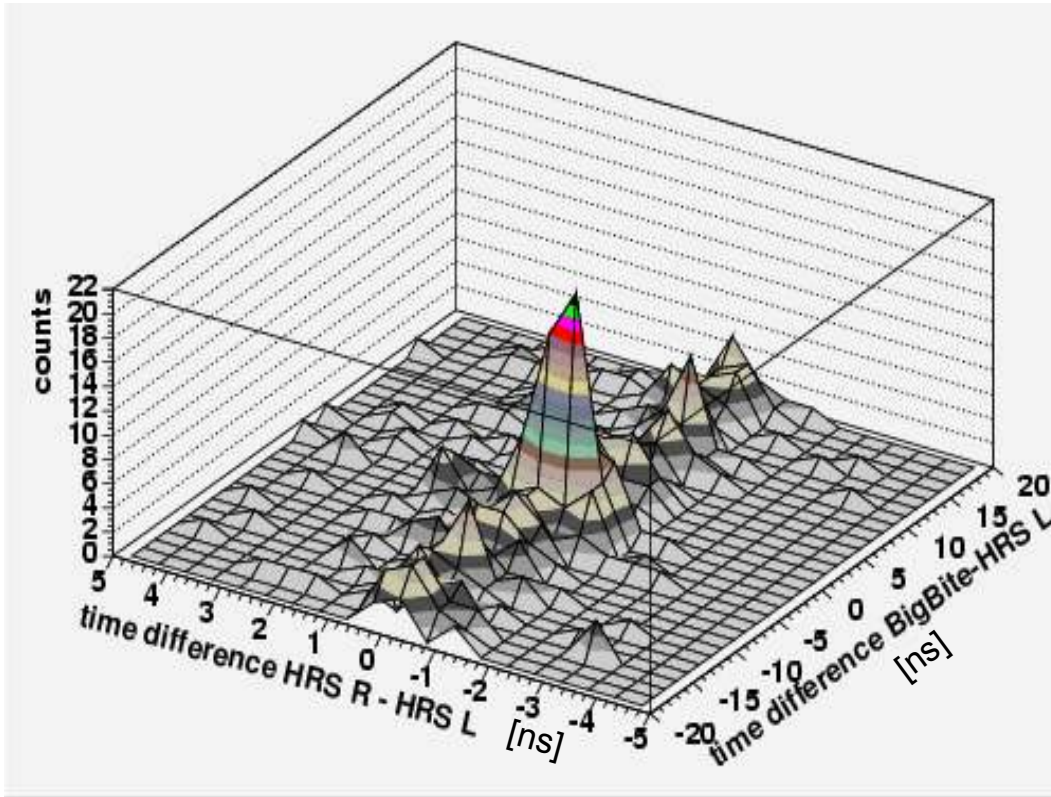


Figure 3-14: Number of counts vs. the time difference between the two HRSs and the time difference between BigBite E-plane and HRS-L.

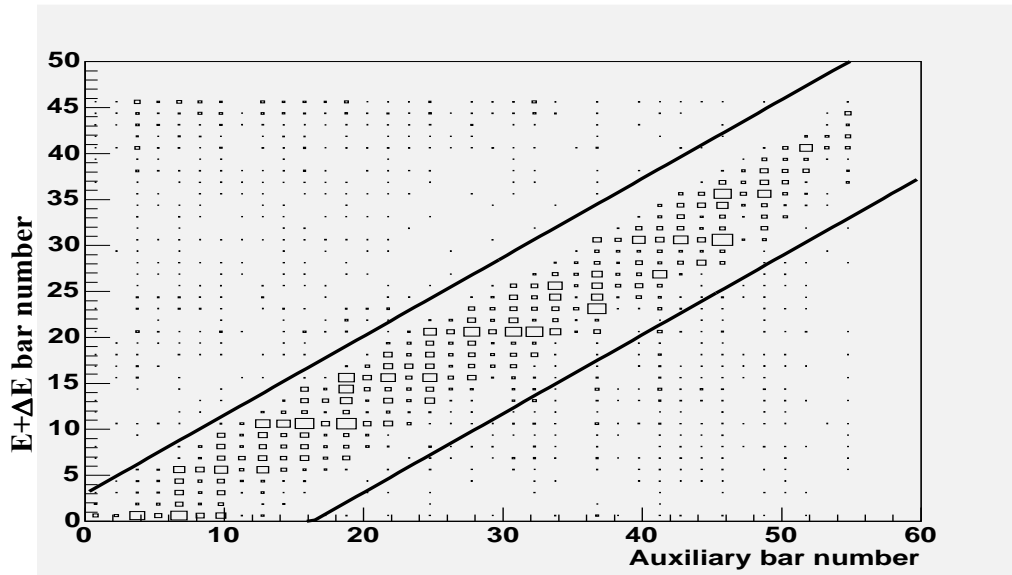


Figure 3-15: The distribution of the hit bar number in BigBite Trigger plane ($E+\Delta E$) vs. the Auxiliary plane bar number. The area between the two diagonal lines was selected in order to remove neutral and negatively charged particles tracks.

Chapter 4

Results and Conclusions.

4.1 The semi inclusive $^{12}\text{C}(e,e'p)$ reaction for $X_B > 1$.

The two Hall A high-resolution spectrometers (HRSs) [45] were used to measure the $^{12}\text{C}(e,e'p)$ reaction. Scattered electrons were detected in the left HRS (HRS-L) and knocked-out protons were detected using the right HRS (HRS-R).

For the $^{12}\text{C}(e,e'p)$ reaction the energy and momentum transfer, ω , \vec{q} are defined in the following way :

$$\omega = E_e - E_{e'} \quad (\text{Eq. 4-1})$$

$$\vec{q} = \vec{p}_e - \vec{p}_{e'} \quad (\text{Eq. 4-2})$$

Where E_e and \vec{p}_e are the energy and momentum of the incident electron, and $E_{e'}$ and $\vec{p}_{e'}$ are the energy and momentum of the scattered electron.

The missing energy and missing momentum of the $^{12}\text{C}(e,e'p)$ reaction are defined in Eq. 4-3 and 4-4.

$$\vec{p}_{miss} = \vec{q} - \vec{p}_{HRS} \quad (\text{Eq. 4-3})$$

$$E_{miss} = E_e - E_{e'} - T_{HRS} - T_{A-1} \quad (\text{Eq. 4-4})$$

Where \vec{p}_{HRS} and T_{HRS} are the momentum and kinetic energy of the proton detected by HRS-R. T_{A-1} is the kinetic energy of the residual A-1 nucleus. In PWIA of the reaction $-\vec{p}_{miss} = \vec{p}_i$ the momentum of the stuck proton before it was knocked-out by the virtual photon (See figure 4-1).

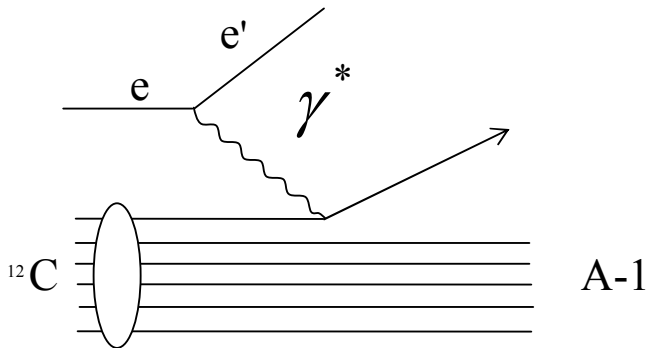


Figure 4-1: The PWIA Feynman diagram of the $^{12}\text{C}(e,e'p)$ reaction.

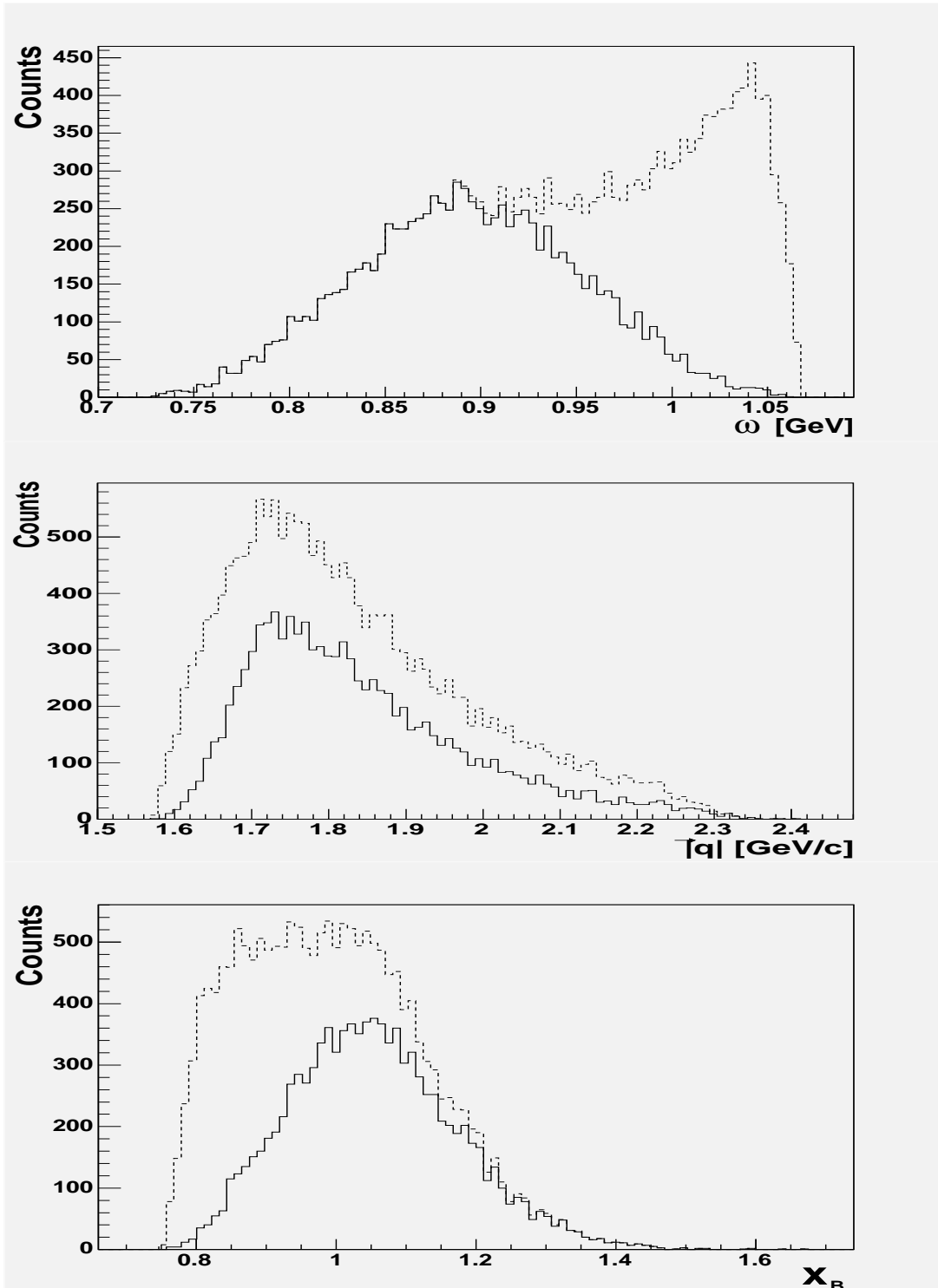


Figure 4-2: The energy transfer distribution [top]. The momentum transfer distribution [middle], and the Bjorken scaling x_B variable distribution [bottom]. The dashed line represents the entire measured distributions for K1, while the solid line shows the distributions after a cut that was applied on the angle of \vec{p}_{miss} to remove Δ -production events.

The coincident $^{12}\text{C}(e,e'p)$ events were detected in the two HRSs, with a typical trigger rate of 0.2 Hz. For HRS-L the central scattering angle (momentum) was 19.5° (3.724 GeV/c). With an incident beam of 4.627 GeV, this corresponds to a virtual photon with median three-momenta of $|\vec{q}| = 1.65$ GeV/c, energy $\omega = 0.865$ GeV, $Q^2 = 2$ (GeV/c) 2 and $x_B = 1.2$. These values correspond to the central momentum and angle of the left spectrometer and are shown in figure 1-4. Figure 4-2 shows the measured distributions of ω , $|\vec{q}|$ and x_B . As was discussed in chapter 3 we applied a cut on the direction of \vec{p}_{miss} to separate out pion and delta production ($e,e'\Delta$) events. The distributions of ω , q and x_B for the remaining ($e,e'p$) events are also shown in figure 4-2.

HRS-R was set at 3 different combinations of central angle and momentum: 40.1° & 1.45 GeV/c, 35.8° & 1.42 GeV/c and 32.0° & 1.36 GeV/c. In this work we named these kinematics settings as K1, K2 and K3 respectively. The median missing-momentum values for these kinematics are $p_{miss} = 0.3, 0.4$ and 0.5 GeV/c, respectively. The full missing momentum distributions for the $^{12}\text{C}(e,e'p)$ reaction are shown in figure 4-3.

The total beam charge collected in each of the 3 kinematics setting together with the total number of ($e,e'p$) and ($e,e'pp$) events are shown in table 4-1.

The measured $^{12}\text{C}(e,e'p)$ missing-energy spectra for K1, K2 and K3 are shown in figure 4-4. The contribution of events due to a single proton removal from the p-shell in ^{12}C , leaving the ^{11}B nucleus in its ground state, is seen as a peak at missing energy of about 16 MeV in the lowest p_{miss} kinematics (K1). The differential cross-sections calculated for this transition, compared to two theoretical calculations by Ciofi *et al.* [56] are shown in figure 4-5. The transition to the ^{11}B state is a single nucleon excitation and is discussed at [55]. The strength above the ^{11}B ground state is due to p-shell removal to highly-excited bound states and p-shell and s-shell removal to the continuum.

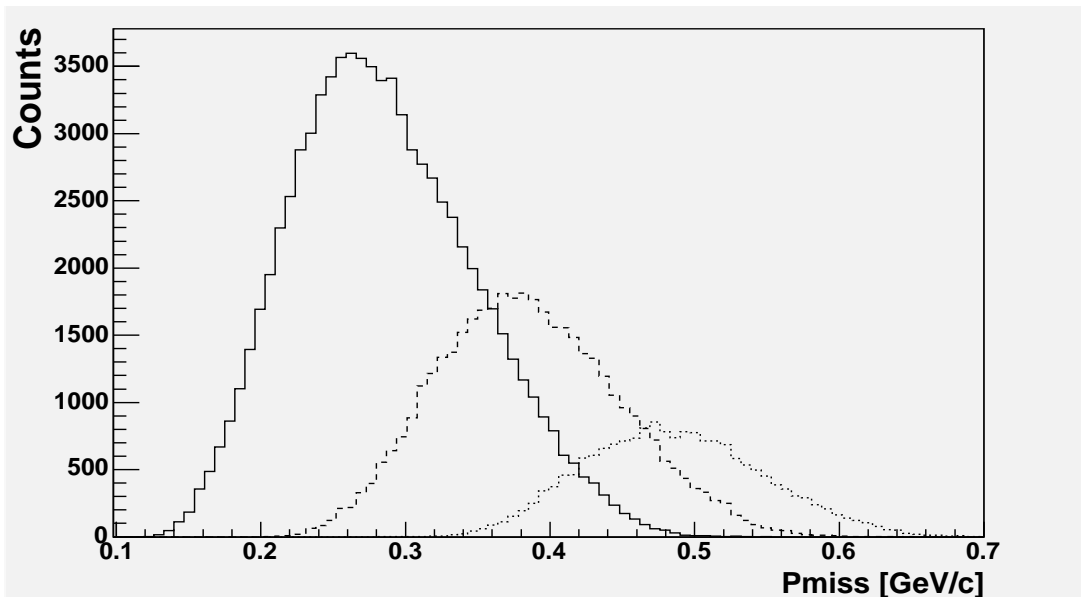


Figure 4-3: The missing momentum spectrum of the A-1 system for the K1 (solid), K2 (dash) and K3 (points) kinematics.

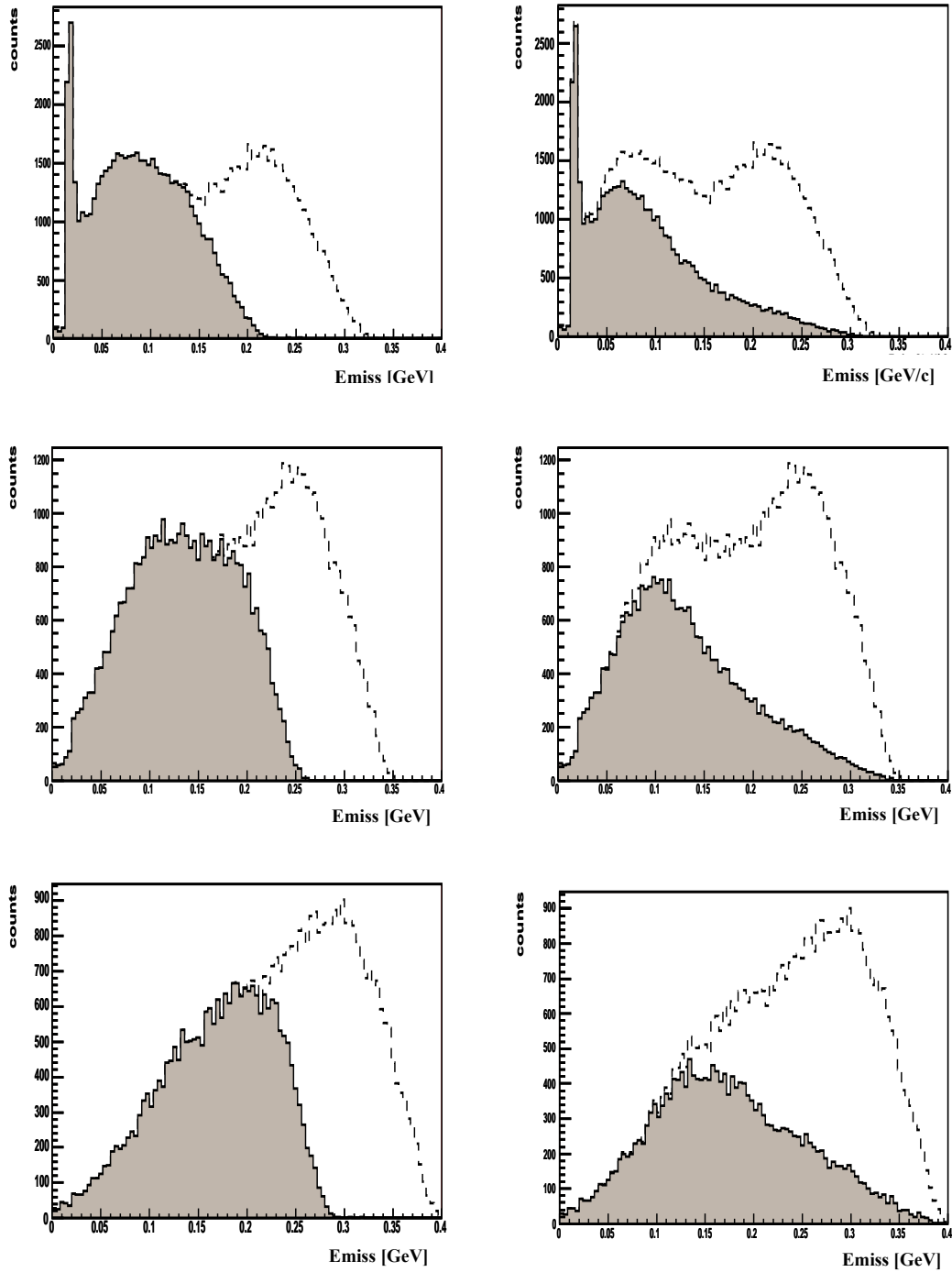


Figure 4-4: The measured $^{12}\text{C}(e,e'p)$ missing-energy spectra for kinematics K1, K2 and K3 (top to bottom). The peak at 16 MeV in K1 is due to removal of p-shell protons, leaving the ^{11}B in its ground state. The grey region contains events from s and p shell removal with residual excited bound or continuum states. The dash line contains events in which a pion was produced or a Δ was excited. These events were cut out either by using an angular cut on \vec{p}_{miss} (Left), or by applying a $x_B > 1$ (Right).

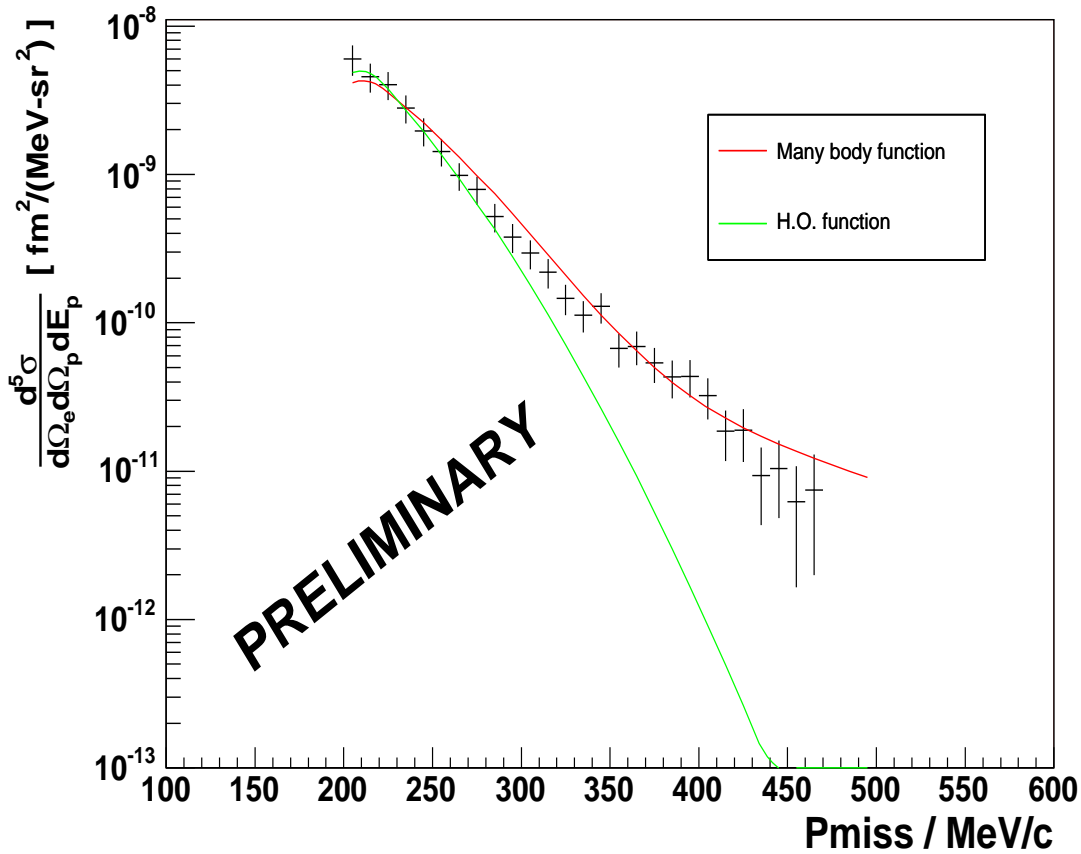


Figure 4-5: Differential Cross-Section for the $^{12}\text{C}(e,e'p)^{11}\text{B}$ transition as a function of the missing momentum. The upper curve represents many-body calculation by Ciofi [56], which takes into account short-range correlations. The lower curve is a result of harmonic oscillator model (H.O) calculation.

	Q [C]	Number of (e,e'p) events $\times 10^3$	Number of (e,e'pp) events
K1	24.2	142	178
K2	20.1	123	117
K3	14.5	87	88

Table 4-1: Summary of the total charge and the number of (e,e'p) and (e,e'pp) events for each of the 3 kinematical setups K1, K2 and K3.

4.2 The triple coincidence $^{12}\text{C}(e,e'pp)$ reaction.

The BigBite spectrometer was positioned to determine if a single high-momentum proton was balancing the \vec{p}_{miss} of the $(e,e'p)$ reaction ($\vec{p}_{rec} \approx -\vec{p}_i$).

The recoiling protons were identified in BigBite using the measured energy loss in the scintillator detectors and the consistency between the measured time-of-flight (TOF) and the momentum measured by the trajectory in the magnetic field. The momentum resolution of BigBite, determined from elastic electron-proton scattering, was $\Delta p/p = 4\%$. The singles rates with a $30 \mu\text{A}$ beam were about 100 kHz per scintillator in the first (Auxiliary) plane and 80 kHz per scintillator in the third (E) plane. With these rates, nearly all events had only one track with a reconstructed momentum consistent with the momentum from the TOF. For the events that had more than one possible reconstructed track, we selected the track that had the most consistent momentum between the TOF determination and from ray tracing. Primarily due to the gaps between scintillators, the overall proton detection efficiency was 85%. See chapter 3 for more details.

The TOF for protons detected in BigBite was defined from the target to the third (E) scintillator plane ($\sim 3 \text{ m}$) assuming the protons leave the center of the target at the same time as the scattered electrons and the knocked-out protons. This time was corrected using the reconstructed trajectory path length. The timing peaks shown in figure 4-7 are due to real triple coincidences and the flat background is due to random coincidences between the $^{12}\text{C}(e,e'p)$ reaction and protons in BigBite. The background-subtracted number of $(e,e'pp)$ events, Net , and its uncertainty ΔNet were calculated by :

$$Net = S+B-(B/n) \quad (\text{Eq. 4-5})$$

$$\Delta Net = \sqrt{S + B + (B/n^2)} \quad (\text{Eq. 4-6})$$

where $S+B$ is the total number of events in the peak window (including signal and background events), B is the number of events outside the peak window, and n is the ratio between the width of the background and the peak windows. The net number of events as a function of the size of the TOF cut is shown in figure 4-8. The selected cuts are shown in figure 4-8 as horizontal lines and in figure 4-7 as the inner vertical lines. The TOF cut to define the background are also shown in figure 4-7.

In figure 4-9 the ω , q and x_B distributions of the selected $(e,e'pp)$ events are shown compared to the distribution for the $(e,e'p)$ events. The $(e,e'pp)$ distributions shown were obtained by subtracting the B distribution (off peak) from the $S+B$ (in the peak). For comparison the $(e,e'p)$ and the $(e,e'pp)$ distributions were normalized to an equal number of events.

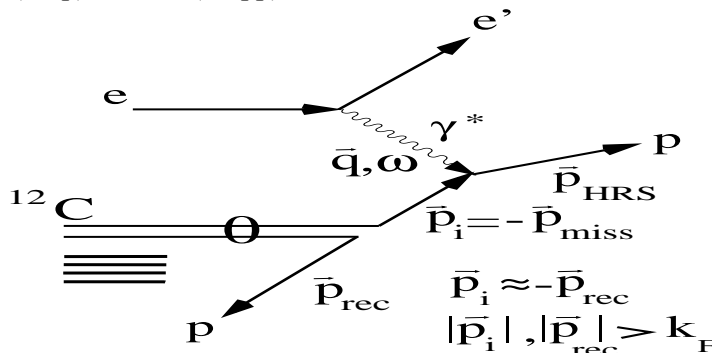


Figure 4-6: The PWIA Feynman diagram of the $^{12}\text{C}(e,e'pp)$ reaction. k_F is the Fermi sea level, which for ^{12}C is about 228 MeV/c.

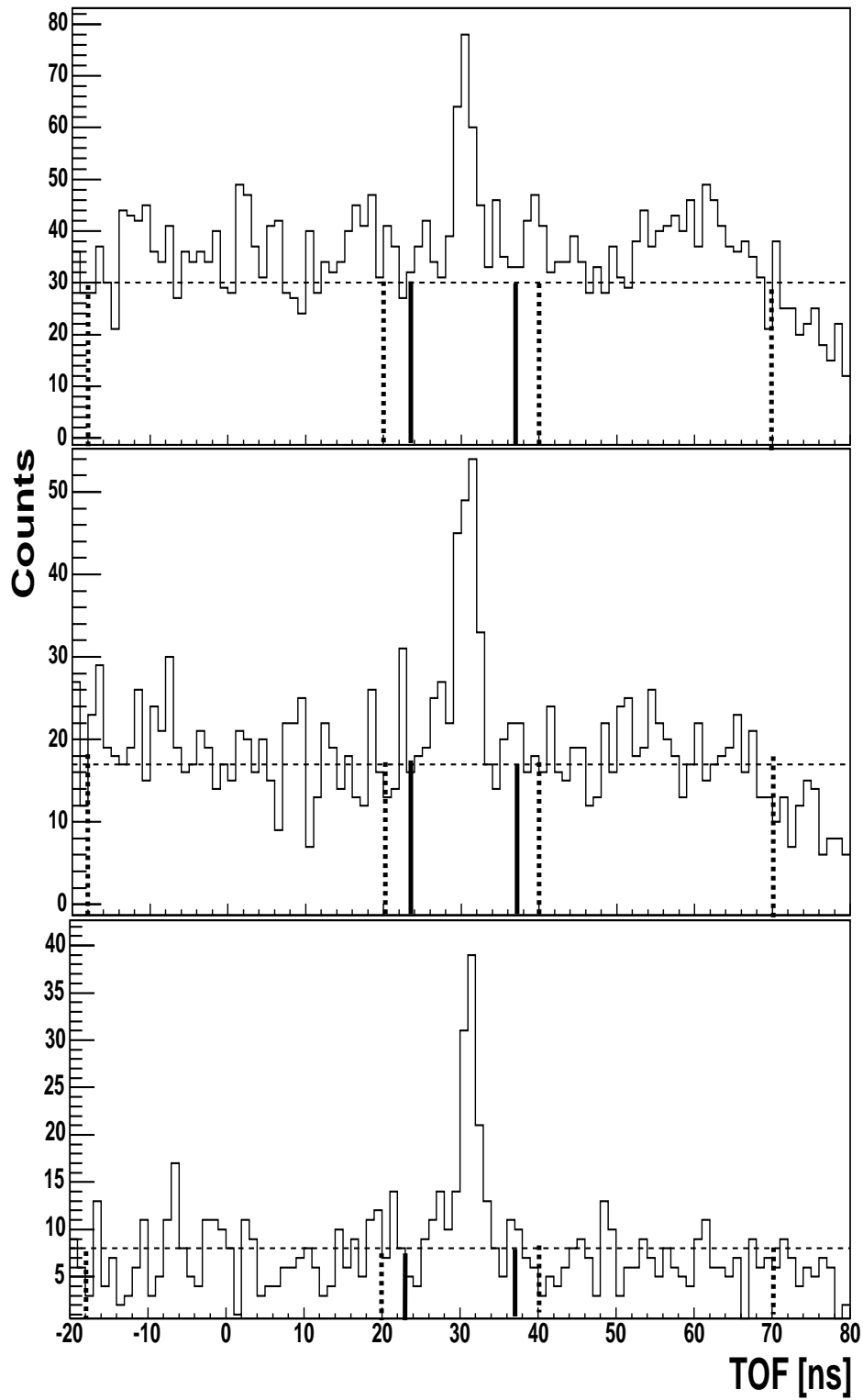


Figure 4-7: The corrected TOF between the target and BigBite E plane for K1, K2 and K3 kinematics from top to bottom respectively. The vertical lines represent the edges of the signal, while the dashed vertical lines represent the edges of the background windows.

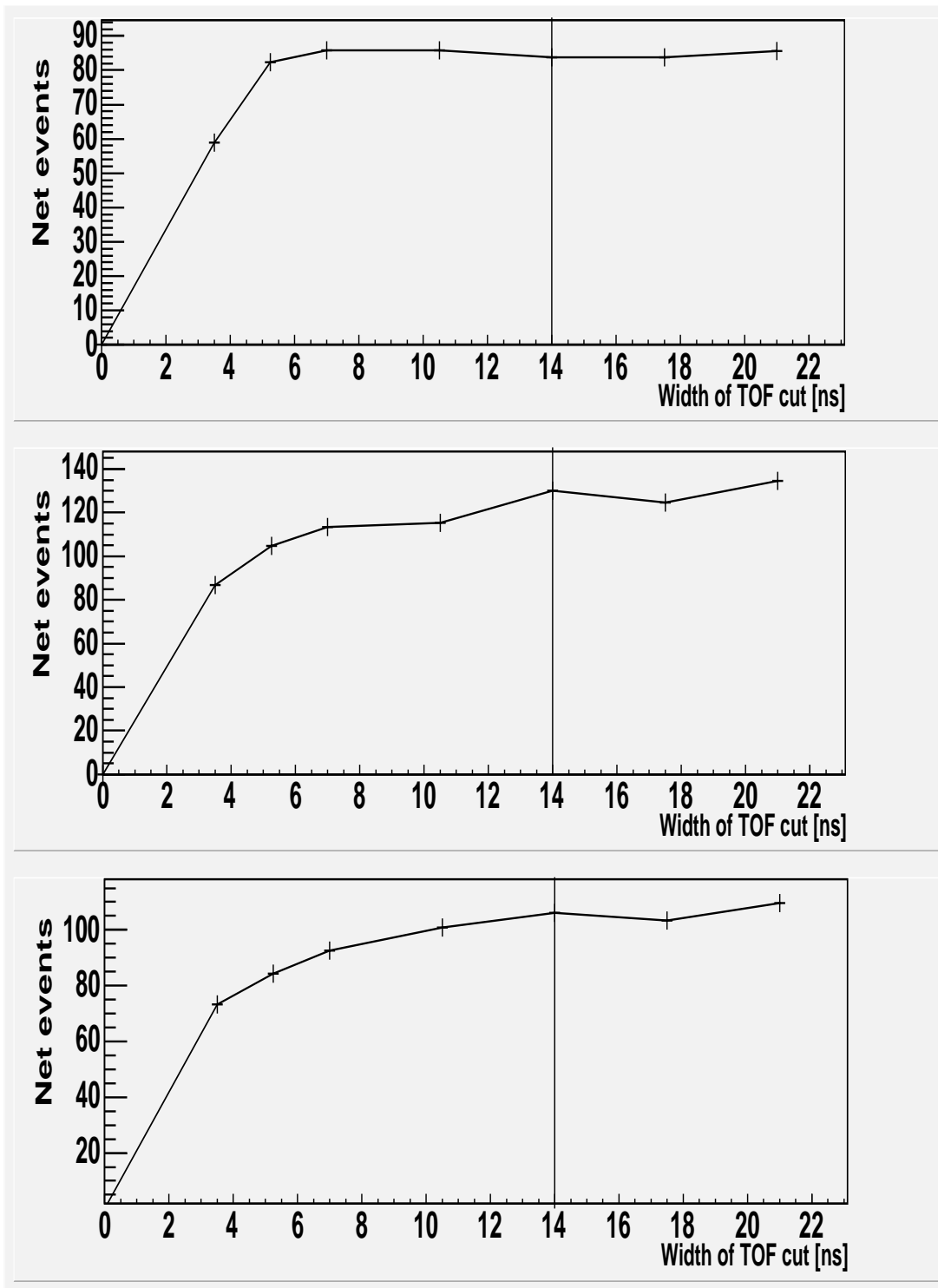


Figure 4-8: The net number of (e,e'pp) events vs. the width of the signal TOF window in TDC channels (1 ch = 35 picosec), for K1, K2 and K3 kinematics top to bottom respectively. The lines mark the width of the windows used to calculate the number of (e,e'pp). See also figure 4-7.

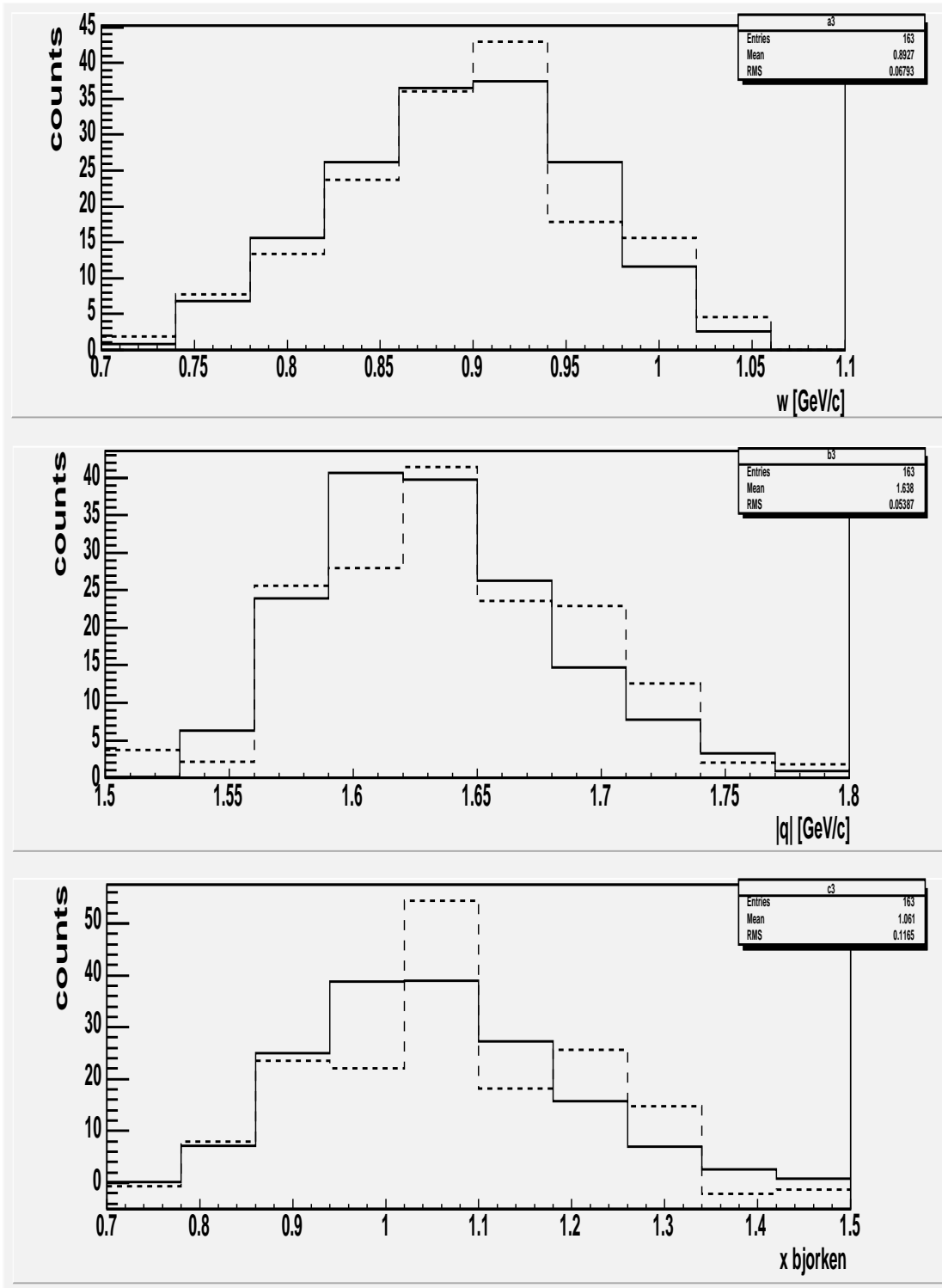


Figure 4-9: The energy transfer distribution [top]. The momentum transfer distribution [middle]. The Bjorken scaling variable x_B distribution [bottom]. The dashed line represents the measured background-subtracted $^{12}\text{C}(e,e'pp)$ distribution. The solid line is the $^{12}\text{C}(e,e'p)$ distributions normalized to the same total number of events. Both curves are after a cut to remove pion and Δ production events was applied on the angle of \vec{p}_{miss} .

4.3 The motion of the correlated pair.

Angular correlation between the two protons in the SRC pair.

The cosine of the measured angle, γ , between initial momentum of the struck proton ($\vec{p}_i = -\vec{p}_{miss}$) and the recoiling proton detected in BigBite (\vec{p}_{rec}) are shown in figure 4-10. We also show in figure 4-10 the angular correlation for the random background as defined by a time window outside the coincidence peak in figure 4-7. The back-to-back nature of the real triple-coincidence events is demonstrated clearly. The curve is a result of a simulation of the scattering off a moving pair having a center-of-mass (c.m.) momentum width of 0.136 GeV/c as discussed below. The signal to background ratio of K1 was not good enough to show the correlations signature.

Center-of-Mass motion of the pair.

For the triple-coincident events, we reconstructed the two components of $\vec{p}_{c.m.}$ in the direction towards BigBite and perpendicular to the scattering plane (the scattering plane is defined by the incoming and outgoing electron), assuming PWIA:

$$\vec{p}_{c.m.} = \vec{p}_i + \vec{p}_{rec} = -\vec{p}_{miss} + \vec{p}_{rec} . \quad (\text{Eq. 4-7})$$

In these directions, we had a large enough acceptance to be sensitive to the magnitude of the c.m. motion. The measured c.m. motion of the pair is strongly affected by the finite BigBite angular and momentum acceptances. We used the Monte Carlo simulation as described in appendix B in order to simulate the relation between the measured c.m. motion distributions and the 'real' c.m. motion.

The simulation assumes that an electron scatters off a moving pp pair with a c.m. momentum relative to the A-2 spectator system described by a 3-dimensional Gaussian distribution, with the same width in all directions (see appendix B). We varied the width of the Gaussian motion until the best agreement with the data was obtained. In principle, for small c.m. width, the measured and input ('real') widths are similar. As the input width to the simulation increases, the finite acceptances do not allow the simulated width to follow the increased input width. The effect can be seen clearly in figures 4-11 and 4-12 which show the expected width (simulation output) as a function of the assumed width (simulation input). The actual measured width of the data is represented by the middle horizontal line in each plot. The upper and lower lines represent one standard deviation from the central value. The extraction of the c.m. motion was done by calculating the corresponding simulated c.m. value of the intersection of the horizontal line with the curve. The average 'real' width of the Gaussian that represents the motion of the pair is shown in figure 4-13.

To summarize, the six measured distributions (two components in each of the three kinematics settings) yielded, within uncertainties, the same width with a weighted average of 0.136 ± 0.020 GeV/c. This width is consistent with the width determined from the (p,ppn) experiment at BNL [28], which was 0.143 ± 0.017 GeV/c. It is also in agreement with the theoretical prediction of 0.139 GeV/c in reference [56].

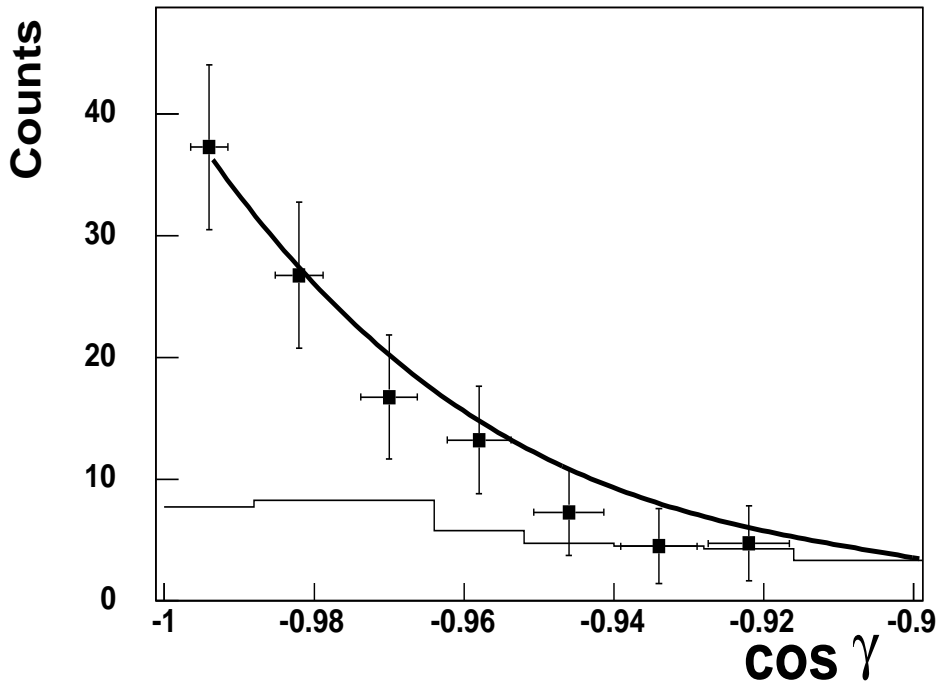
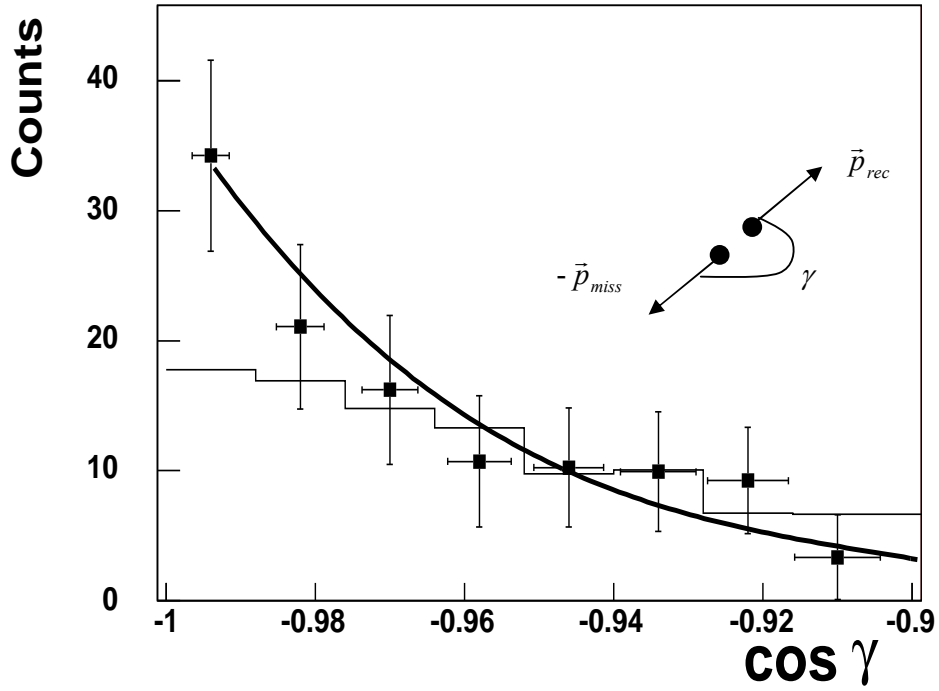


Figure 4-10: The distribution of the cosine of the opening angle γ , between $-\vec{p}_{miss}$ and \vec{p}_{rec} for the K2 (top) and K3 (bottom) kinematics. The histogram shows the distribution of random events. The curve is a simulation of the scattering off a moving pair with a width of 0.136 GeV/c for the pair c.m. momentum.

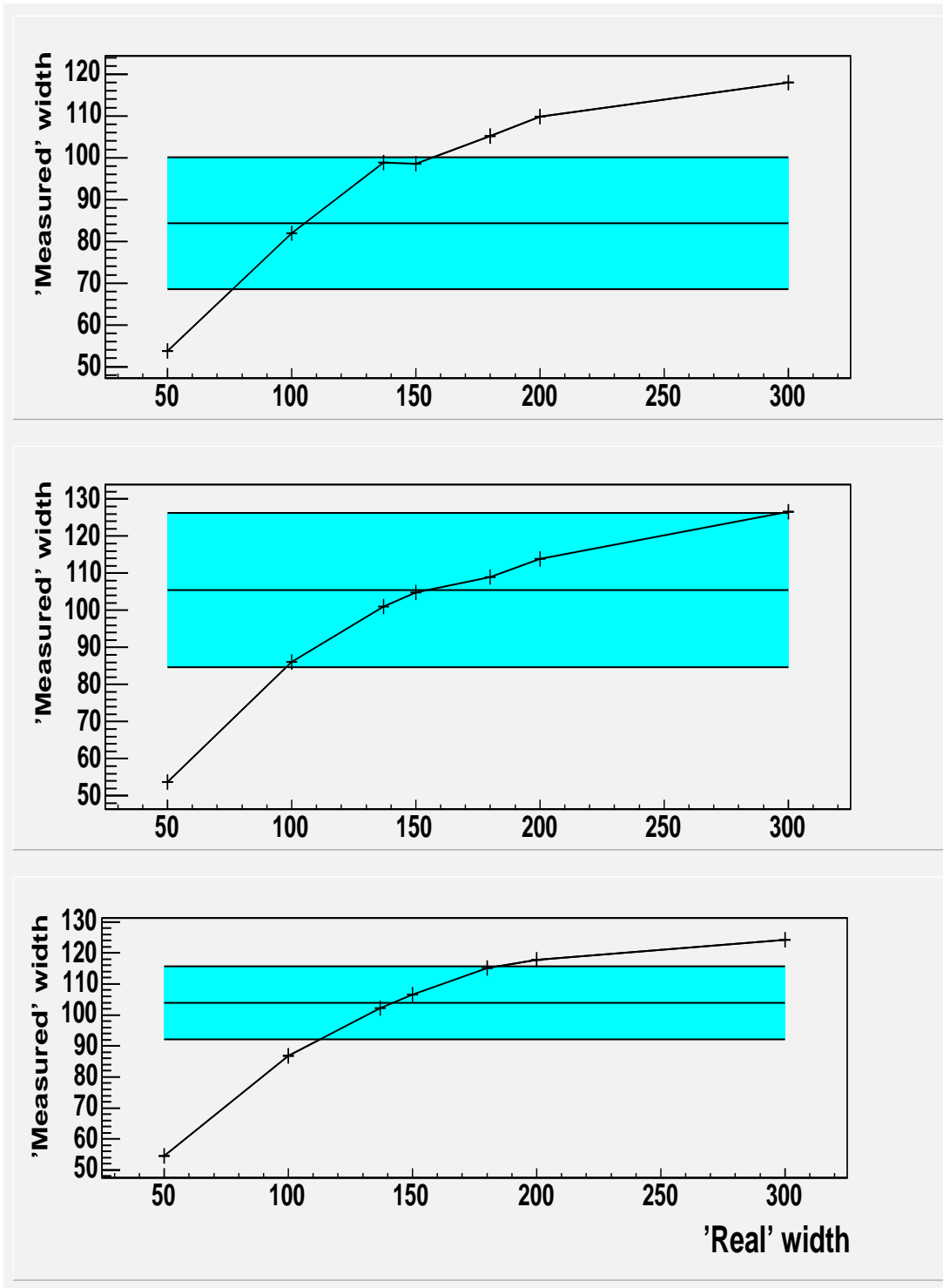


Figure 4-11: 'Measured' vs. 'real' width of the c.m. motion in the vertical direction for K1, K2 and K3 (top to bottom). The curve is a result of the simulation described in appendix B. The middle horizontal line in each plot represents the width from the data. The top and bottom lines define one standard deviation from the central value.

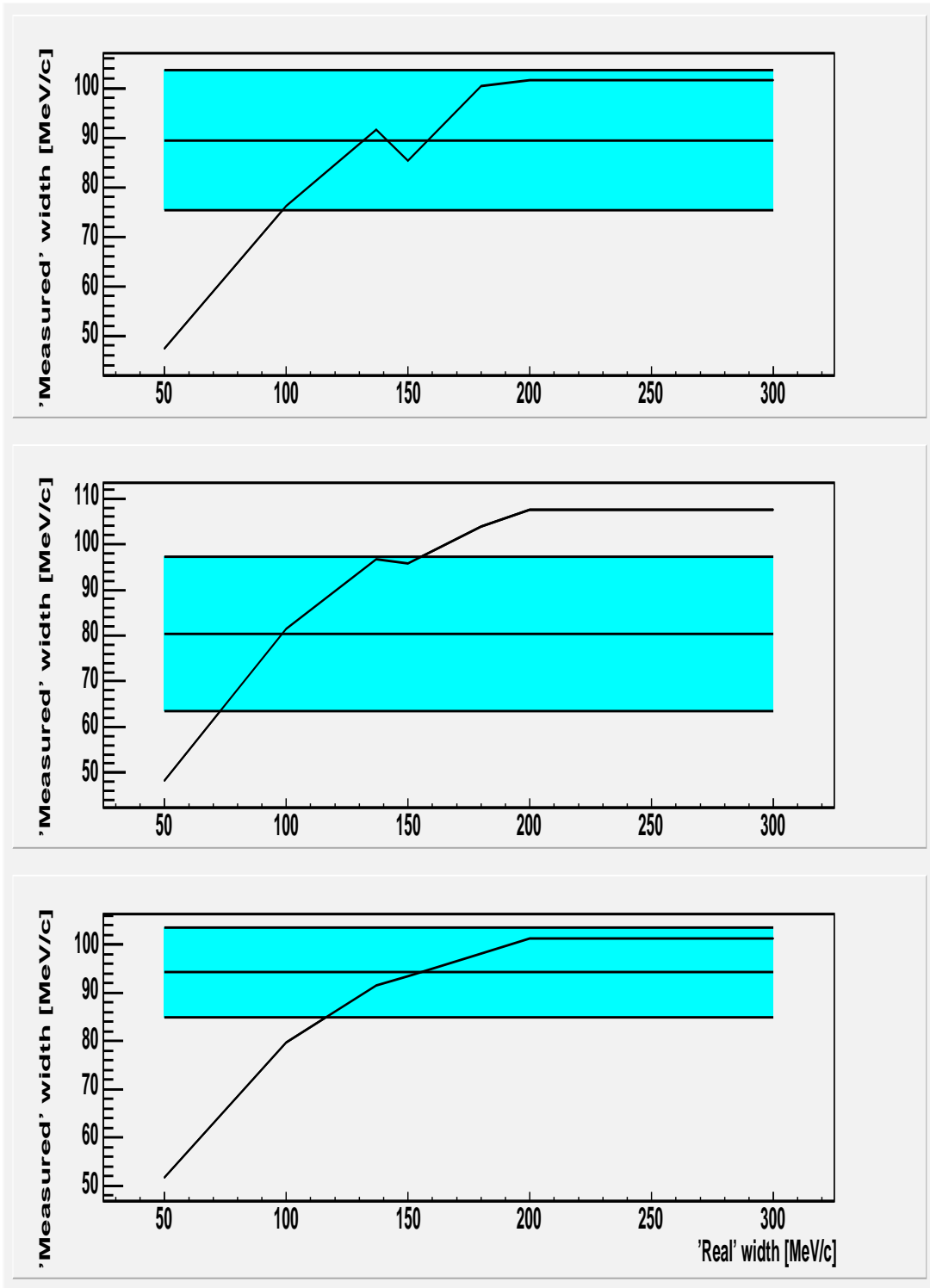


Figure 4-12: 'Measured' vs. 'real' width of the c.m. motion in the scattering plane in the direction of BigBite for K1, K2 and K3 (top to bottom). The curve is a result of the simulation described in appendix B. The middle horizontal line in each plot represents the width from the data. The top and bottom lines define one standard deviation from the central value.

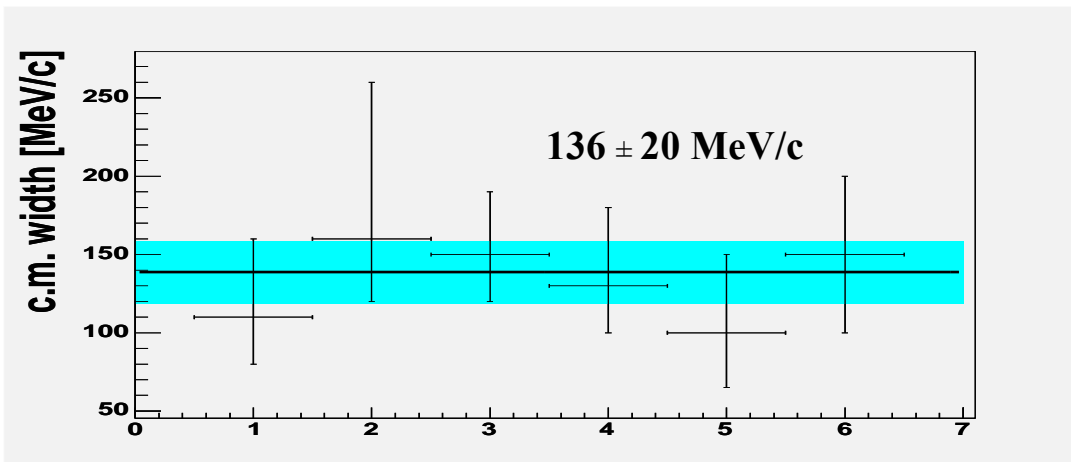


Figure 4-13: The two components of the measured c.m. width for each of the K1, K2 and K3 kinematics ($2 \times 3 = 6$ points in total).

4.4 The $(e,e'pp)/(e,e'p)$ ratio.

4.4.1 The measured ratio.

The measured ratio of $^{12}\text{C}(e,e'pp)$ to $^{12}\text{C}(e,e'p)$ events is given by the ratio of events in the background-subtracted TOF peak (see figure 4-9) to those in the shaded area in the missing energy spectrum of figure 4-5. This ratio, as a function of p_{miss} in the $^{12}\text{C}(e,e'p)$ reaction, is shown in the upper panel of figure 4-14. The uncertainties are dominated by statistics. The uncertainty in separating out events from pion and Δ production is small.

The measured ratio can be translated to the ratio of the nine-fold differential cross section for the $^{12}\text{C}(e,e'pp)$ reaction to the six-fold differential cross section for the $^{12}\text{C}(e,e'p)$ reaction. This ratio is presented in the middle panel of figure 4-14. This nine-fold differential cross section ratio was calculated by dividing the event ratio for each p_{miss} bin with the proton in BigBite energy bin ΔE_p and with BigBite angular acceptance $\Delta\Omega_p$ (which with the software cut defined in this work is equal to 90 msr).

4.4.2 The extrapolated ratio

The measured ratios are limited by the finite acceptance of BigBite. We used the simulation described in appendix B, to account for this finite acceptance. The resulting extrapolated ratios are shown in the lower panel of figure 4-14. The simulation used a Gaussian distribution (of width 0.136 GeV/c as determined above) for the c.m. momentum of the pp pairs, to study what fraction of the $(e,e'pp)$ events fall inside BigBite acceptance. The sensitivity of the extrapolated ratios to different acceptance cuts was also studied. The shaded band in the figure corresponds to using a width ± 0.040 GeV/c (two standard deviations).

As can be seen in figure 4-4, in the p_{miss} range between 0.30 and 0.60 GeV/c, $(9.5 \pm 2)\%$ of the $^{12}\text{C}(e,e'p)$ events have a second proton having $\vec{p}_{rec} \cong -\vec{p}_{miss}$ that is ejected roughly back-to-back to the first one, with very little dependence on p_{miss} .

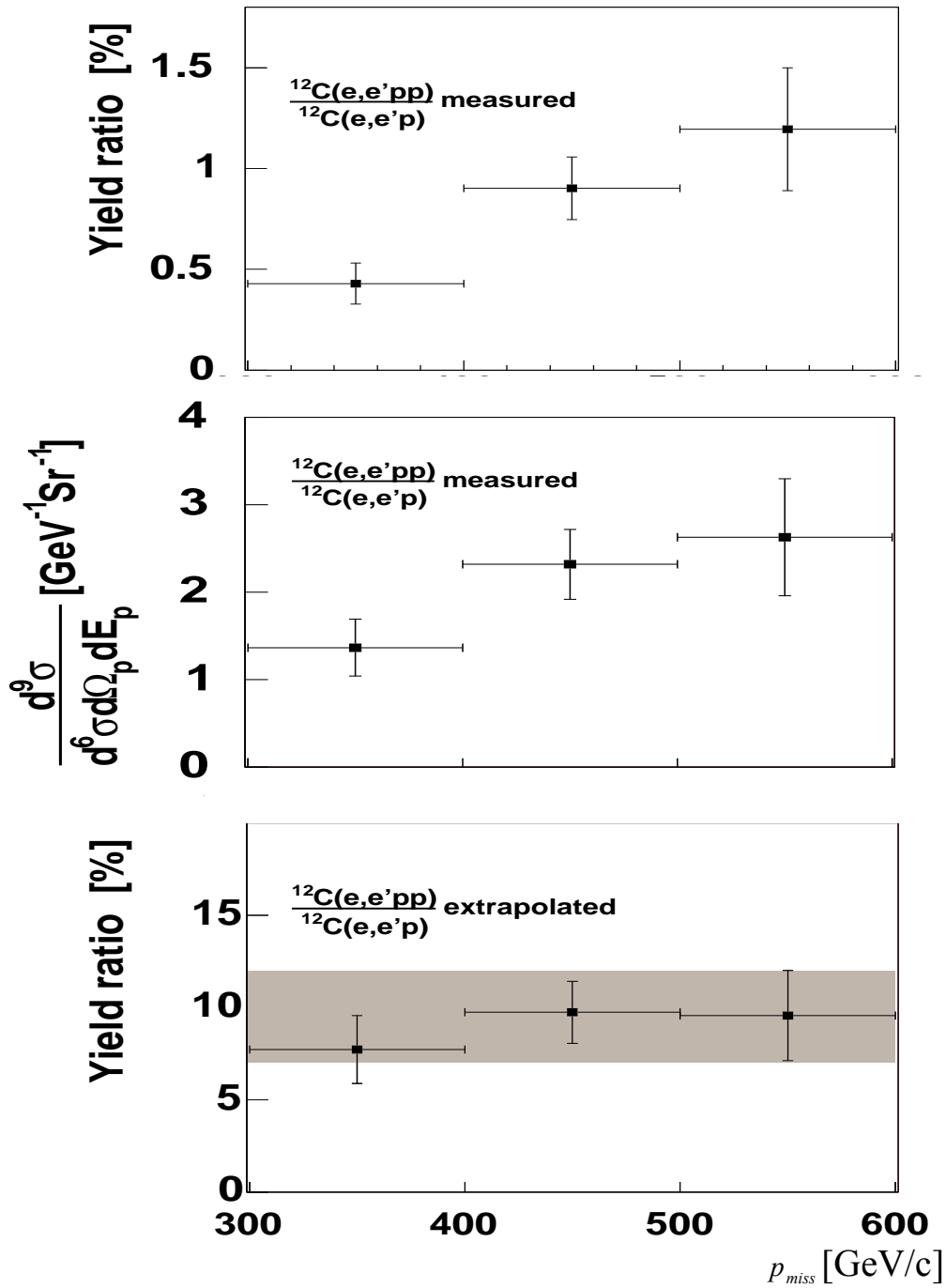


Figure 4-14: The measured and extrapolated ratios of yields for the $^{12}\text{C}(e,e'pp)$ and the $^{12}\text{C}(e,e'p)$ reactions. Top: The raw yield ratios. Middle: Differential cross section ratio of the $^{12}\text{C}(e,e'pp)$ reaction to the $^{12}\text{C}(e,e'p)$ reaction. Bottom: Extrapolated yield ratios (see text). The gray area represents a band of $\pm 2\sigma$ uncertainty in the width of the c.m. momentum of the pair.

4.4.3 Sensitivity check for the (e,e'pp)/(e,e'p) ratio.

The sensitivity of the measured and extrapolated (e,e'pp)/(e,e'p) ratio to changes in cuts was tested.

Cut for the removal of events with pion or Δ production.

To remove events with pion or Δ production, we used a cut on the angle of \vec{p}_{miss} as described in section 3.2.1. We tested the sensitivity of the triple to double coincidence ratio to changes in the selected values of the \vec{p}_{miss} angular cut. For each of the 3 kinematics, we deduced the measured (e,e'pp)/(e,e'p) ratio and calculated the extrapolated ratio for the nominal cut as well as for $\pm 4^\circ$. The nominal position and the $\pm 4^\circ$ shifted positions of these cuts for kinematics K1, K2 and K3 respectively can be seen in figure 3-13. As can be seen in table 4-2 the uncertainties introduced by changes to these cuts are smaller than the statistical errors ($\sim 20\%$). A sensitivity of the (e,e'pp)/(e,e'p) ratio to an alternative cut ($x_B > 1$), was also checked, the results are shown in Table 4-3.

Kinematics	Nominal cut	-4° below the nominal cut		$+4^\circ$ above the nominal cut	
	(e,e'pp)/(e,e'p)	(e,e'pp)/(e,e'p)	Relative change [%]	(e,e'pp)/(e,e'p)	Relative change [%]
K1	0.42 ± 0.1	0.47 ± 0.09	+11	0.38 ± 0.1	-10
K2	0.9 ± 0.15	0.87 ± 0.14	-3	0.84 ± 0.16	-6
K3	1.19 ± 0.3	1.29 ± 0.28	+8	0.96 ± 0.32	-19

Kinematics	Nominal cut	-4° below the nominal cut		$+4^\circ$ above the nominal cut	
	(e,e'pp)/(e,e'p) extrapolated	(e,e'pp)/(e,e'p) extrapolated	Relative change [%]	(e,e'pp)/(e,e'p) extrapolated	Relative change [%]
K1	7.72 ± 1.83	7.55 ± 1.55	-2	7.7 ± 2.17	0
K2	9.74 ± 1.67	8.91 ± 1.47	-8	9.85 ± 1.9	1
K3	9.56 ± 2.43	9.68 ± 2.14	+1	8.17 ± 2.7	-14

Table 4-2: The values of the measured (top) and the extrapolated (bottom) ratios with the nominal cut values, and calculated ratios when changing the angular cuts position by $+4^\circ$ and -4° . The relative changes in the ratio are also shown. The largest relative change is 19%.

Kinematics	nominal \vec{p}_{miss} cut			$x_B > 1$ cut		
	(e,e'pp)	(e,e'p)	(e,e'pp)/(e,e'p) [%]	(e,e'pp)	(e,e'p)	(e,e'pp)/(e,e'p) [%]
K1	98	27338	0.42 ± 0.1	91	22134	0.48 ± 0.11
K2	119	15746	0.90 ± 0.15	99	15751	0.74 ± 0.15
K3	46	4611	1.19 ± 0.3	69	6042	1.36 ± 0.27

Table 4-3: The values of the measured ratios with the nominal cut values, and calculated ratios when replacing the \vec{p}_{miss} angular cut with a $x_B > 1$ cut.

Sensitivity to finite acceptance corrections

Since the extrapolation factor is fairly large (~ 10) and can only be obtained by a simulation, we also performed a sensitivity check to this correction. We tested the effect of different angular acceptance cuts of BigBite on the extrapolated $(e,e'pp)/(e,e'p)$ ratio. Partial angular acceptance window cuts were applied both to the data and to the extrapolation factor calculation in the vertical and horizontal directions (see figure 4-15). Within uncertainties, no changes to the extrapolated ratio were observed except the loss of statistics.

Kinematics	Full acceptance	Cut A		Cut B	
	$(e,e'pp)/(e,e'p)$ extrapolated	$(e,e'pp)/(e,e'p)$ extrapolated	Relative change [%]	$(e,e'pp)/(e,e'p)$ extrapolated	Relative change [%]
K1	7.72 ± 1.83	7.09 ± 2.69	-8	8.77 ± 2.58	13
K2	9.74 ± 1.67	9.23 ± 2.4	-5	7.67 ± 2.28	-20
K3	9.56 ± 2.43	8.2 ± 3.35	-14	7.96 ± 3.29	-16

Table 4-4: The values of the extrapolated ratio with the nominal cut and the calculated ratio when applying the angular acceptance cuts, as shown in figure 4-14. The changes of the ratios relative to the nominal cut are also shown. The largest relative change to the extrapolated $(e,e'pp)/(e,e'p)$ ratio is 20%.

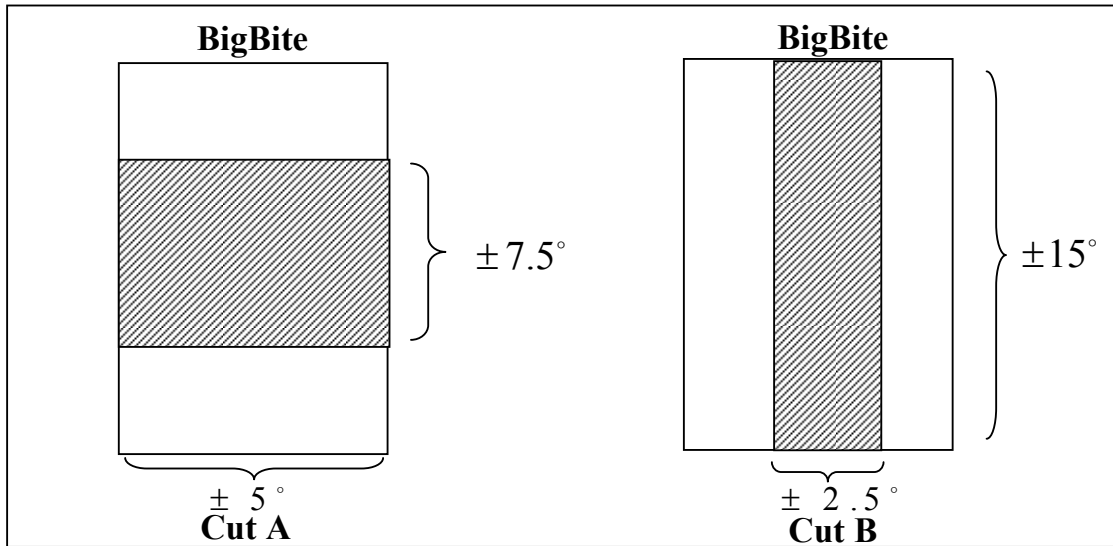


Figure 4-15: The vertical (Left-A) and horizontal (Right-B) angular acceptance cuts defined for the $(e,e'p)/(e,e'pp)$ ratio sensitivity check.

4.5 The missing energy spectra of the $^{12}\text{C}(e,e'pp)$ reaction.

For the triple coincidence events, one can define the missing energy as follow:

$$E_{2m} = E - E' - T_{HRS} - T_{rec} - T_{A-2} \quad (\text{Eq. 4-8})$$

The reaction includes removal of protons from the $(1p)^2$, $(1p1s)$ and $(1s)^2$ states. The average separation energies for these transitions can be calculated from the separation energies of 1p and 1s protons in ^{12}C taking in to account the interaction energies between the proton in the pair [57,58]. The separation energies for $(1p)^2$, $(1p1s)$ and $(1s)^2$ are then:

$$\begin{aligned} E_{2m}(1p)^2 &= E_{miss}(1p) + E_{miss}(1p) - E_{pair}(1p)^2 = 16 + 16 - 4.5 = 27.5 \text{ [MeV]} \\ E_{2m}(1p1s) &= E_{miss}(1p) + E_{miss}(1s) - E_{pair}(1p1s) = 16 + 38 - 2 = 52 \text{ [MeV]} \\ E_{2m}(1s)^2 &= E_{miss}(1s) + E_{miss}(1s) - E_{pair}(1s)^2 = 38 + 38 - 8.5 = 67.5 \text{ [MeV]} \end{aligned} \quad (\text{Eq. 4-9})$$

Note that the $(1p1s)$ and $(1s)^2$ are wide distributions and the values above are the central values of the distribution.

The measured distribution of the missing energy spectra of the $^{12}\text{C}(e,e'pp)$ reaction can be seen in figure 4-16. A clear peak resulting from the $(1p)^2$ excitations at 27 MeV can be seen. This is with agreement with theoretical calculations [57,58], which showed that the $(1p1s)$ and $(1s)^2$ excitations, are wide, and inseparable by measurement, which is the case for our measured spectra. The event excess between 40 and 80 MeV, might be explained by the combination of these two excitations. At $E_{2m}=34$ MeV two additional channel open; the $^{12}\text{C}(e,e'ppn)^9\text{Be}$ channel and the $^{12}\text{C}(e,e'ppnn)^4\text{He}^4\text{He}$ channel. Since little strength is observed in the region $E_{2m}=30-45$ MeV, the contributions of these reactions to the measured cross-section are small. Another noticeable feature is the excess of events at around 95 MeV. The origin of this strength above 85 may be due to knock-out of more than two particles.

For comparison, in figure 4-17, we also present two other previous measurements of the missing energy following a removal of two protons from ^{12}C [17,59]. The first was a $^{12}\text{C}(e,e'pp)$ low $Q^2 \approx 30 \text{ (MeV/c)}^2$ measurement with an energy transfer $\omega \approx 212$ MeV and missing momentum p_{miss} range of 300-600 MeV/c. This measurement was done at NIKHEF and is described in details in the thesis by Leon Kester [35] and a following publication [17]. The second measurement is a $^{12}\text{C}(e,e'd)$ measurement performed at MIT-Bates with energy transfer $\omega \approx 200$, $x_B=2$, $Q^2 = 770 \text{ (MeV/c)}^2$ and $|\vec{q}| \approx 900$ MeV/c, which is described in a thesis by Steven Douglas Penn [59]. Both measurements were done as a part of a study of SRC, and show similar features to those described above.

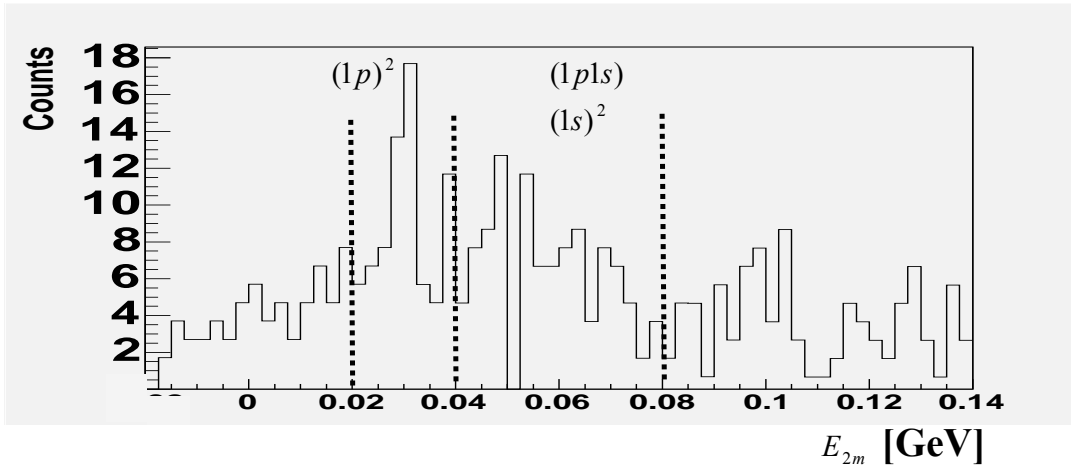


Figure 4-16: The number of events as a function of the two nucleon missing energy E_{2m} for kinematics K2 and K3 combined.

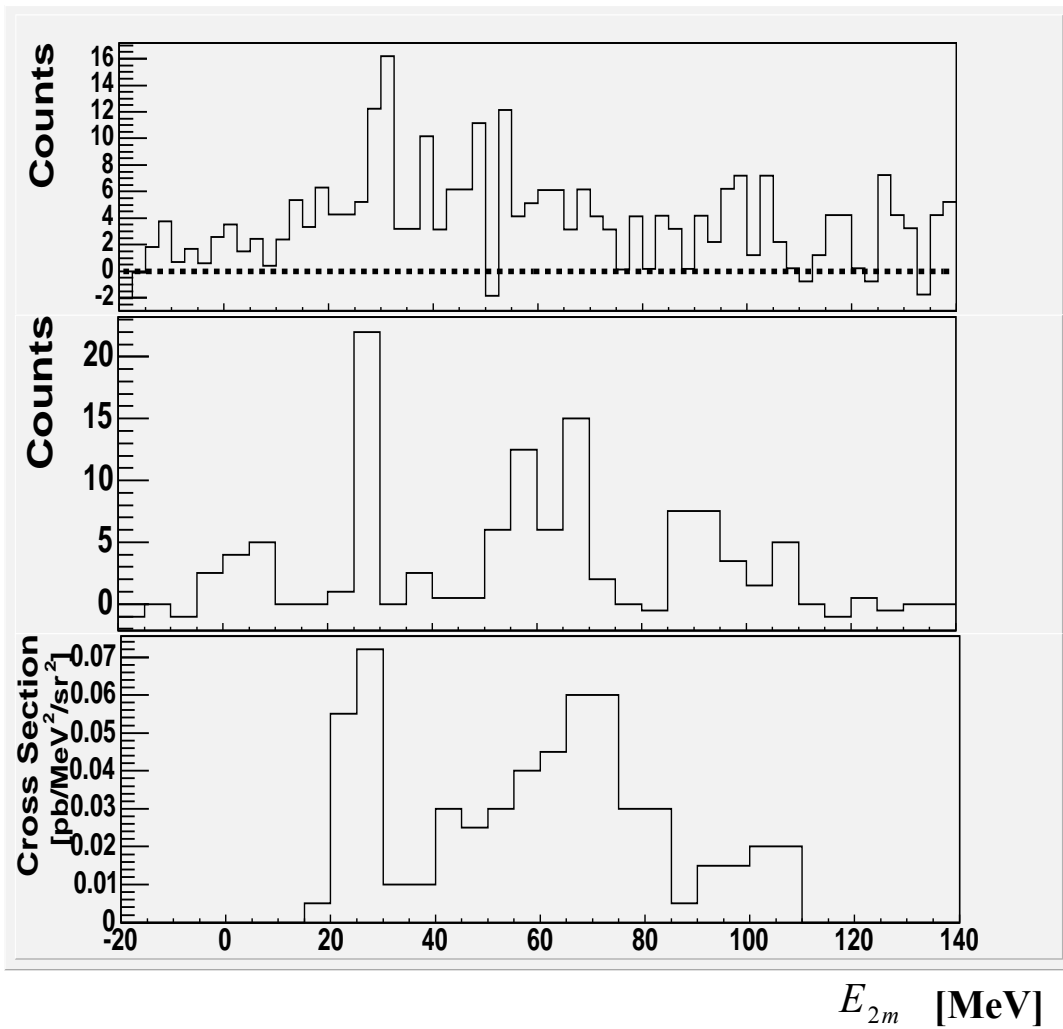


Figure 4-17: The number of events as a function of the two nucleon missing energy E_{2m} . Top : This experiment kinematics K2 and K3 combined. Middle: measurement by Kester et al.[17]. Bottom: measurement by Penn et al.[59].

4.6 Summary and Conclusions.

The new high-energy, high-luminosity accelerator facilities of the last decade make it possible to reveal the existence of SRC pairs and to study their features using high-momentum transfer reactions.

We measured simultaneously the $^{12}\text{C}(e,e'p)$ and $^{12}\text{C}(e,e'pN)$ reactions in kinematics designed to maximize observation of SRCs while suppressing other effects such as FSI, IC, and MEC. We identified directionally and momentum correlated proton pairs in ^{12}C using the $^{12}\text{C}(e,e'pp)$ reaction. In the PWIA, the c.m. momentum distribution of the pp-SRC pair was determined to have a Gaussian shape with a width of 0.136 ± 0.020 GeV/c.

We determined the fraction of the $^{12}\text{C}(e,e'p)$ events at $p_{\text{miss}} \approx 300\text{-}600$ MeV/c from pp-SRCs to be 9.5 ± 2 %. This ratio indicates a small abundance of pp-SRC in ^{12}C compare to the number of np-SRC pairs as determined from the BNL/EVA measurement [28]. These results have been recently published [69].

The $^{12}\text{C}(e,e'pn)$ reaction channel was also measured as a part of this experiment. The simultaneous measurement of $^{12}\text{C}(e,e'pp)$ and $^{12}\text{C}(e,e'pn)$ allow for the first time, a direct estimation of the ratio of np-SRC/pp-SRC pairs in ^{12}C . The results of this measurement are described elsewhere [5]. Preliminary results confirm the dominance of np-SRC over pp-SRC in ^{12}C , which is a clear fingerprint of the nucleon-nucleon short-range force [8].

The primary source of high-momentum nucleons in nuclei is short-range correlated pairs, i.e. pairs of nucleons with large, roughly equal back-to-back momenta. The isospin structure of these pairs is important as it can teach us about the strong interaction at short distances. In particular, the ratio of n-p short-range correlation (np-SRC) pairs to p-p short-range correlation (pp-SRC) pairs is highly sensitive to the short-range part of the N-N tensor force. Moreover, as a manifestation of asymmetric dense cold nuclear matter that can be studied in the laboratory, pp-SRCs are relevant to the understanding of neutron stars.

The small percentage of pp-SRC pairs obtained from this experiment can be interpreted as a clear fingerprint of the short-range N-N tensor force [8]. These correlations become important in nuclei when high densities are reached locally. This situation occurs in neutron stars on a large scale. The observations reported in this work could be important for understanding crucial questions on the formation of neutron stars from supernovae, such as the limit on the mass of the star, and the physics of neutrino cooling. A small concentration of protons inside a neutron star can have a disproportionately large effect due to the differences in the short-range n-p and p-p interactions.

APENDIX A: Path reconstruction for charged particles in BigBite.

BigBite was designed to measure the momentum and angle of charged particles. Timing, hit position and energy deposited in the scintillators are all being used to measure the direction and momentum of the incoming particles. A non-focusing magnetic dipole ($B \sim 0.9$ T) is used to curve the charged particle paths before they hit the detector planes. The radius of curvature of the particle path in the magnetic field is proportional to its momentum.

To calculate the three-dimensional position of a detected particle, we used the known positions of the scintillator bars that were hit and the time differences between the generated signals in the left and right PMTs of those bars. The hit pattern information of each scintillator plane was used to reconstruct the particle path inside the magnetic field and the corresponding magnitude and direction of the particle's momentum.

The magnetic field in the BigBite spectrometer is perpendicular to the detector planes. We define this direction to be the y direction. The full chosen coordinate system is shown in Figure A-1: The magnetic field can be treated as fixed effective magnetic field inside known boundaries, vanishing outside these boundaries. This enables us to separate the calculation into two components; a charged particle moving freely in the y -direction and under the influence of the magnetic field in the x - z plane, according to:

$$\frac{d\mathbf{p}}{dt} = e\mathbf{v} \times \mathbf{B}. \quad (\text{Eq. A-1})$$

Assumptions & parameters

The central trajectory has the following quantities:

- $p=500$ MeV/c, curvature radius $r=1.81$ m, magnetic field $B=0.92$ T
- The angle between entry and exit radii is 25° .
- One can adjust the effective field boundaries.
- A point target and point hits on the auxiliary and trigger planes.
- The geometrical constants of the problem are those obtained from a full survey of the spectrometer.

Calculation of the particle movement on the x - z plane

The calculation of the particle movement is done using the fact that outside the magnetic field boundaries we can treat the particle as a free particle, and, as such, it moves in straight lines. Those lines are tangent to the circular motion done by the particle inside the boundaries of the magnetic field.

The equation describing the particle straight line movement, after exiting from the magnetic field area, is found from the known hit points of the particle on the trigger and auxiliary planes, and is given by

$$z = a_3x + b_3, \quad (\text{Eq. A-2})$$

Where a_3 and b_3 are calculated in a straight forward manner. The point where this line intercept with the boundary of the magnetic field is the exit point, marked as point E in figure A-1.

We marked as point I, the entry to the magnetic field boundary. This point is known as a function of a single parameter l . The parameter l indicates the distance of point I from the beam line. We write the particle straight path from the target point to point I as

$$z = \frac{l}{d_1}x + l, \quad (\text{Eq. A-3})$$

where d_1 is the distance of the target point from the entrance boundary of the magnetic field area. The path of the charged particle in the magnetic field is a circle which the lines given by Eq. A-2 and Eq.A-3 are tangent to it. Therefore, the center of the circle is found by taking perpendiculars to the lines given by Eq. A-1 that passes through points I and E and finding the point where those perpendiculars intercept. The equation that describes the line perpendicular to the line in Eq. A-2 is

$$z = -\frac{1}{a_3}(x - E_x) + E_z \quad (\text{Eq. A-4})$$

The equation that describes the line perpendicular to the line in Eq. A-3 is

$$z = -\frac{d_1}{l}x + l \quad (\text{Eq. A-5})$$

Using the fact that both the distance of point I from the center of the circle and the distance of point E from the center of the circle are equal (circle radii), we write an equality that defines the parameter l . By doing so we get

$$l^3 + A_2l^2 + A_1l + A_0 = 0, \quad (\text{Eq. A-6})$$

$$A_2 = a_3d_1 + 2a_3E_x - 2E_z, \quad (\text{Eq. A-7})$$

$$A_1 = E_z^2 - E_x^2 - 2d_1E_x - 2a_3d_1E_z - 2a_3E_xE_z, \quad (\text{Eq. A-8})$$

$$A_0 = 2d_1E_xE_z + a_3d_1E_z^2 - a_3d_1E_x^2. \quad (\text{Eq. A-9})$$

A more compact way of writing Eq. A-6 is

$$l'^3 + pl' + q = 0, \quad (\text{Eq. A-10})$$

where,

$$l' = l + \frac{1}{3}A_2, \quad (\text{Eq. A-11})$$

$$p = A_1 - \frac{1}{3}A_2^2, \quad (\text{Eq. A-12})$$

$$q = \frac{2}{27}A_2^3 - \frac{1}{3}A_2A_1 + A_0. \quad (\text{Eq. A-13})$$

In this form Eq. A-6 has the following three solutions:

$$l'_1 = u - v, \quad (\text{Eq. A-14})$$

$$l'_2 = -\frac{1}{2}l'_1 + i\frac{\sqrt{3}}{2}(u + v), \quad (\text{Eq. A-15})$$

$$l'_3 = -\frac{1}{2}l'_1 - i\frac{\sqrt{3}}{2}(u + v), \quad (\text{Eq. A-16})$$

where

$$u = \left(-\frac{1}{2}q + \sqrt{\frac{q^2}{4} + \frac{p^3}{27}} \right)^{\frac{1}{3}}, \quad (\text{Eq. A-17})$$

$$v = \frac{p}{3u}. \quad (\text{Eq. A-18})$$

Eq. A-14, A-15 and A-16 describes three distinct solutions for l , from that we choose only the physical solution. The physical solution has to have the following characteristic:

- i.* The parameter l must be real.
- ii.* The entry point calculated as a function of the parameter l must be on the magnetic field boundaries.
- iii.* The particle must move on the path from the target point to the hit point on the Trigger plane in a physical manner. It means that the circular motion in the magnetic field has to be on the short arc of the circle, and must be counter clockwise or clockwise when the center of the circle is higher or lower, respectively, than the perpendicular lines to the left and right sides of the magnetic field boundaries passing through points I and E, respectively.

In order to find the direction of movement of the particle in *iii.*, we define two vectors: \mathbf{R}_1 which is a vector that connects the center of the circle to point I, and \mathbf{R}_2 which is a vector that connects the center of the circle to point E. those are two vectors in the \mathbf{x} - \mathbf{z} plane that their vector product

$$\mathbf{R}_1 \times \mathbf{R}_2 = R^2 \sin \beta \mathbf{y} \quad (\text{Eq. A-19})$$

gives a positive value in the \mathbf{y} direction if the movement is from the trigger plane to the target (counter clockwise), and negative value if the movement is from the target to the trigger plane (clockwise).

After applying the three roles, we have a physical solution for l , from which we can calculate the path L_{xz} , and the momentum $|\mathbf{P}_{xz}|$ of the particle on the \mathbf{x} - \mathbf{z} plane.

The momentum is given by:

$$|\mathbf{P}_{xz}| = eBR, \quad (\text{Eq. A-20})$$

The path length (given a hit point H on the Trigger plane):

$$L_{xz} = \sqrt{l^2 + d_1^2} + R\beta + \sqrt{(H_x - E_x)^2 + (H_z - E_z)^2}, \quad (\text{Eq. A-21})$$

where the angle β is found from the scalar product

$$\mathbf{R}_1 \cdot \mathbf{R}_2 = R^2 \cos \beta \quad (\text{Eq. A-22})$$

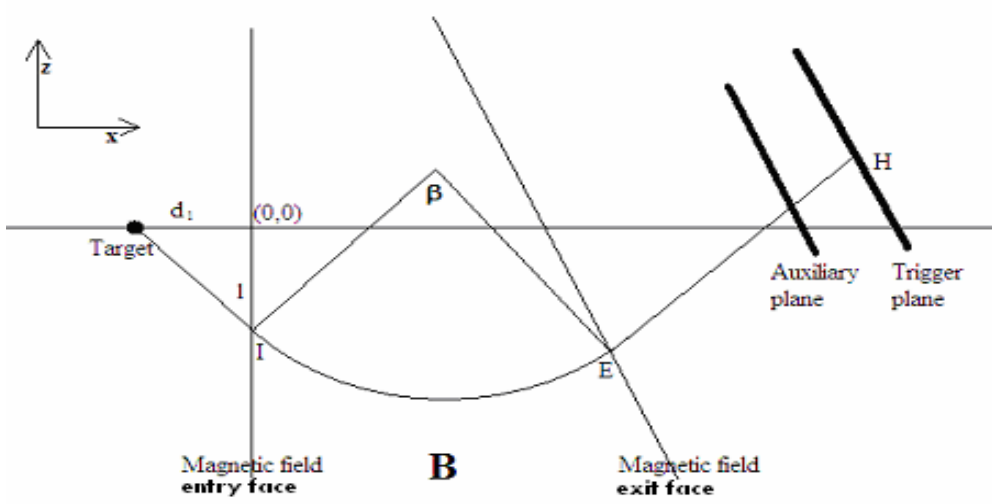


Figure A-1: A schematic view of a particle path (in the x-z plane) leaving the Target, changing its direction while moving in the magnetic field area, and finishing its path at the trigger plane.

Calculation of the particle movement in three dimensions

In the three dimensional problem we have only two known points, the target point T and the hit point H on the Trigger plane. From those points we find the total momentum of the particle by using the relation

$$\frac{P_y}{|\mathbf{p}_{xz}|} = \frac{v_y}{|v_{xz}|} = \frac{H_y - T_y}{L_{xz}}. \quad (\text{Eq. A-23})$$

Using eq A-23, the total momentum is:

$$|\mathbf{p}| = \sqrt{p_y^2 + |\mathbf{p}_{xz}|^2} = eBR \sqrt{1 + \left(\frac{H_y - T_y}{L_{xz}} \right)^2}, \quad (\text{Eq. A-24})$$

and the total length of the particle path is

$$L = \sqrt{L_{xz}^2 + (H_y - T_y)^2}. \quad (\text{Eq. A-25})$$

APENDIX B: Monte-Carlo simulations.

Various aspects of the experiment were tested and calculated using Monte-Carlo simulations. The different applications of these simulations include rate calculations, finite acceptance corrections, resolutions and efficiency evaluations.

3 Monte-Carlo simulations were used:

- MCEEP simulation for describing the $(e,e'p)$ and also $(e,e'pp)$ part of the reaction.
- A simulation to calculate the $(e,e'pp)$ part of the reaction using the real $(e,e'p)$ events.
- GEANT4 BigBite detector simulation.

The MCEEP simulation

MCEEP - Monte Carlo for $(e,e'p)$ experiments, is the Standard Hall A Monte Carlo simulation tool [60]. It includes a simulation of the Hall A experimental set-up (i.e. the HRS pair) and various event generators for different physical models.

A new physics model was incorporated in order to simulate the short-range correlation experiment [61]. The dedicated new event generator assumes a "quasi-deuteron" model, which involve the scattering of electrons from a deuteron which has an initial Fermi motion in the lab frame. To simulate also the recoil part of the reaction, the simulation assumes that for each high momentum proton there is a short-range correlated partner, which is emitted back-to-back in the c.m. frame of the pair.

This simulation was used primly to simulate coincidence and singles rates, but also to calculate the finite acceptance extrapolation factors for the $(e,e'pp)/(e,e'p)$ ratio (see section 4.4.3) and to determine the c.m. motion of the observed p-p pairs (see section 4.2).

For more details see [61].

Monte-Carlo simulation based on the $(e,e'p)$ data.

This simulation code was used as a cross-check to the modified MCEEP simulation described above. The advantage of this simulation over the MCEEP simulation, is that it uses real $(e,e'p)$ events to simulate the recoil protons in BigBite, rather than simulated $(e,e'p)$ events. The simulation assumed SRC pairs with 3 dimensional Gaussian c.m. motion distributions with equal widths in all 3 axes. The width is a free parameter, to be entered by the user. For each $(e,e'p)$ event, a specific SRC pair motion is simulated, and the direction and momentum of a recoil partner are then calculated. The main aspects which were tested using this code are similar to the MCEEP simulation and include calculation of the finite acceptance extrapolation factors for the $(e,e'pp)/(e,e'p)$ ratio (see section 4.4.3) and determining the c.m. motion of the observed p-p pairs (see section 4.2).

GEANT4 BigBite detector simulation.

The GEANT4 detector simulation kit [62] was used to simulate the BigBite spectrometer magnet with the trigger and auxiliary scintillator planes used for this experiment [63]. Various reconstruction techniques and detector characteristics were studied using this simulation [64]. Among the aspects which were studied were momentum and angular resolutions, efficiencies and acceptance features.

More details on the BigBite GEANT 4 simulation can be found at [64].

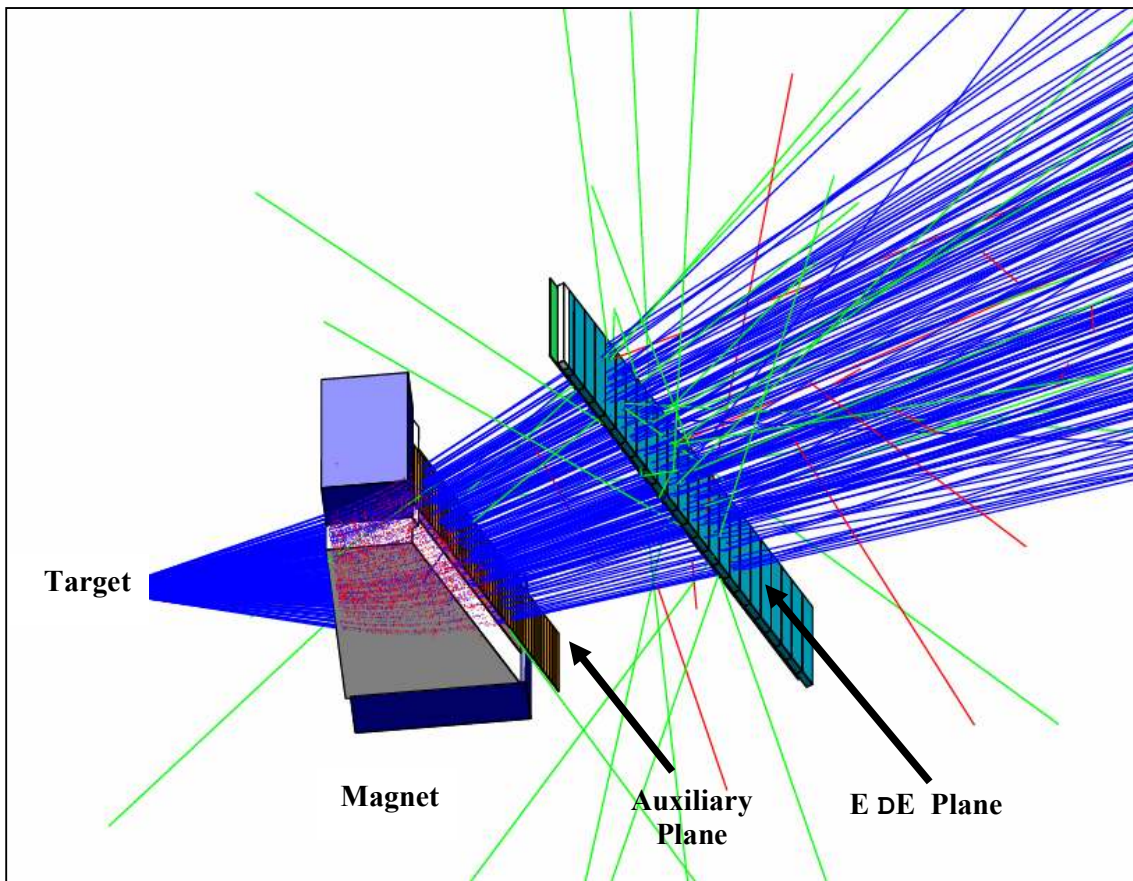


Figure B-1: A GEANT4 schematic view of BigBite with simulated 400 MeV/c proton tracks (dark) and neutrons tracks (bright).

APENDIX C: Estimate of final-state interactions.

We follow the method of I. Mardor *et al.* [44] to estimate the FSI effects on the measurement.

Step 1:

We calculate in a Glauber approximation σ_{eff} for 1.5 GeV/c protons (the momentum of our high energy proton) and for proton with 600 MeV/c, which is the lowest energy proton with a known measured transparency obtained by using (e,e'p).

The calculation is given by:

$$T = \frac{1}{A} \int \rho \exp(-\sigma_{eff} \int \rho \hat{z} dl) dv \quad (\text{Eq. C-1})$$

Where ρ is the nuclear density, which is normalized by the integral over the nuclear volume :

$$\int \rho dv = A \quad (\text{Eq. C-2})$$

We adjusted the effective cross section to obtain the measured transparency.

The results we obtained are:

$$\sigma_{eff}(1.5 \text{ GeV} / c) = 26 \text{ mb}$$

$$\sigma_{eff}(600 \text{ MeV} / c) = 14 \text{ mb}$$

Table C-1 and C-2 show how the calculated results with the assigned effective cross sections fit the available data

nucleus	T calculated	T measured
¹² C	0.6	0.635
Fe	-	0.45
Au	-	0.33

Table C-1: data for 1.5 GeV/c protons from O'Neill *et al.* [65]. The Data is an average of the measurement at $Q^2=1$ and 3 GeV/c²

nucleus	T calculated	T measured
¹² C	0.76	0.77
²⁷ Al	-	0.65
⁵⁸ Ni	-	0.54
¹⁸¹ Ta	-	0.41

Table C-2: data for 600 MeV/c protons from Garino *et al.*[66].

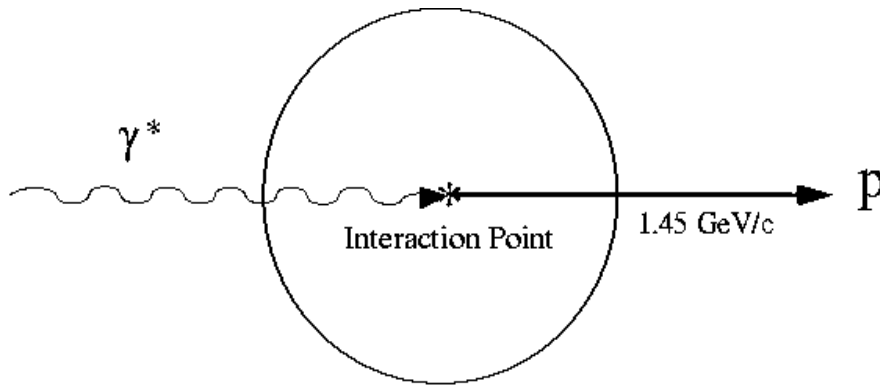


Figure C-1: The schematics of the calculations for the transparency of the knocked proton in this experiment.

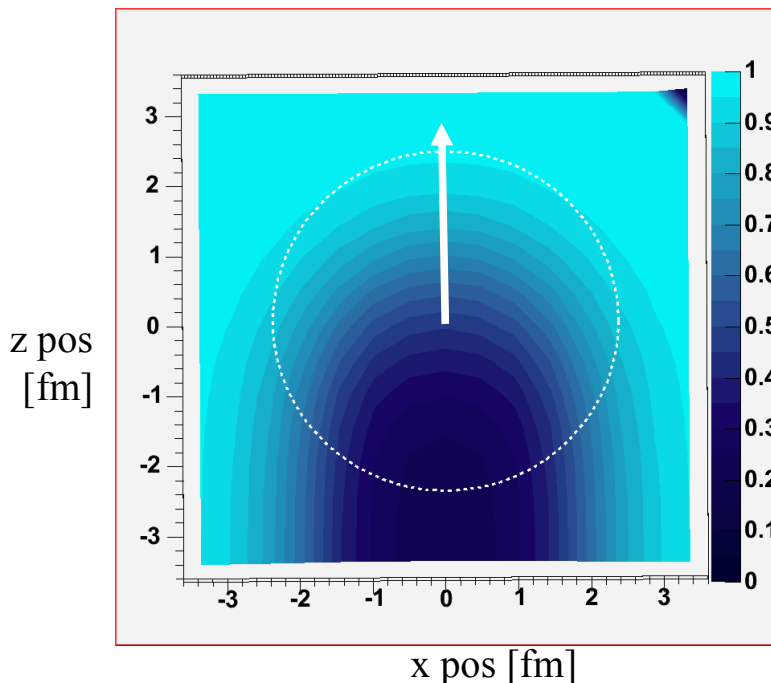


Figure C-2: The calculated transparency as a function of the interaction point in the nucleus. The dashed line represents the RMS radius of ^{12}C at 2.4 Fermi's.

Step 2:

We estimate the effective cross section for the recoil proton in this experiment i.e. protons with momentum 250-650 MeV/c. To do this we used the measured effective cross section at 600 MeV/c and the energy dependent of the mean free path as calculated by Pandharipande and Pieper [67]. The effective cross section obtained is shown in figure C-3 as a function of the proton momentum. The transparency calculated for protons in this momentum range are shown for ^{12}C in figure C-5 as a function of the proton momentum.

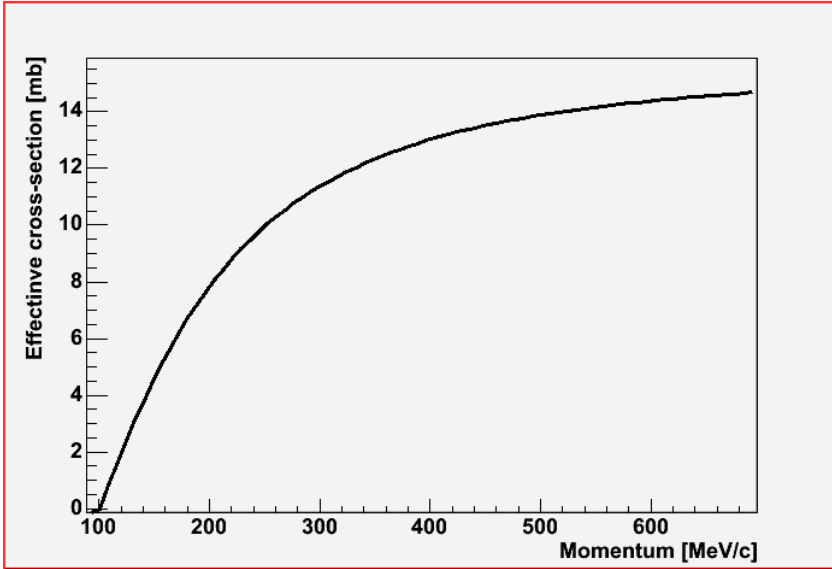


Figure C-3: The effective cross section for low energy protons.

Step 3:

The transparency of the recoil particle in the triple coincidence experiment is higher than that calculated in step 2 since the $(e,e'p)$ already selected an interaction point in the nucleus where the transparency of the $(e,e'p)$ proton is high and therefore the transparency of the recoil proton is also high. We calculated the conditioned transparency as:

$$T = \frac{1}{A} \int \rho \exp(-\sigma_{eff}(1.5 \text{ GeV}/c) \int \rho \hat{z} dl) \exp(-\sigma_{eff}(p_{recoil}) \int \rho \hat{n} dl) dv \quad (\text{Eq. C-3})$$

See figure C-4 for a schematic description of the calculation. The unit vector \hat{n} in the equation above is about 50° to the z axis.

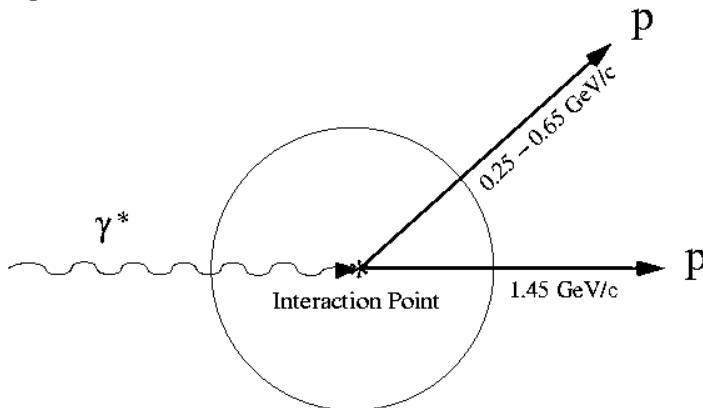


Figure C-4: The schematic of the conditioned transparency calculation for the two protons in the triple coincidence experiment.

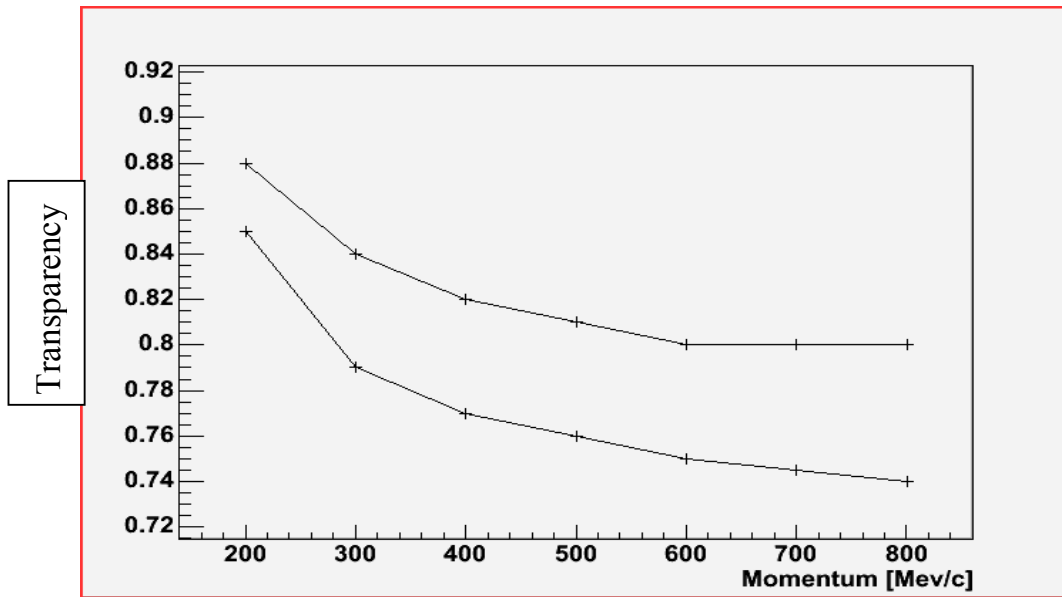


Figure C-5: The Transparency and conditioned Transparency (upper plot) as a function of the momentum of the recoil particle.

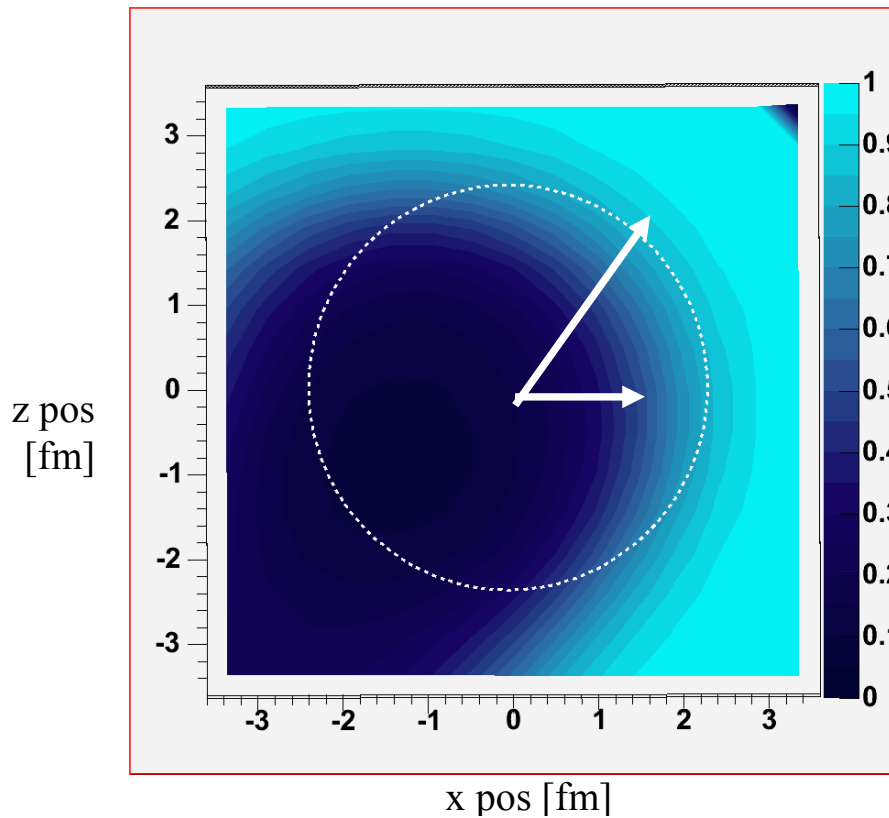


Figure C-6: The combined transparency for the two protons as a function of the interaction point in the nucleus. Notice that here the high momentum proton emerges along the horizontal axis not the vertical axis as in figure C-2.

Single Charge Exchange (SCX)

Some of the (e,e'pp) events might be due to (e,e'n) on np pairs followed by SCX of the high momentum neutron. Since the SCX is very forward peaked at these energies, we assumed that each proton produced in a SCX process will look like a correlated partner. To estimate this effect, we will assume that the effective cross section for this is given by:

$$\sigma_{eff}^{SCX} = \sigma_{eff}(1.5GeV/c) \frac{\sigma_{SCX}}{\sigma_{TOTAL}} \quad (\text{Eq. C-4})$$

Where the ratio of the integrated SCX to the total cross section was taken from ref [68]. The probability of this to happen for 1.5GeV/c neutrons in ¹²C was calculated to be:

$$P = 1 - T = 1.6\% \quad (\text{Eq. C-5})$$

The FSI effect on the measured (e,e'pp)/(e,e'p) ratio

Assuming the (e,e'pn) is an order of magnitude larger than the (e,e'pp), the contamination of (e,e'pp) events with contribution from the np correlated pairs is about 16%. For the low energy partner the probability to do SCX is lower due to Pauli blocking [67] and also due to the fact that there is no strong forward peak as in the high energy case. We therefore neglected the contamination due to SCX of the recoil neutron. The transparency of the recoil proton is about 15-20 % (see figure C-5). Therefore, our rough estimation of the FSI effect indicates that the absorption and single-charge-exchange compensate each other so that the net effect is small compared to the uncertainties in the measurement. This conclusion is backed by the c.m. motion result which gives widths for all the components that are narrow and internally consistent (see section 4-3).

Bibliography

- [1] G. Mayer, Phys. Rev. **74**, 235 (1948).
- [2] L. Lapikas, Nucl. Phys. P **A553** 297c (1993).
- [3] K. S. Egiyan *et al.*, Phys. Rev. C **68**, 014313 (2003).
- [4] K. S. Egiyan *et al.*, Phys. Rev. Lett. **96** 082501 (2006).
- [5] R. Subedi Ph.D thesis, unpublished (2007).
http://hallaweb.jlab.org/experiment/E01-015/e01015ramesh_thesis/details/Thesis_Final.pdf
- [6] J. Arrington *et al.*, Phys. Rev. Lett. **82**, 2056 (1999).
- [7] L. L. Frankfurt, M. I. Strikman, D. B. Day and M. M. Sargsyan, Phys. Rev. C **48**, 2451 (1993).
- [8] O. Benhar *et al.*, Phys.Rev.C **47**, 2218 (1993).
- [9] J. S. O'Connell *et al.*, Phys. Rev. Lett. **53**,1627 (1984); Phys. Rev. C **35**, 1053 (1987).
- [10] W.Bertozzi, R.W. Lourie and E.J. Moniz, in Modern Topics in Electron Scattering, B. Frois and I. Sickfieds editors (World Scientific, 1991).
- [11] P.E. Ulmer *et al.*, Phys. Rev. Lett. **59**, 2259 (1987).
- [12] D. Day *et al.*, Phys. Rev. Lett. **43**, 1143 (1979).
- [13] D. Rohe *et al.*, Phys. Rev. Lett. **93**, 182501 (2004).
- [14] J. Ryckebusch, S. Janssen, W. Van Nespén, and D. Debruyne, Phys. Rev. C **61**(2000).
- [15] O. Benhar, A. Fabrocini, S. Fantoni, I. Sick, Nucl. Phys. **A579**, 493 (1994).
- [16] C.J.G.Onderwater *et al.*, Phys. Rev. Lett. **78**, 4893 (1997).
- [17] L.J.H.M.Kester *et al.*, Phys. Rev. Lett. **74**, 1712-1715 (1995).
- [18] C.J.G. Onderwater *et al.*, Phys. Rev. Lett. **81**, 2213 (1998).
- [19] A. Zondervan *et al.*, Nucl., Phys. **A587**, 697 (1995).
- [20] D.L. Groep *et al.*, Phys. Rev. Lett. **83**, 5443 (1999).
- [21] D.L. Groep *et al.*, Phys. Rev. C **63**, (2001).
- [22] K.I. Blomqvist *et al.*, Phys. Lett. B **424**, 71 (1998).

- [23] G. Rosner, Prog. Part. Nucl. Phys. **44**, 99 (2000).
- [24] J. Arends *et al.*, Z. Physik **A298**, 103(1980).
- [25] M. Kanazawa *et al.*, Phys. Rev. C **35**, 1828 (1987).
- [26] J. Ryckebusch, S. Janssen, W. Van Nespén and D. Debruyne, Phys. Rev. C **61**, (2000).
- [27] Stijn Janssen, Jan Ryckebusch, Wim Van Nespén and Dimitri Debruyne, Nucl. Phys. A **672**, 285-309, (2000).
- [28] J. Aclander *et al.*, Phys. Lett. B **453**,211 (1999).
- [29] A. Malki *et al.*, Phys. Rev. **C65**, 015207 (2002).
- [30] A. Tang *et al.*, Phys. Rev. Lett. **90** (2003).
- [31] E. Piassetzky, M. Sargsian, L. Frankfurt, M. Strikman, and J. W. Watson, Phys. Rev. Lett. **97**, 162504 (2006).
- [32] L. L. Frankfurt and M. I. Strikman, Phys. Rept. **76** (1981).
- [33] C. Ciofi degli Atti *et al.*, Phys. Rev. C **44**, R7 (1991).
- [34] E. J. Moniz *et al.*, Phys. Rev. Lett. **26**, 445 (1971).
- [35] L. Kester Ph.D Thesis, unpublished (1993).
- [36] K. I. Blomqvist *et al.*, Phys. Lett. **B421**, 71 (1998).
- [37] D. L. Groep *et al.*, Phys. Rev. **C63**, 014005 (2001).
- [38] J. M. Laget, Phys. Lett. B **199**, 493 (1987).
- [39] R. J. Glauber, in Lectures in Theoretical Physics, edited by W. Brittain and L. G. Dunham, Wiley Interscience, New York, V.1 (1959).
- [40] E.J. Moniz and G.D. Nixon, Annals of Physics **67** 58 (1971).
- [41] D.R. Yennie in Hadronic Interactions of electrons and Photons ed. J. Cummings, D. Osborn, 321 (1971).
- [42] L. L. Frankfurt, M. M. Sargsyan, M. I. Strikman, Phys. Rev. C **56**, 1124 (1997).
- [43] V. R. Pandharipande and S. C. Pieper, Phys. Rev. C **45**, 791 (1992).
- [44] I. Mardor, Y. Mardor, E. Piassetzky, J. Alster, and M. M.Sargsian, Phys. Rev. **C46**, 761 (1992).
- [45] J. Alcorn *et al.*, Hall A - Nucl. Instrum. Meth. **A 522**, 294 (2004).

- [46] J.D. Walecka, Electron Scattering for Nuclear and Nucleon Structure, Cambridge Monograph on Particle Physics, Nuclear Physics and Cosmology, v. 16 (Cambridge University Press, 2001).
- [47] R. Shneor M.Sc thesis, "High luminosity operation of large solid angle scintillator arrays in Jefferson Lab Hall A" unpublished (2003).
- [48] Progress Report on the Auxiliary Plane, for the Triple Coincidence Experiment with BigBite, (2001).
- [49] The Jefferson lab data acquisition group, CODA - CEBAF On-Line Data Acquisition User's Manual, unpublished (1999).
- [50] <http://www-esd.fnal.gov/esd/catalog/intro/introfb.htm>.
- [51] <http://www-esd.fnal.gov/esd/catalog/intro/introvme.htm>.
- [52] <http://www.windriver.com/products/wxworks5/>
- [53] <http://hallaweb.JLab.org/root/>
- [54] R. Brun (CERN), ROOT An object-Oriented Data Analysis Framework User Guide, unpublished (2003).
- [55] P. Monaghan Ph.D. Thesis (to be submitted).
- [56] C. Ciofi degli and S. Simula, Phys. Rev. **C53**, 1689 (1996).
- [57] C. Giusti and F.D. Pacati, Nucl. Phys. **A535** 573 (1991).
- [58] C. Giusti and F.D. Pacati, Nucl. Phys. **A546** 607 (1992).
- [59] S.D. Penn Ph.D thesis, "An Examination of two-nucleon correlations in $^{12}\text{C}(e,e'p)$ and $(e,e'd)$ " unpublished (1985).
- [60] MCEEP Monte Carlo for $(e,e'p)$ experiments-
<http://hallaweb.JLab.org/software/mceep/mceep.html>
- [61] Scattering off a moving pair in nuclei-
<http://hallaweb.JLab.org/experiment/E01-015/documents/e01015-mc.ps>
- [62] GEANT4 -toolkit for the simulation of the passage of particles through matter-
<http://cern.ch/geant4/>
- [63] GEANT4/C++ Monte Carlo studies of the BigBite Focal-Plane detector system-
http://hallaweb.JLab.org/experiment/E01-015/documents/BB_MC.ps
- [64] Simulated momentum and scattering angle reconstruction with BigBite-
<http://hallaweb.JLab.org/experiment/E01-015/documents/position.ps>

- [65] O'Neill *et al.*, Phys. Lett. **87** 351 (1995).
- [66] Garino *et al.*, Phys. Rev. **C45** 780 (1992).
- [67] Pandharipande and Pieper Phys. Rev. **C45** 791 (1992).
- [68] Friedes *et al.*, Phys. Rev. Lett. **15** 38 (1965).
- [69] R. Shneor *et al.*, Phys. Rev. Lett. **99** (2007).